MASTER THESIS

Dayinta Perrier

Light Trapping in Thin Film a-Si:H Solar Cells with Reflective and Plasmonic Nanostructured Back Contacts

Nanorod synthesis combined with FDTD simulations and optimizations for nanostructured solar cells

---

Supervisors:
Lourens van Dijk MSc
Yinghuan Kuang MSc
Dr. Marcel Di Vece

External supervisor
Prof. Dr. Ruud E. I. Schropp

Universiteit Utrecht

UTRECHT UNIVERSITY
FACULTY OF SCIENCE
DEBYE INSTITUTE FOR NANOMATERIALS SCIENCE
SECTION NANOPHOTONICS - PHYSICS OF DEVICES
14.02.2013

ABSTRACT

Solar energy is a promising renewable energy resource. Solar cells can convert solar energy into electrical energy. In order to make solar cells widely economically competitive, it is required to decrease the production cost. Thin film solar cells are developed to reduce the cost by the use of less and low cost material. One of the opportunities to increase the absorption of thin film solar cells, is a nanostructured back reflector. A recent development is to place plasmonic nanostructures at the rear side. By plasmonic light trapping, the absorption can be enhanced.

In this thesis, two structures of a-Si:H solar cells with (plasmonic) nanostructured back reflectors are investigated: a nanorod and a nanohole back reflector. The benefit of a nanorod structured solar cell is the orthogonalization of the light travel path and the carrier transport path. In addition, the nanorod system demonstrates an anti-reflection effect at the top surface and a strong light scattering inside the cell. In this thesis first a wet chemical method for the synthesis of ZnO nanorods on polyethylene naphtalane is described, serving as a base for the metal nanorod back reflector. The growth parameters including reactant concentration, growth time and seed layer thickness on the morphology of ZnO nanorods are investigated and optimized. Secondly, Finite-Difference Time Domain (FDTD) simulations are performed on the nanorod solar cell to study the absorption in the active a-Si:H i-layer. From the simulations, the origin of the absorption is investigated and an optimal nanorod solar cell design is proposed.

The second studied solar cell has a back contact with nanoholes. This is an interesting plasmonic nanostructure, since it can as well propagate surface plasmons and as scattering resonance plasmons can be generated. The absorption of this nanostructured is studied by the use of FDTD simulations. The results give an insight on the origin of the enhanced absorption, by which it can be determined which absorption enhancements are caused by a plasmonic effect.

Contents

1 Introduction

1.1 Energy generation

Oil, coal and peat together cover more than half the energy supply in the world, as shown in figure 1. Two big problems arise from our reliance on these energy sources: global warming (the greenhouse effect) and sustainability. The first problem is that the emission of CO_2 from burning of coal and oil significantly contributes to the global greenhouse effect [20]. In 1997 the Kyoto Protocol was adopted and put into operation in 2005. A protocol in which more than 37 countries, including the European Union, over the world made the commitment to limit the emission of greenhouse gases [73]. In order to cut back on the Greenhouse effect, it is necessary to transfer to more environmentally friendly and renewable energy sources [19].

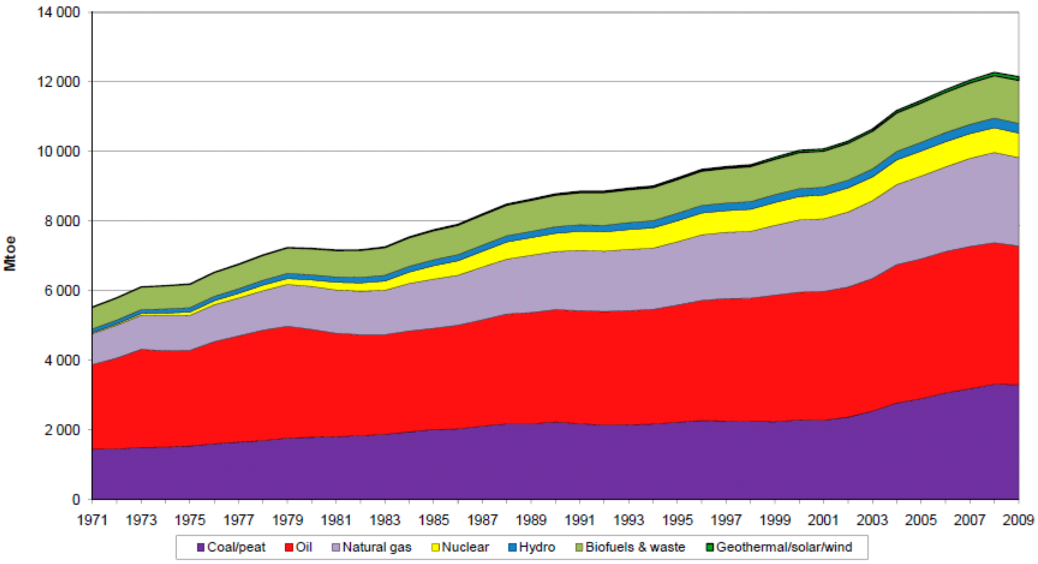

Fig. 1: Total primary energy supply of IEA Energy Statistics [18].

The second problem of our dependency on oil, coal and peat is their sustainability [34]. The energy demand increases and will in all probability increase significantly in the coming years as the prognosis shows in figure 2. According to Hubbert's theory, these sources are not infinite. In 1956, Hubbert developed a model for the oil production, which led to Hubbert's theory. This curve, called the Hubbert curve, has an optimum which estimates the maximum oil production. Since this oil peak is being approached, it is important to develop alternative energy sources [63]. Moreover, the increasing consumption also results in a higher CO_2 emission.

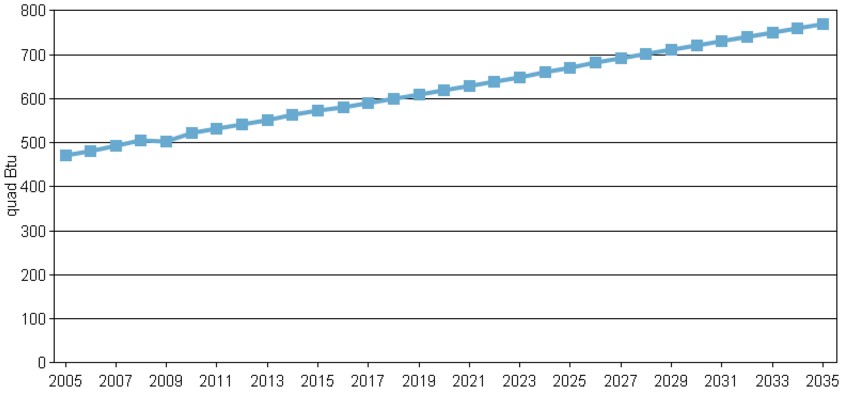

Fig. 2: Worldwide energy use prognosis [18].

Renewable energy sources are regarded as the solution for these main problems [16]. Potential renewable energy sources in which much research has been done, are biomass, hydropower, geothermal, wind and solar energy. At the moment only about 9% of the consumed energy comes from renewable energy sources. It is still difficult for these renewable energies to compete with coal and oil.

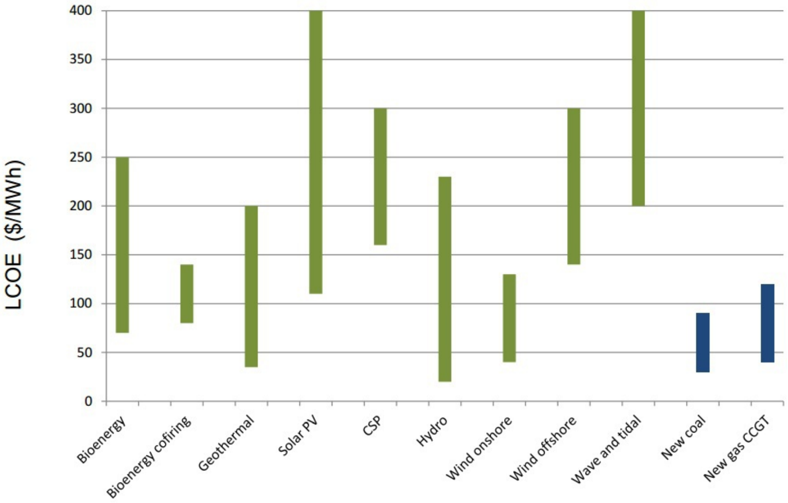

Fig. 3: Levelized Cost of Energy, IEA May 2012 [18].

Solar energy is a promising renewable energy resource due to the combination of its enormous amount of energy and sustainability. As shown in figure 3, the price of solar energy varies significantly, depending on where it is located. To make optimal use of this potential, low-cost solar cells are very interesting.

1.2 Solar energy

In 1839 the photovoltaic effect was discovered by Becquerel [55, 74]. From then on the photovoltaic effect was further developed. Recently, major steps are made in the development of the use of solar energy, accelerated by the depletion of the energy resources, the increased energy demand and the cutback on the greenhouse gas CO_2.

The capacity of the sun to supply energy is many times more than energy consumed on the earth. The emitted power by the sun that reaches atmosphere of the earth is ~ 1.353 kW/m^2, which is called the AM 1.5 solar spectrum shown in figure 4. This emitted power per hour is more than consumed in one year [49]. By covering 4% of the desert by photovoltaics, already enough energy is produced to support the world [18]. That is why the sun is an interesting energy source. However, there are some complications. The transport of energy all over the world is still difficult. Therefore, the placement of solar cells will have to be localized and have to possess a high efficiency. Secondly, the sun does not produce continuous energy supply, which comes hand in hand with the efficient storage problem of energy. Another problem is that the cost of energy converted by solar cells is still relatively high. This thesis will focus on the understanding of the absorption enhancement in the low cost nanostructured thin film solar cells. The future goal is to develop a high efficient, low cost thin film solar cell.

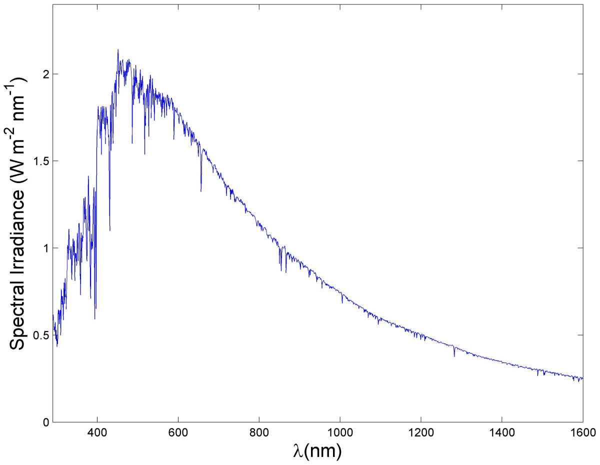

Fig. 4: AM 1.5 solar spectrum, data obtained from NREL [44].

1.3 Shockley-Queisser limit

The main part of a solar cell is an absorber layer, which the energy of converts photons into electron-hole pairs. The amorphous Silicon solar cell contains a p-i-n junction, in which the p-type and n-type regions are doped with holes and electrons, respectively. The i-type region is the intrinsic region [40]. The electron-hole pairs are extracted by the electric field of p-i-n junction and then collected by the electrodes, forming a current when connected to an external circuit. In general, a semiconductor is used as the absorber. When the photon has a lower energy than the band gap ($h\nu < E_g$) it is not absorbed. Photons with an energy higher that the band gap of the semiconductor can be absorbed ($h\nu > E_g$). These photons induce electron-hole pairs and can conduce to the current [76]. After exciting an electron-hole pair, the pair is separated by an internal electric field. Consequently, an electrical current is produced by the solar cell [55]. To guide the electrons into the external-circuit current (I_{sc}), conducting layers are needed at the back and on top of the solar cell (figure 5).

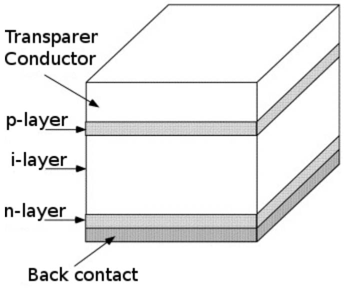

Fig. 5: Structure of a p-i-n solar cell [15].

In theory, every absorbed photon will induce one electron-hole pair which contributes to the current. The quality of the solar cell is determined from the $I-V$ curve. The maximum producible current is given by I_{ph}, and the actual current by I_{sc}, the short-circuit current. The open-circuit voltage of the solar cell is given by V_{oc}. The fill factor (FF) is determined by the shape of $I-V$ curve (the yellow plane in figure 6). By multiplying I_{sc}, V_{oc} and FF, the maximum power at the maximum power point (MPP) can be obtained. A typical $I-V$ curve is shown in figure 6.

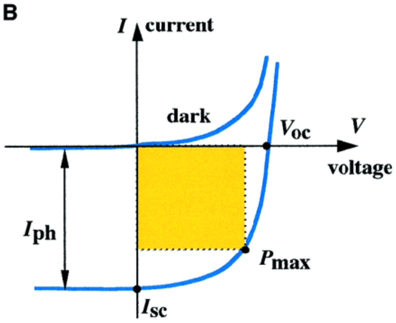

Fig. 6: $I-V$curve of a solar cell, where I_{sc} is the short-circuit current, I_{ph} is the electric current density, V_{oc} is the open-circuit voltage and P_{max} is the electrical power of the cell at the maximum power point [55].

The quality of the solar cell is determined by the limits of the cell. The theoretical limit of the solar cell, is the so-called the Shockley-Queisser limit and is ~31%. This was established by William Shockley and Hans Queisser in 1961 [58]. It is based on the physical losses of the solar cell, blackbody radiation, recombination of the separated electron-hole pair, spectral losses and other small losses like shading of the front contacts. The spectral losses are mainly in the red and near infrared region. Blue photons have a high energy, and therefore a small wavelength ($E = \frac{hc}{\lambda}$). Thus these photons cannot travel far through the absorber layer before being absorbed. On the other hand, red photons have a low energy and hence a long wavelength. Now, the absorber layer needs to be very thick in order to absorb these photons. However, the thicker the absorber layer, the higher the recombination rate of the separated electron-hole pairs. Therefore, it is important to find an equilibrium between the highest absorption of photons and the lowest recombination rate. Recent achievements on solar cells are listed by the National Renewable Energy Laboratory (NREL), shown in figure 7 [44].

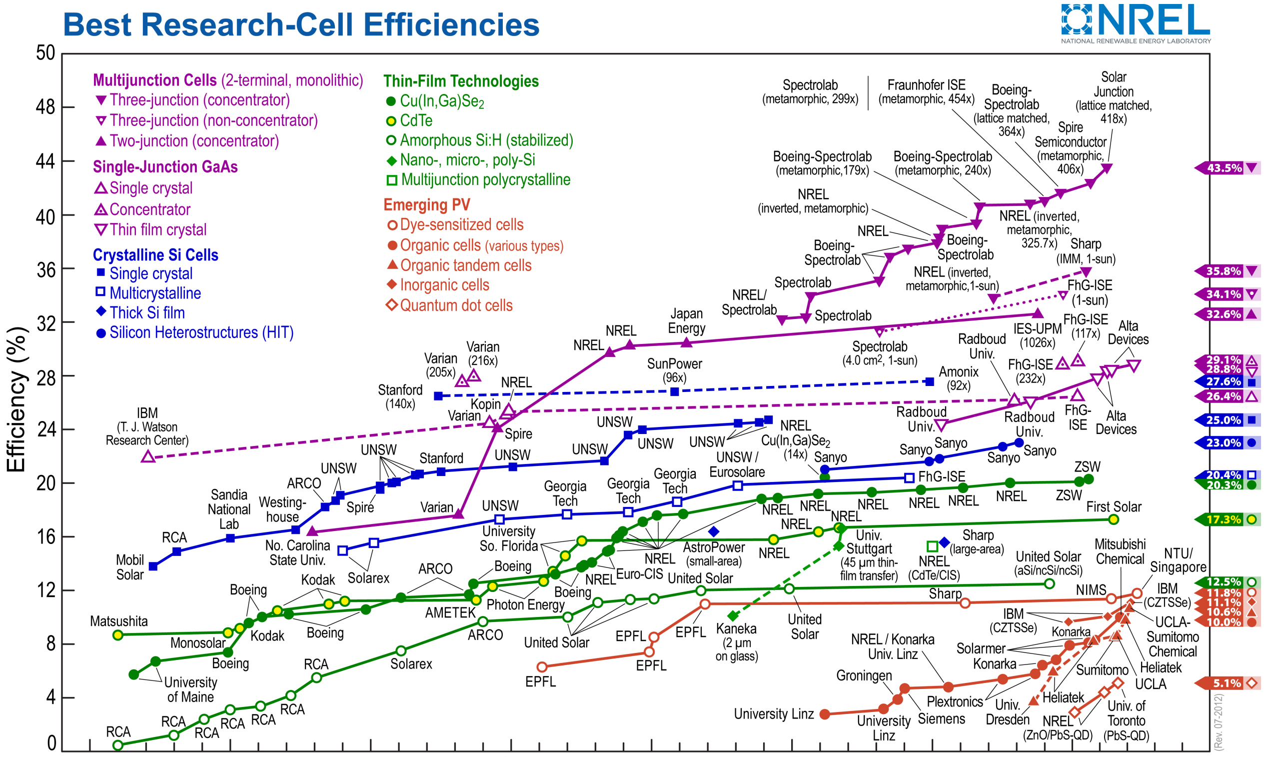

Fig. 7: Best research-cell efficiencies [44].

1.4 Thin film a-Si:H solar cells

Silicon is a widely used light absorbing semiconductor material. Both crystalline and amorphous silicon are suitable for solar cells, and also intermediates like microcrystalline. In the beginning, most commercially available solar cells are made from crystalline silicon (c-Si), the band gap is only ∼1.1 eV. Crystalline silicon is a widely used material for electronics technology, and techniques for purifying and manufacturing c-Si are readily available. Therefore, it is straightforward to use silicon for the production of solar cells. Also, c-Si contains less defects than amorphous silicon. Defects cause recombination of electron-hole pairs, hence the produced current by the solar cell is decreased.

In theory, amorphous silicon (a-Si) should have a higher absorption coefficient than c-Si, due to the disordered lattice. However, in realistic a-Si has about the same absorption coefficient as c-Si. The main problem of amorphous silicon is the presence of unsaturated bonds, also known as dangling bonds (figure 8), which causes defect states within the band gap. These bonds cause defects in the absorber layer, which leads to a higher recombination rate and a lower current. To solve this problem, the dangling bonds can be passivized by adding hydrogen. Consequently, the defects in the band gap are removed. The suitable high band gap makes a-Si appealing to use for thin film solar cells. Thin film solar cells suppress the costs significantly [47, 53]. Moreover, the dark current in thin films is decreased, which causes an increased open circuit voltage [61]. Another appealing feature of a-Si:H is the deposition temperature. It can be deposited at lower temperature (lower than 500 °C) than c-Si, which reduces the production costs. Due to this lower deposition temperature, the a-Si:H solar cells can also be made on low cost plastic polyethylene naphthalate (PEN) [51].

Material	$E_g$min (eV)	$E_g$max (eV)
c-Si	1.1	1.1
μc-Si:H	1.0	1.2
a-Si:H	1.7	1.8

Tab. 1: Band gap range of crystalline, microcrystalline and amorphous silicon [51].

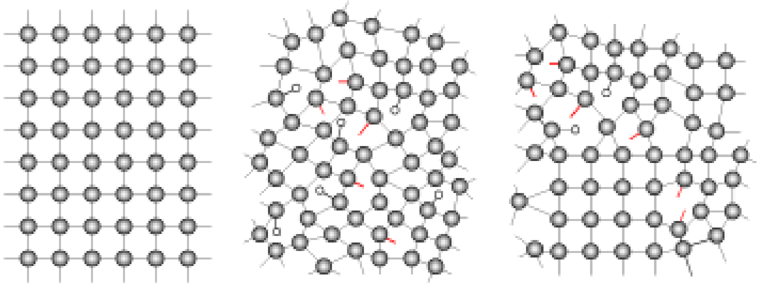

Fig. 8: Atomic structures of crystalline silicon, amorphous silicon and microcrystalline silicon [9].

It seems a-Si:H is the right candidate for solar cells. It has a high band gap energy and can be manufactured at low temperature. Additionally, the costs are lowered considerably. Unfortunately, the efficiency of a-Si:H based solar cells decreases after light exposure, due to the Staebler-Wronski effect [56]. This effect is a light-induced increase in defects in the a-Si:H layer. Wafer based c-Si solar cells, on the other hand, are more stable. However, there is always a trade-off between price and efficiency of the solar cell. This trade-off is described in price per Watt-peak ($\eta \cdot 1000 \left[\frac{\text{W}}{\text{m}^2}\right] \cdot A$), the generated output by illuminating 1000 W/m^2 [6]. In order to compete with other alternative sustainable energies, the price per Watt peak should be as low as possible. Therefore, it is necessary to optimize a-Si:H based solar cells for enhanced performance.

1.5 Applications of nanostructures in thin film solar cells

When making a thin film solar cell, the thickness of the absorber layer is decreased. This technology is used due to two important benefits. First of all, the production costs are reduced by the decreased required amount of material. Secondly, the electrical properties of the solar cell are improved by decreasing the recombination probability of an electron hole pair. On the contrary, the photon absorption is reduced due to the thinned absorber layer. Following from the low absorption coefficient of a-Si:H in the red and infrared region. Rather than increasing the absorber thickness, an alternative approach is the exploration of advanced light trapping schemes. A recent technique to trap light is to make the usage of (plasmonic) nanostructures at the rear side of the cell [13, 39, 59, 78, 79]. Hereby the absorption can be increased mainly in the red region. Blue photons can easily be trapped without using light trapping schemes. This nanostructuring at the back has several effects. Primarily, the nanostructures scatter radiation into large off-normal angle thus the path length of light in the absorber layer is significantly increased. Therefore the absorption possibility of photons is enhanced. Secondly, in some elongated nanostructures like nanowires and nanorods, the light travel path and the carrier extraction path are orthogonalized. In this way the absorption and carrier collection are improved simultaneously. The highest loss of absorption is in the red region. Nanostructures can increase the absorption in this region in two ways. Constructive interference due to the nanostructures causes absorption peaks in the red region. Furthermore, plasmonic light trapping can be obtained by well-designed structures, and increase absorption in this region [61]. The plasmonic effect describes the interaction between photons and a nanostructured metal surface and will be explained further in the next chapter.

Two nanostructured systems are studied in this thesis. The first studied system is a nanorod solar cell. In this system, the light travel path and the carrier transport path are assumed to be orthogonalized. In addition, an anti-reflection effect at the top surface and a strong light scattering inside the cell are demonstrated [3, 22, 61]. Thereby the thickness of the absorber layer can be very thin to reduce material cost, increase the throughput of the deposition system and make the cell more stable.

Another interesting system is the solar cell with a back contact contain nanohole. This nano textured system has the special property to generate both surface plasmons and plasmonic scattering. Therefore, this structure could lead to an enhanced response [5]. The red region is the most interesting part of the solar spectrum for a-Si:H since it exhibits a very weak absorption ability in this region and light trapping schemes is even more crucial for improving absorption.

1.6 Outline of this thesis

This thesis will comprise the study of two solar cells with different nanostructered back contacts. First some general theory about solar cells will be given, followed by the theory of the plasmonic effects, FDTD simulations and specifically simulations of thin film solar cells will be covered in more depth. The two studied nanostructured solar cells are a nanorod based solar cell and one containing nanoholes in the Ag back contact. For the first structure both the synthesis of ZnO rods on a polyethylene naphtalane (PEN) substrate as well as the simulations on its absorption behavior will be investigated. The different synthetic parameters will be studied to see their effects on the morphology of nanorods. From the simulated solar cell, the absorption behavior will be studied and an optimization will be performed using FDTD simulations. The second structure will only be studied through FDTD simulations, where the diameter of the nanohole will be varied. From the results the origin of the absorption spectrum and possible plasmonic effects of the solar cell will be determined. The thesis will be concluded with a summary of all results and based on these results a proposal for a low cost, high efficient solar cell will be given.

2 Theory

2.1 Abstract

In the first section, the fundamentals of plasmonics are explained. The plasmon modes are explained and different plasmonic effects are discussed. Subsequently, plasmonics in solar cells are discussed. The second section will explain the FDTD simulation program and the settings. In the last section, the FDTD simulations for a thin film solar cell are discussed. Two examples are shown to explain how FDTD can be applied on a-Si:H thin film solar cells.

2.2 Plasmonics

2.2.1 Fundamentals

The earliest and most famous example of a plasmonic effect is the Roman Lycurgus cup, shown in figure 9 [43]. A glass cup that changes from color when illuminated from the back or the front, due to plasmonic nanoparticles. Since the plasmonic effect can occur in noble metals due to their unique properties, prior to the explanation of this plasmonic effect, their optical properties will be discussed.

Fig. 9: The Roman Lycurgus cup [43].

A metal can be seen as a positive lattice, with negative electrons moving through the lattice. According to the Drude model, the electron can be seen as free electrons, hence there is no interaction between the electrons and the lattice nor between the electrons mutually. Often, a metal contains one or two conduction electrons which can move like free electrons. The Drude-Sommerfeld theory is a complement to the Drude model. This model combines the free electron model with Fermi Dirac statistics, in which electrons can be described as fermions. From this theory, the angular frequency dependent dielectric function can be derived [37, 43]. The dielectric constant can be divided into a real and an imaginary part ($\varepsilon = \varepsilon^{'} + i\varepsilon^{''}$):

$$\varepsilon_{Drude}(\omega) = 1 - \frac{\omega_p^2}{\omega^2 + \Gamma^2} + i\frac{\Gamma\omega_p^2}{\omega(\omega^2 + \Gamma^2)} \tag{1}$$

where ω is the angular frequency and ω_p the volume plasma frequency ($\omega_p = \sqrt{\frac{ne^2}{m_e\varepsilon_0}}$) [43]. The damping term is given by $\Gamma = \frac{v_F}{l}$ with v_F representing the Fermi velocity and l the electron mean free path. The dielectric constant is divided into real and imaginary parts. The energy gain in the metal is given by the real part and the imaginary part represents the energy losses in the metal. Resulting from the Drude-Sommerfield model, the real part is negative and the imaginary part positive, as shown in figure 10a. Consequently, this combination of the real and the imaginary part explains that light can only penetrate the metal superficially [43].

In order to make this model suitable for both low and high energy photons, a correction is needed. The Drude-Sommerfeld model neglects the excitation of lower-lying electrons to the conduction band due to energetic photons. Therefore, the Drude-Sommerfeld theory is not accurate for the optical properties of metals in the visible regime, as shown in figure 10b. Similar to the free electron model, the angular frequency dependent dielectric constant of excited electrons can be determined [43].

$$\varepsilon_{interband}(\omega) = 1 + \frac{\tilde{\omega}_p^2(\omega_0^2 - \omega^2)}{(\omega_0^2 - \omega^2)^2 + \gamma^2\omega^2} + i\frac{\gamma\tilde{\omega}_0^2\omega}{(\omega_0^2 - \omega^2)^2 + \gamma^2\omega^2} \tag{2}$$

where $\tilde{\omega}_p$ is the plasma frequency of the bound electrons ($\tilde{\omega}_p = \sqrt{\frac{\tilde{n}e^2}{m\varepsilon_0}}$) and $\omega_0 = \sqrt{\frac{\alpha}{m}}$ [43]. This leads to a contribution to the dielectric constant shown in figure 10b. Together, these two models make an accurate approximation of the angular frequency for both short and long wavelength.

An important question is how light can couple to these plasmon modes. In order to find the conditions it was postulated that energy and momentum conservation should be taken into account. The oscillations of the free electrons are quantized in a quasi-particle called a plasmon. Due to photons at optical frequency, these plasmons at the surface can be excited, also called surface plasmon polaritons (SPPs). The wave vector of the SPP represents the direction of the propagation of the wave. To study the conditions for light coupling to a plasmon mode, the interface between two media is observed. ε_m represents the dielectric constant of the metal and ε_d which is assumed to be real for a simplified model. In order to propagate a SPP over the interface, the following two conditions are required for these dielectric constants [43]:

$$\varepsilon_m(\omega) \cdot \varepsilon_d(\omega) < 0 \tag{3}$$

$$\varepsilon_m(\omega) + \varepsilon_d(\omega) < 0 \tag{4}$$

Another requirement for inducing a SPP is the larger wave vector of the photon with respect to the wave vector of light in free space. Due to the conservation of momentum and energy, the plasmon can only be excited when the wave vector of the photon is large enough to couple to the plasmon. Subsequently, after coupling a SPP is excited, which can propagate over the surface. The wave vector can be divided in a real and an imaginary part ($k_{spp} = k' + ik''$). The wavelength needed to excite the plasmon is determined by the real part and the damping of the plasmon is determined by the imaginary part [2]:

$$k^{'} = k_0\sqrt{\frac{\varepsilon^{'}_m \varepsilon_d}{\varepsilon^{'}_m + \varepsilon_d}} \tag{5}$$

$$k^{''} = k_0\sqrt{\frac{\varepsilon^{'}{}_m \varepsilon_d}{\varepsilon^{'}{}_m + \varepsilon_d}}\,\frac{\varepsilon^{''}_m \varepsilon_d}{2\varepsilon^{'}_m(\varepsilon^{'}_m + \varepsilon_d)} \tag{6}$$

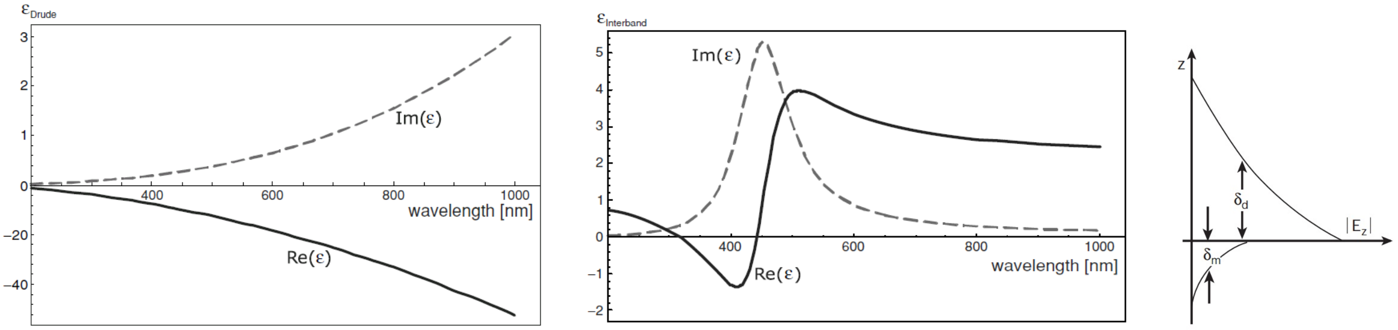

(a) (b) (c)

Fig. 10: Characteristic metal properties. (a) Real and imaginary parts of energy gain in gold [43]. (b) Contribution excitation lower-lying electrons in gold [43]. (c) A characteristic propagation length of SPP at metal-dielectric surface in the metal (δ_m) and the dielectric medium (δ_e) [2].

Here the real part of the wave vector (k') determines the wavelength of the SPP mode ($k' = 2\pi/\lambda_{spp}$) at the wavelength of light in free space (λ_0) , which defines the wave vector in free space ($k_0 = 2\pi/\lambda_0$). From this it can be derived that the decay length of the plasmon is shorter in the metal than in the dielectric medium (figure 10c). The plasmon wave vector depends on the metal and its band structure and describes the momentum needed to couple.

To overcome this momentum mismatch, the diffraction effects of roughening, grating or patterning the metal surface can be used. Due to the grating, a reciprocal wave vector is added to the system. Now SPPs are induced by the incoming photons. The short wavelength of the photons that couple to the plasmons ensure that the grating has to be in the same order. Therefore nanostructures are used as plasmon guides. Size, shape and grating of the nanoparticles and the dielectric environment can shift the plasmonic peak to other wavelengths [2, 41]. Studies have been performed to control the shift of the SPPs by changing these parameters. In order to couple to SPPs, the phase-matching condition is [37]:

$$\beta = ksin\theta \pm \Delta k_x \tag{7}$$

where β is the SPP propagation constant, k is the wave vector and k_x is the momentum components. An important point to note is that thin film metals can generate surface plasmons at the front and the back of the metal [46]. Surface plasmons which are reflected between two barriers will collapse from running waves into standing waves, consequently a localized surface plasmon is obtained [24, 32]. These often arise due to the presence of conductive nanoparticles or can be caused by a nanostructured surface.

Another way to use plasmonics is by nanoparticles. Photons can couple to these particles and instead of inducing a surface plasmon, plasmon scattering is generated. In order to have a plasmonic effect, the radius of the particle (a) should be significantly smaller than the wavelength of the photon ($a \ll \lambda$) [37]. Therefore, the plasmon modes are controlled by the size and shape of the particles, as shown in figure 11. In general, the plasmon resonance shifts to the red region when the particle radius increases, though this only applies for a single particle on a surface [25]. When the particles are close to each other, near-field coupling of the plasmon resonances between the particles can take place. Now, the particles serve as waveguides and the distance between the nanostructures can influence the SPP resonance. Former research has shown that plasmon resonance occurs at only a few kinds of nanoparticles: spheres, ellipsoids and infinitely long circular cylinders [4].

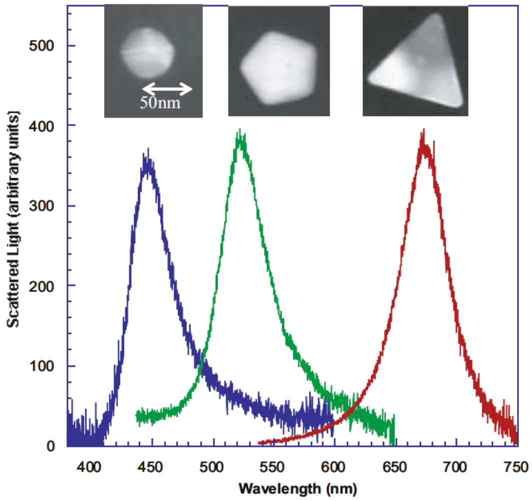

Fig. 11: The SPP resonance peak depends on shape and size of the nanoparticle [37].

2.2.2 Plasmonic solar cells

Plasmonic nanostructures can be applied in solar cells. The first appealing feature, is that the SPP resonance peak can be shifted to the red region by tuning the particle, as discussed in the previous paragraph. In this red region, large absorption losses of solar cells take place due to the low absorption coefficient of a-Si:H at long wavelength. Therefore SPP resonance can reduce these losses. The plasmons can also offer three distinct effects to enhance the absorption in the a-Si:H i-layer. The photons can be scattered into the cell in different directions, by nanoparticles placed on top of the solar cell (figure 12a). Due to this scattering into different directions, the optical path length will be extended and the absorption will be increased. Secondly, due to localized surface plasmon resonances, near-field enhancement can occur (figure 12b). Scattering of the nanostructures into the a-Si:H layer can be caused, which can be absorbed to increase the efficiency of the solar cell. These enhanced radiation spots are the so called 'hot spots'. The hot spots can only couple to the a-Si:H absorber layer, when the metal and the a-Si:H are close to each other. The final effect that can be caused by nanostructures, is the propagation of SPPs over the interface between the metal and the a-Si:H (figure 12c). In this case, the plasmonic structures serve as waveguides sub-wavelength scale, to propagate the SPP modes over the interface [2, 12, 37, 41, 47, 68]. Another interesting feature is that the absorption path can be orthogonalized by using nanostructures. In a nanorod structure, light is absorbed in vertical direction and electron hole pairs are collected in horizontal direction. Due to this separation of photon absorption and carrier collection, the photon path is elongated and the carrier path is reduced [42].

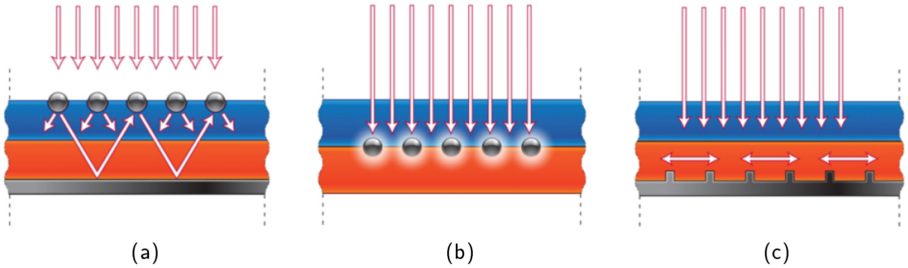

Fig. 12: The three ways of absorption enhancement in a solar cell thanks to the plasmonic nanostructures [12]. (a) Scattering into the cell caused by nanostructures on top of the cell. (b) Localized surface plasmon resonances can cause high near-field enhancement. (c) SPPs can be propagated on at the interface of the metal and the dielectric medium.

Besides the scattering of the metal, photons can also be absorbed by the metal due to the localized surface plasmon mode. This could lead to the ohmic losses in the solar cell. This means that a photon is lost, because of absorption in the metal which is converted into heat. Therefore, it is important to optimize the plasmonic nanostructures to maximize the back scattering, and minimize the ohmic losses [12].

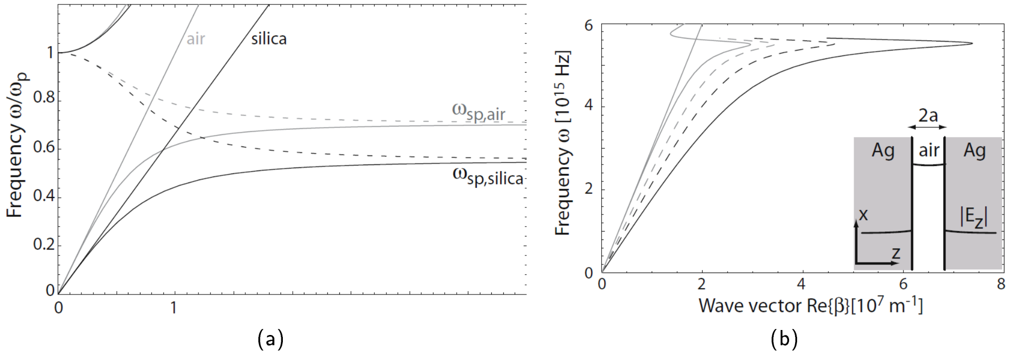

Fig. 13: Some properties of plasmonics. (a) Light at normal incidence on a flat metal surface cannot couple to the plasmon modes, because of an energetic mismatch, shown for air and a-Si:H. (b) A nanostructure at the surface of a metal can overcome the energy mismatch, and plasmonic coupling can supply. [37]

An interesting nanostructure for the back contact of solar cells is a metal with a grating of nanoholes. On one hand, these nanoholes can provide a reciprocal lattice vector to generate coupling to the surface plasmon modes, as shown in figure 13b. In addition, the nanoholes can induce plasmonic scattering within the nanohole, leading to Fabry-Perot type oscillations and Mie scattering [5, 24, 28, 38]. A nanohole can be considered as an anti-particle [12]. Therefore, nanoholes can have the same effect as nanoparticles, i.e., elastic scattering can be caused by the nanoholes, though the plasmon modes are shifted [28, 35]. The Mie scattering in the nanohole, also known as hole plasmon resonance or plasmon resonators, can be explained by coupling of the surface plasmons inside the nanohole can take place. The configuration of these surface plasmons can be bonding and antibonding as shown in figure 14a [46]. However, another way to approach this plasmonic effect is considering the hole plasmon resonance as a locally trapped standing wave propagated in the nanohole, shown in figure 14b. Applied to a solar cell, these holes can cause localized absorption enhancement in the photo active layer. It is important to take both plasmon effects into account to optimize this nanostructure. The surface plasmons depend on the pitch of the nanoholes, on the other hand the plasmon scattering on the size and shape of the hole, together these properties will lead to confinement [24]. Therefore, these parameters will have to be optimized for maximum scattering and coupling of surface plasmons to the photo active layer.

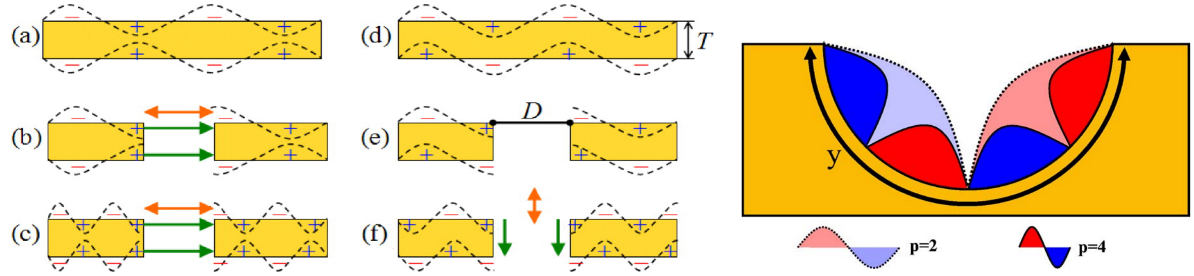

(a) Coupling of surface plasmons within a nanohole for a thin film metal. The charge configuration og the modes can be bonding, shown in figure a-c, and anti-bonding, shown in figure d-e. Ligt can couple to both configurations [46].

(b) propagation of a localized plasmon in the nanohole [24].

Fig. 14: Distinct plasmonic effects in nanoholes

A periodic nanohole structure can generate both surface plasmons and plasmon scattering. On the contrary, random distribution of holes on a surfaces lower the absorption intensity per surface plasmon mode. On the other hand, more scattering plasmons are induced due to multiple scattering paths [24, 69].

2.3 Finite-Difference Time-Domain Simulations

2.3.1 Fundamentals of FDTD

The Maxwell equations describe the interaction between photons and a metal surface. Certain boundary conditions are used to solve these equations. These are complex calculations, and are extremely difficult to do analytically. Another more simple way to calculate what happens, is by using Finite-difference time-domain (FDTD) simulations, which are often used to study plasmonic effects [32]. These FDTD simulations are based on solving the Maxwell equations, these relate Electric field (E) and magnetic field (B) to charge (ρ) and current (J). The simulations are done by the commercial available software from Lumerical [33]. This technique is time domain, meaning the Maxwell equations are derived to time [33].

$$\frac{\partial \overrightarrow{D}}{\partial t} = \nabla \times \overrightarrow{H} \tag{8}$$

$$\overrightarrow{D}(\omega) = \varepsilon_0 \varepsilon_r(\omega) \overrightarrow{E}(\omega) \tag{9}$$

$$\frac{\partial \overrightarrow{H}}{\partial t} = -\frac{1}{\mu_0} \nabla \times \overrightarrow{E} \tag{10}$$

Where $\overrightarrow{D}$, $\overrightarrow{H}$ and $\overrightarrow{E}$ are displacement, magnetic and electric fields, respectively, and $\nabla\times$ the curl operator. The electric permittivity and magnetic permeability are given by ε_0 an μ_0 and the complex relative dielectric constant is given by $\varepsilon_r(\omega) = n^2$, with n =refractive index). Since it is assumed that the fields are independent of z ($\varepsilon_r(\omega, x, y, z) = \varepsilon_r(\omega, x, y)$), and the structure is assumed to be infinite in z direction, the z dimension of the equations can be omitted [33]:

$$\frac{\partial \vec{E}}{\partial z} = \frac{\partial \vec{H}}{\partial z} = 0 \tag{11}$$

Now the equation merely has to be splitted into x and y direction. Thereby it can be divided into an electric part (transverse electric, TE) and a magnetic part (transverse magnetic, TM). These consist of E_x, E_y, H_z and H_x, H_y, E_z respectively.

The Maxwell equations are confined by space and time, which makes these calculations finite-difference. The space is defined by small boxes in the order of 10 nm^2, called Yee cells named after the founder of the principles of FDTD (figure 15). These cells are constructed from the electric fields (E), located at the edges, and the magnetic fields (H) at the faces. Together this large number of Yee cells form the simulated region. Time is confined by the time needed for the electric and magnetic fields to go through a Yee cell. The cells can be specified in material properties, number and size.

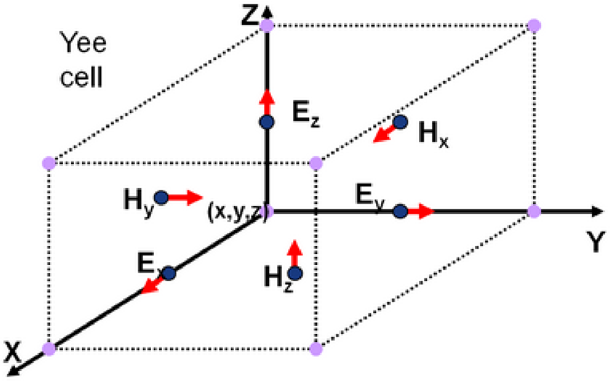

Fig. 15: Yee cell [33].

The size of the Yee cell is defined by the mesh size, this also decides the smoothness of the shape. Therefore, the smaller the mesh size, the more accurate the calculations. However, the smaller the size, the more time-consuming and memory demanding for the calculations. Consequently, it is necessary to find a balance between accuracy and time. Another way to restrain time, is by using a non-uniform FDTD mesh. In order to determine the best settings, a convergence test is required.

These calculations can be done in both two dimension (2D) and three dimensions (3D). Other different parameters should be chosen carefully to results into correct simulations, i.e., boundary conditions, material properties and light source. These parameters will be discussed in the following paragraphs [33, 75].

2.3.2 Boundary conditions

It is important to choose the correct boundary condition of the simulation region. They determine the kind of region that is simulated. For example, one nanovoid can be extended to a periodic structure with nanovoids. Also, the photon reflection can be continued through the boundaries, absorbed or even be reflected by the boundaries. It is important to take the light source into account, i.e., perfectly matched layer (PML) boundaries are best to use for absorbing boundaries at normal incidence. On the other hand, these PML conditions are not suitable for grazing incidence, since there will be a significant reflection due to these boundaries. In order to make one structure periodic and therewith have periodic EM fields, the bloch boundary conditions are suitable [33, 75].

2.3.3 Material properties

The most decisive parameters for the FDTD calculations are the material properties. Therefore, $\varepsilon_r(\omega)$, the relative permittivity, is an important value to solve the calculations. It consists of a real and an imaginary part [37]:

$$\varepsilon(\omega) = \varepsilon_1(\omega) + i\varepsilon_2(\omega) \tag{12}$$

$$\varepsilon_1 = n^2 - k^2 \tag{13}$$

$$\varepsilon_2 = 2nk \tag{14}$$

$$n = n_1 + in_2 \tag{15}$$

From here, it shows that the calculations strongly depend on the n- and k-values of the material, the refractive index and the extinction coefficient respectively. Based on these properties, a fit plot of the real and the imaginary part of the materials can be made. These are used for the simulations.

FDTD contains a wide material data base of polynoom fits of standard materials. The fit plots of these materials are made by using different models, i.e., the Drude, Debye and Lorentz model. The fit plot that corresponds to the experimental used material, should be used. Also, sampled data can be added by importing the n- and k-values of the material [33, 75].

2.3.4 Light sources

Different sorts of light sources can be chosen in FDTD, i.e., point sources, Gaussian and thin lens sources, and plane wave sources. When measuring the consequences of solar radiation, the plane wave source can be used. The choice of boundary conditions is strongly determined by which light source is used [33].

2.4 Thin film solar cell and FDTD

The a-Si:H thin film solar cell creates the opportunity to reduce the production cost by decreasing the required amount of material. However, due to the thin absorber layer, these solar cells have a low photon absorption in red and infrared region. The absorption of the blue photons can be described by the Lambert-Beer Law in approximation. This Law describes the dependence of penetration depth on the material specific absorption coefficient and is described by the following equation [14]:

$$I(\lambda) = I_0(\lambda)\mathrm{e}^{-\alpha(\lambda)x} \tag{16}$$

where I_0 and α are the incident intensity and the absorption coefficient, respectively. x represents the depth on which the intensity (I) is measured. The absorption coefficients of several materials are shown in figure 16. It can be calculated according to this equation [49]:

$$\alpha(\lambda) = \frac{4\pi k}{\lambda} \tag{17}$$

Where k is the extinction coefficient and λ is the wavelength in cm. Due to the high absorption coefficient of a-Si:H at short wavelength, almost all photons are absorbed before reaching the back contact of the solar cell. Photons of longer wavelength will be reflected by the back reflector of the solar cell.

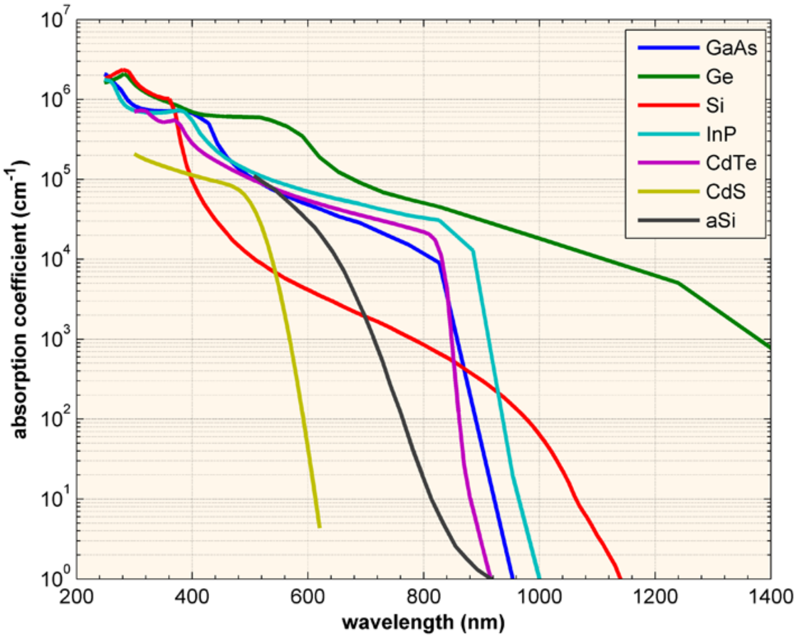

Fig. 16: Absorption coefficient of several materials [49].

The absorption in thin film solar cells can be studied by using FDTD simulations. The absorption cross sections can be calculated from the results of the simulations. The wavelength of the incoming photons changes in a-Si:H, due to the different refractive index. This wavelength can be derived from the absorption cross sections. Thereby, the wavelength in a-Si:H can be calculated theoretically according to this formula:

$$\lambda_{Si} = \lambda_{air} \times \frac{n_{air}}{n_{Si}} \tag{18}$$

Where λ_{Si} and λ_{air} are the wavelength in a-Si:H and air, respectively. n_{air} and n_{Si} are the refractive indexes of air and a-Si:H, respectively. It is important to note that the refractive index of a-Si:H is wavelength-dependent, for which the refractive index of the FDTD database is used. The interference analysis is executed using the following method: the wavelength in a-Si:H (λ_{Si}) is derived from the distance between two absorption maxima ($1/2\lambda_{Si}$). The wavelength in the a-Si:H layer will be calculated by using equation 18.

In this thesis, two differen nanostructured thin film solar cells will be studied. In order to understand the influence of the nanostructures with respect to a flat thin film solar cell, two different flat solar cells are simulated by using FDTD. In addition, the influence of different p-i-n junction and the ZnO layer thickness will be shown here. Both samples correlate to the later on simulated nanostructured solar cells. The schematic cross section of one of the flat solar cells is shown in figure 17a with the details of the structure. This structure will be related to the nanorod solar cell in Chapter 4. The total absorption and the absorption in the a-Si:H i-layer are shown in figure 18. The absorption in the a-Si:H i-layer, is of interest for the obtained current density of the solar cell. The absorption coefficient of a-Si:H at short wavelength is high. Therefore, based on the Lambert-Beer Law, high absorption in the i-layer at short wavelength is expected [72]. Due to the high absorption of the ITO layer at this wavelength, this high absorption in the i-layer is not obtained. Two absorption optima appear in the absorption spectrum, which are probably originated from optimal constructive interference. The absorption cross sections at different wavelengths are shown in figure 17. At shorter wavelength, strong constructive interference is observed as shown in figure 17b, 17c and 17d. At longer wavelength, lower constructive interference is obtained as shown in figure 17e and 17f and is in agreement with literature [7, 12, 29]. The wavelength determined by the absorption maxima and minima are measured and converted to wavelength in nanometer, which is called the observed wavelenth. On the other hand, the incoming wavelength (λ_{air}) is converted to the wavelength in a-Si:H (λ_{Si}) and compared to the observed result, as listed in table 2.

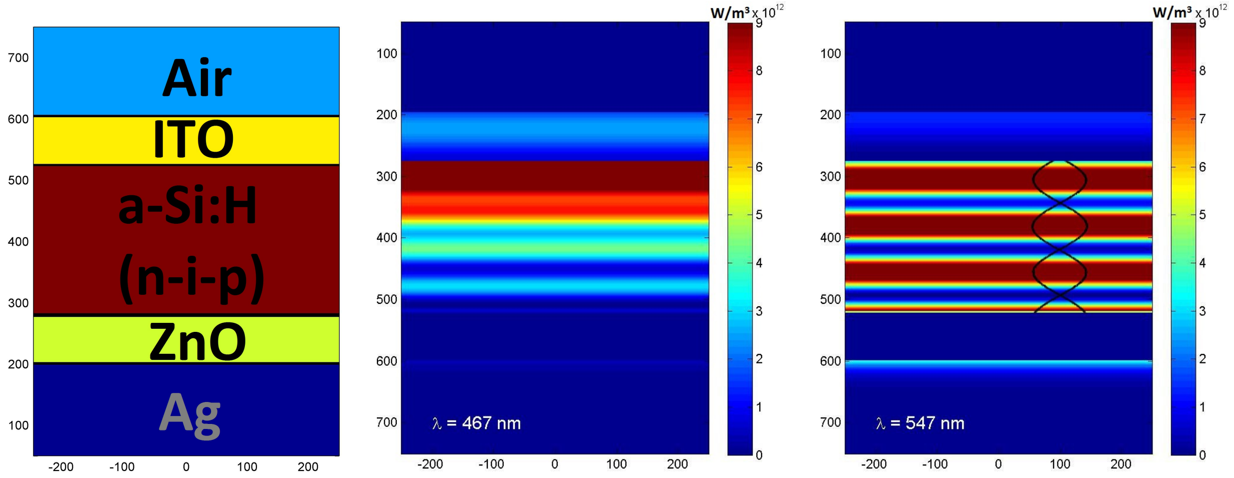

(a) Schematic cross section. (b) (c)

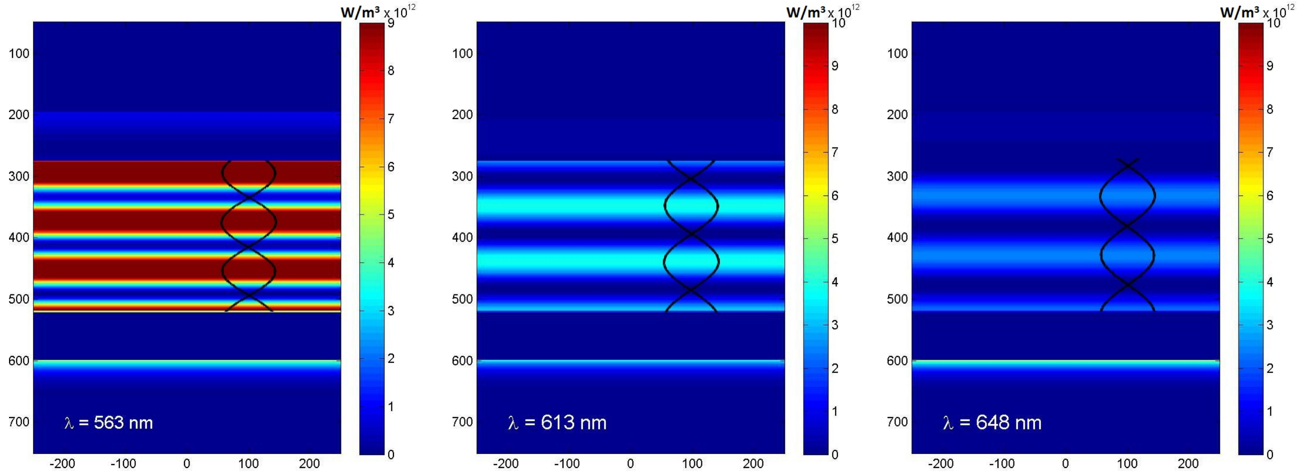

(d) (e) (f)

Fig. 17: Absorption cross sections of a flat solar cell including interference patterns, with 200 nm thick Ag layer, 80 nm thick ZnO layer, 245 nm thick n-i-p junction (30 nm, 200 nm and 15 nm thick respectively) and 80 nm thick indium tin oxide (ITO). The wavelength in the a-Si:H i-layer is determined by measuring the distance between the absorption maxima. In this figure, these wavelengths are noted by a sinusoidal wave.

λ_{air} (nm)	$n_{Si}(\lambda_{air})$	Calculated λ_{Si} (nm)	Observed λ_{Si} (nm)
547	3.634	150.5 ± 5.4	150.8 ± 5.4
563	3.579	157.9 ± 5.4	157.1 ± 5.4
613	3.415	179.5 ± 5.4	175.9 ± 5.4
648	3.335	194.3 ± 5.4	204.9 ± 5.4

Tab. 2: Analysis of the wavelengths in the absorption cross sections. The calculated wavelengths are calculated according to equation 18 and the observed wavelengths are the wavelengths derived from the observed absorption maxima and minima.

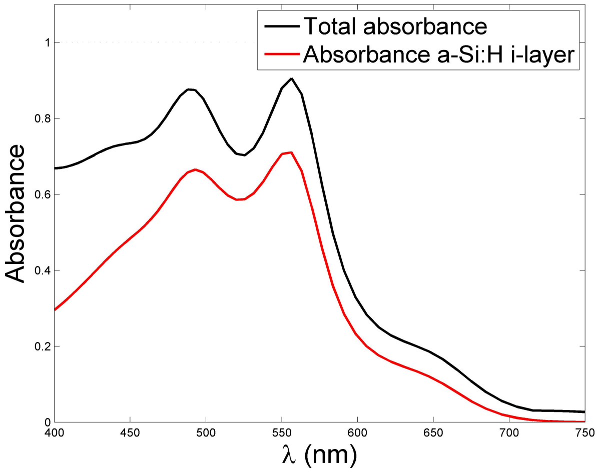

Fig. 18: Absorption in the thin film solar cell of the total cell and the absorber layer (a-Si:H i-layer).

The schematic cross section of the second structure is shown in figure 20a. This structure will be related to the nanohole solar cell in Chapter 5. The optima of the absorption curves of this sample are shifted to different wavelength significantly, as shown in figure 19. Due to the changed thickness of the n-i-p junction and of the ZnO layer, the optimal constructive interference occurs at different wavelength. The absorption cross sections of this flat solar cell at varying wavelengths are given in figure 20 and the analysis is listed in table 3, and correspond to literature [7, 12, 29].

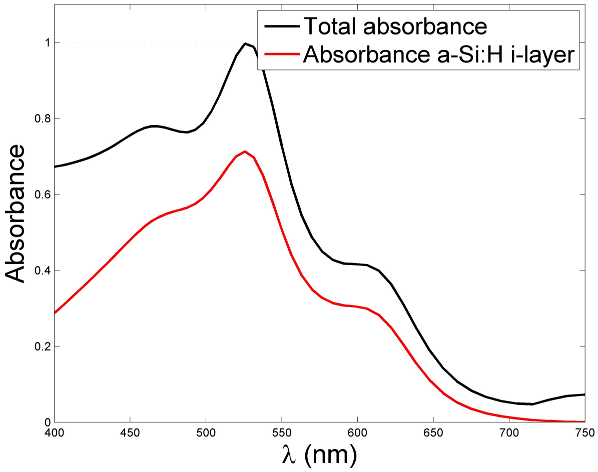

Fig. 19: Total absorption curve and absorption in the a-Si:H i-layer of a thin film solar cell.

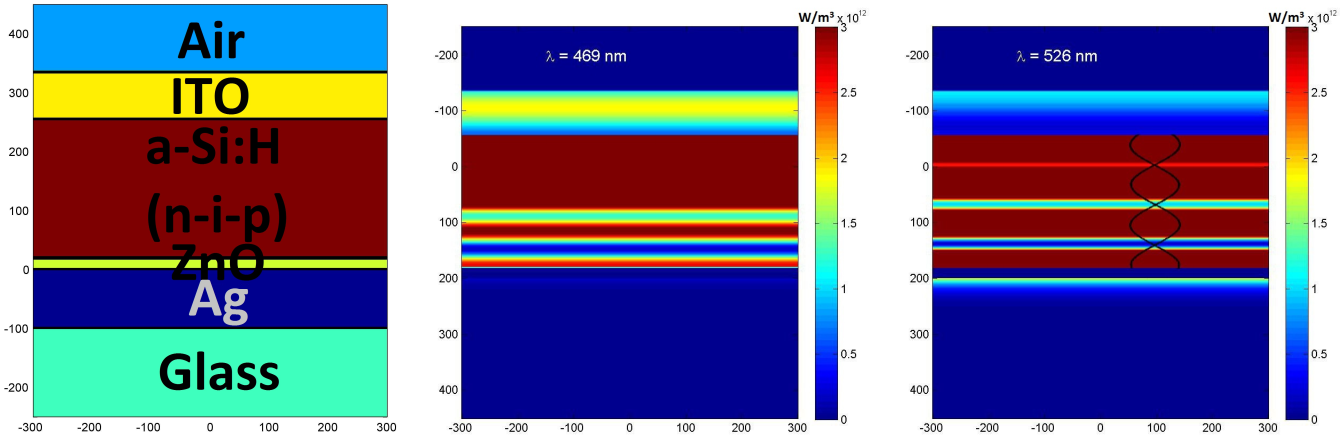

(a) Schematic FDTD cross section.

(b)

(c)

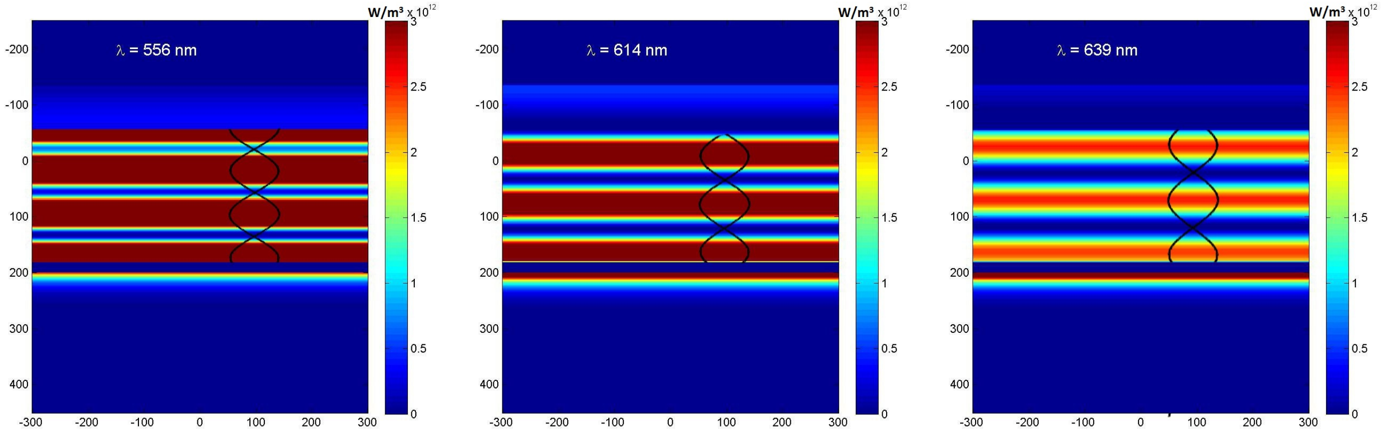

(d)

(e)

(f)

Fig. 20: Absorption cross sections of flat solar cell. The solar cell has a 100 nm thick Ag layer, 20 nm thick ZnO layer, 236 nm thick n-i-p junction (20 nm, 200 nm and 16 nm thick respectively) and 80 nm thick indium tin oxide (ITO). The wavelength in the a-Si:H i-layer is determined by measuring the distance between the absorption maxima. In this figure, these wavelengths are noted by a sinusoidal wave.

λ_{air} (nm)	$n_{Si}(\lambda_{air})$	Calculated λ_{Si} (nm)	Observed λ_{Si} (nm)
526	3.712	141.7 ± 5.4	140.4 ± 5.4
556	3.601	154.4 ± 5.4	156.3 ± 5.4
614	3.415	179.8 ± 5.4	178.6 ± 5.4
639	3.355	190.5 ± 5.4	204.1 ± 5.4

Tab. 3: Analysis of the wavelengths absorption cross sections of figure 20. The calculated wavelengths are calculated according to equation 18 and the observed wavelengths are the wavelengths derived from the observed absorption maxima and minima.

The observed wavelengths of both samples are estimations, which match properly with the theory. Therefore, it can be concluded that this interference analysis correlates suitable for these a-Si:H thin film solar cells. This theory will be applied again in chapter 5.

3 Synthesis of ZnO Nanorods for Solar Cells

3.1 Abstract

In this chapter the influence of the growth parameters on the morphology of the nanorods synthesized by chemical bath deposition are studied. These parameters include seed layer thickness, reactant concentration and growth time. Firstly, the growth mechanism of ZnO rods will be discussed. Secondly, the synthesis of the nanorods and the deposition of the Ag backcontact is described. The morphology of nanorods is characterized by using scanning electron microscopy (SEM). The optical properties of the rods coated with Ag are also studied.

3.2 Introduction

In order to lower the costs of solar cells, it is important to decrease the amount of needed material. One way is to produce thin film solar cells [56]. These thin film cells have a thin absorption layer. However, because of this thin absorption layer, the absorption of the cell is lowered. In order to increase the absorption of the a-Si:H thin film solar cells, light trapping is needed. This conventionally is done by light scatters inside the solar cells, e. g., the textured transparent conducting oxide (TCO) layer . However, in conventional thin film solar cells, there is a trade-off between light absorption and carrier collection. The absorber should be optically thick for absorption in the meanwhile electrically thin for efficient carrier extraction and collection. A nanorod system can solve this problem by orthogonalization of the optical incident path and carrier transport path [23].

Another advantage of the nanorod system is the anti-reflection at the front side due to the very rough top surface rather than mirror-like surface with strong reflection [3, 22, 61]. In addition, light scattering both at the back and the front sides is significantly enhanced because of the steep features of nanorod back reflector and the naturally formed rough front texture.

In this nanorod system, ZnO nanorods are employed as building blocks. ZnO nanorods can be grown via a solution-phase method at low temperature (60 $\sim$ 90°C), the experimental setup is shown in figure 21. The synthetic method is simple and relatively cheap [67]. Through this method the ZnO nanorods can be synthesized on large area substrate due to the independence of vacuum chambers. Due to the low processing temperature, low cost substrate such as plastic polyethylene naphtalane (PEN) is applicable.

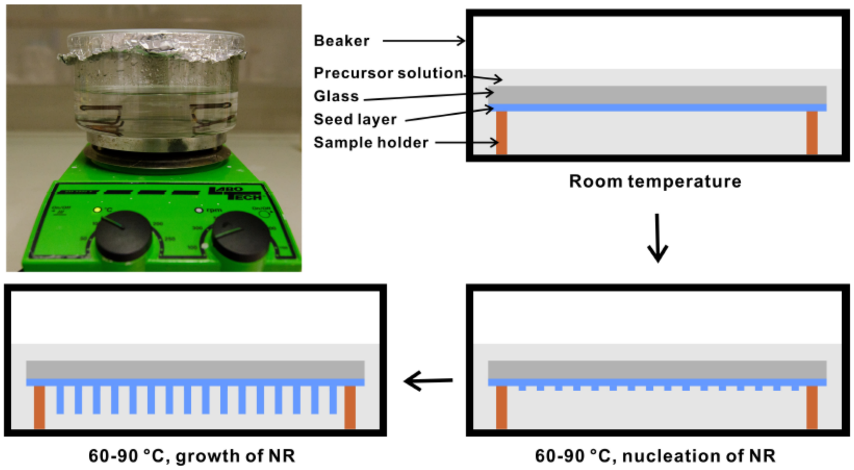

Fig. 21: Experimental setup for the growth of the ZnO nanorods, printed with permission of Yinghuan Kuang's PhD Thesis at Utrecht University.

3.3 The growth mechanism

ZnO nanostructures are widely used in different types of applications [17, 60, 70]. Therefore, several studies have been performed on how to grow these nanostructures. Depending on the preferred morphology, different preparation methods are available. The following methods are commonly used: lithography [21, 45, 52], vapor transport synthesis assisted by vapor-solid (VS) [64, 65] or vapor-liquid-solid (VLS) processes [48, 77], electrochemical deposition [50, 62] and wet chemical methods [11, 76]. Some of the many appealing benefits of wet chemical methods are that the rods can be grown on arbitrary substrates when using a seed layer, the low cost production due to the low temperature and there is less size limitation. Though the controllability of the growth process is relatively more challenging. In general, the nanorods grown by other methods can be better controlled. However, these all suffer from high production cost processes and have size limitations [10, 31, 60].

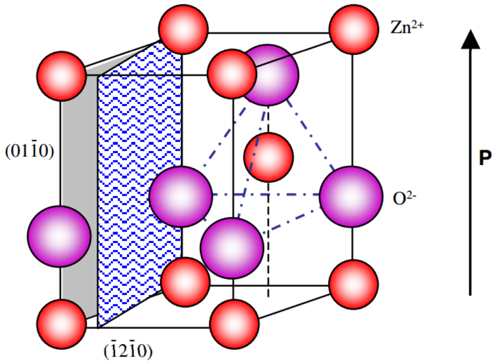

Fig. 22: Wurtzite structure of ZnO [70].

One of the motivations for these nanorod based solar cells, is to suppress the production costs. Therefore, it is interesting to investigate a wet chemical method. The growth of the nanorods is energy driven, the synthesis is developed to achieve a state of lowest free energy. The rods are formed by hydrolysis of zinc salts which crystallizes. Heterogeneous nucleation has a lower activation barrier than homogeneous nucleation, therefore the precipitation rather grow on an existing seed in a layer than remaining in the bulk of the solution. The linear growth can be assigned to the wurtzite structure of ZnO, shown in figure 22. Due to its structure, the (0001) plane of ZnO is polar with Zn^{2+} or O^{2-} termination. When the ZnO nucleus is created, the incoming precursor molecules tend to preferentially adsorb on the polar (0001) face to minimize the surface energy. Since the (0001) plane is the only polar plane of the crystal, the structure can only grow in [0001] direction. This explains the preference for ZnO to form a one-dimensional structure [1, 10, 57, 60, 70].

The synthesis studied in this thesis is based on the reaction of the precursors $Zn(NO_3)_2$ and HMT (hexamethylenetetramine, $(CH_2)_6N_4$) in deionized water. The growing of the rods involves the following reactions [30, 36, 57, 70]:

$$\mathrm{HMT} + 6\mathrm{H_2O} \leftrightarrow 6\mathrm{HCHO} + 4\mathrm{NH_3} \tag{19}$$

$$\mathrm{NH_3} + \mathrm{H_2O} \leftrightarrow \mathrm{NH_4^+} + \mathrm{OH^-} \tag{20}$$

$$\mathrm{Zn^{2+}} + 4\mathrm{NH_3} \leftrightarrow [\mathrm{Zn(NH_3)_4}]^{2+} \tag{21}$$

$$2\mathrm{OH^-} + \mathrm{Zn^{2+}} \leftrightarrow \mathrm{Zn(OH)_2} \tag{22}$$

$$Zn(OH)_2 \leftrightarrow ZnO{+}H_2O \tag{23}$$

$Zn(NO_3)_2$ offers Zn^{2+} and NO_3^-. HMT has several roles in the synthesis. First of all, it neutralizes all planes of the ZnO crystal apart from the (0001) plane. Consequently, the one-dimensional growth in [0001] direction according to the former discussed process can take place. Secondly, it serves as a pH buffer and hydrolyzes in water under forming HCHO and NH_3, shown in equation 19. It is of great importance that this hydrolysis occurs gradually due to the use of HMT, to avoid pH fluctuation. If the pH increases rapidly, ZnO will precipitate quickly and the growth will be inhibited. The formed NH_3 is necessary to carry on the growth of the nanorods. Primarily, it coordinates to $Zn^{2+}$and thereby stabilizes zinc salts in solution, as shown in equation 21. Moreover, it provides the basic character of the solution (equation 20) required for the formation of $Zn(OH)_2$(equation 22). Consequently, the end product ZnO is formed as shown in equation 23 [57, 60, 70].

For the growth of ZnO nanorods, a seed layer is required to favor the nucleation and orientation growth. There are several ways to prepare the seed layer, of which spin coating of quantum dots and sputtering of bulk material are often used. In this thesis radio frequency magnetron sputtering is adopted to prepare the ZnO thin film seed layer. The optimization of the ZnO nanorod surface is based on the fact that all chemical reactions are in equilibrium. Therefore, different parameters can be varied to shift the equilibrium and modify the properties of the nanorods, i.e., the length, the site density and the diameter. Growth time, seed layer thickness and precursor concentration have been reported to have influence on the morphology of ZnO nanorods [31, 57, 70].

3.4 Sample Synthesis

3.4.1 Synthesis seed layer

The PEN sheets were coated with different thicknesses of seed layer by sputtering using Sputtering Apparatus for Light Scattering Applications (SALSA, Kurt J. Lesker Company). A square of PEN was fixed in a frame and deposited on both sides with ZnO:Al 0.5% at low power (setpoint: 80 W). The different samples were made by using different recipes for the sputtering of seed layers, which are shown in Table 4.The thickness is determined by the deposition time and is measured with a Bruker Dektak stylus profiler.

Sample	Sample Thickness	Target / Nominal thickness / Sputtering time / Target to substrate distance / Pressure / Power	Sheet resistance
Sample 1	200 nm	ZnO:Al 0.5% / 200 nm / 5000s / 125mm / 1ubar / 80W	147 Ω/sqr
Sample 2	500 nm	ZnO:Al 0.5% / 500 nm / 10000s / 125mm / 1ubar / 80W	33 Ω/sqr
Sample 3	1000 nm	ZnO:Al 0.5% / 1000 nm / 20000s / 125mm / 1ubar / 80W	20 Ω/sqr
Sample 4	500 nm	ZnO:Al 1% / 500 nm / 10000s / 125mm / 1ubar / 80W	51 Ω/sqr
Sample 5	500 nm	ZnO:Al 2% / 500 nm / 10000s / 110mm / 1ubar / 80W	26 Ω/sqr

Tab. 4: Deposition parameters for different seed layers.

3.4.2 Synthesis nanorods

The low-density monodispersed nanorods were produced using a solution with a precursor of several low concentrations. A mixture of zinc acetate dehydrate (ZnAc, 219.51 g/mol, sigma-aldrich) with equal molar ratio of hexamethylenetetramine (HMT, 140 g / mol, sigma-aldrich) was solved in deionized water to obtain the precursor solution for the growth of ZnO nanorods. This was heated to 70 °C for about 10 minutes while stirred. The samples with varying seed layers were added and the solution was kept constant at 80 °C for one or three hours. After one or three hours the samples were taken out and washed. Table 5 shows the synthesized samples with the varying parameters.

Precursor Concentration	seed layer Thickness	Growth Time
0.0005M	200 nm	1 hr.
	200 nm	3 hrs.
	500 nm	1 hr.
	500 nm	3 hrs.
	1000 nm	1 hr.
	1000 nm	3 hrs
0.00025M	500 nm	1 hr.
	500 nm	3 hrs
0.0010M	500 nm	1 hr.
0.0020M	500 nm	1 hr.
0.0050M	500 nm	1 hr.
	500 nm	3 hr.

Tab. 5: Growth parameters including reactant concentration, seed layer thickness, and growth time for the synthesis of ZnO nanorods.

3.4.3 Metal contact deposition

Silver with a thickness of ~ 200 nm is deposited on the nanorod samples using an evaporation system, in our lab called the Heksenketel. With this evaporation equipment several metals, including silver, can be deposited under vacuum of ~ 1.0 e^{-6} mbar. During the deposition of Ag, the tungstond boat is heated by applying high current, and the metal is evaporated onto the substrate. In solar cells this silver layer serves as a back reflector and back contact. Therefore the light scattering in terms of diffuse reflection is important. In this regard, the optical properties of the surface can be measured by using the Perkin Elmer UV/VIS spectrometer.

3.5 Seed layer thickness

The influence of seed layer on the morphology of ZnO nanorods was studied. ZnO thin film with various thicknesses of 200 nm, 500 nm and 1000 nm were employed as the seed layers, while the reactant concentration was identical at 0.0005 M with a growth time of one hour.

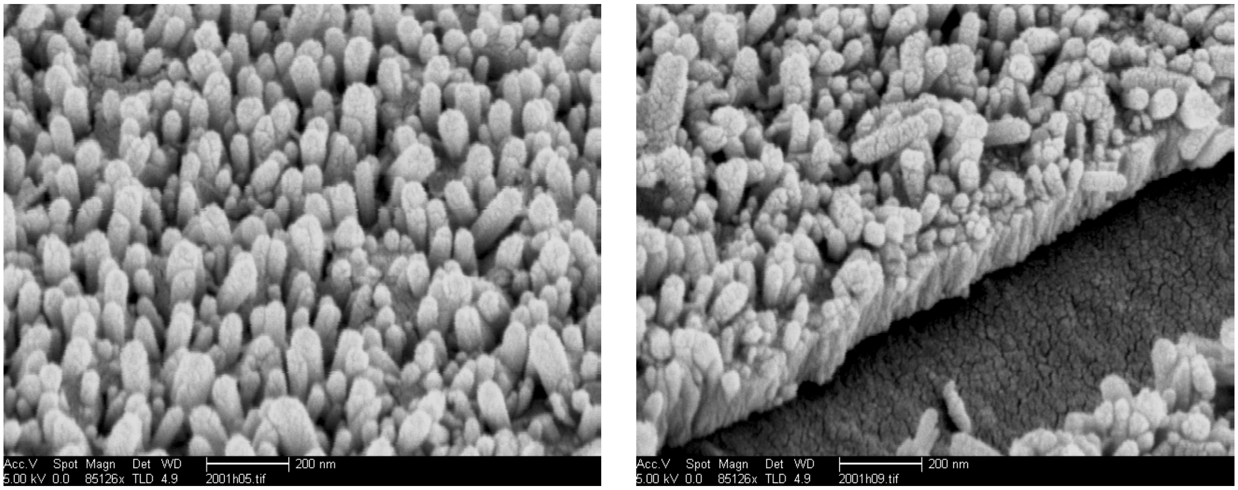

(a) Top view.

(b) Side view.

Fig. 23: SEM images shown the ZnO nanorods grown on PEN substrate precoated with a **200 nm thick ZnO:0.5wt%Al seed layer**. The reactant concentration and growth time are 0.0005 M and 1 h, respectively.

For the 200 nm seed layer thickness, the SEM images show a surface with a high rod density (figure 23). The rods grow into different direction and their diameter is ~ 50 nm. The top of the rods are round shaped.

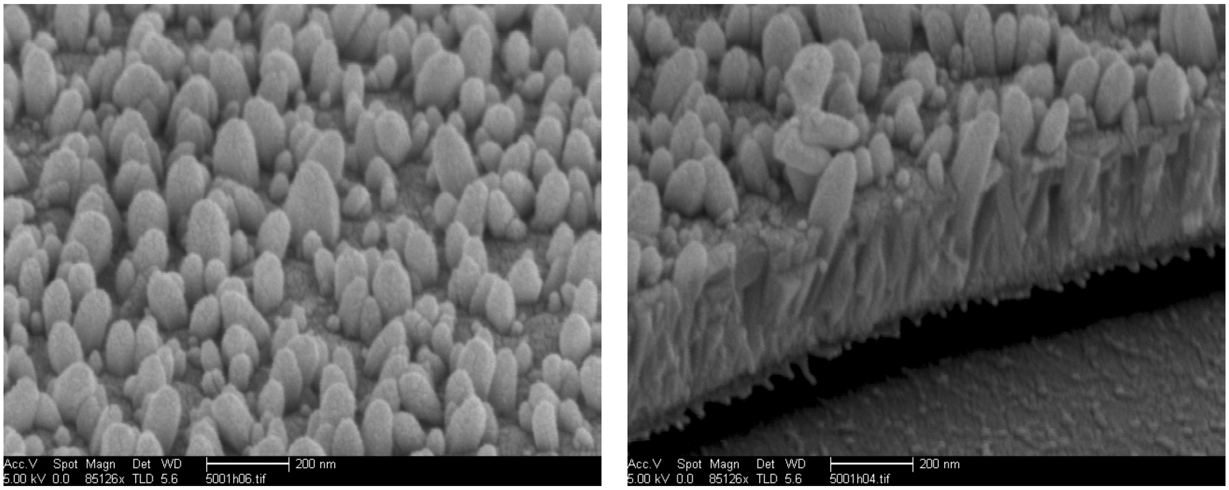

(a) Top View.

(b) Side view.

Fig. 24: SEM images shown the ZnO nanorods grown on PEN substrate precoated with a **500 nm thick ZnO:0.5wt%Al seed layer**. The reactant concentration and growth time are 0.0005 M and 1 h, respectively.

When the seed layer thickness increases to 500 nm, the diameter becomes larger and the density significantly decreased (figure 24). The SEM images show that these rods are slightly more directed into the same direction. Thereby, the rods have a smooth conic shape.

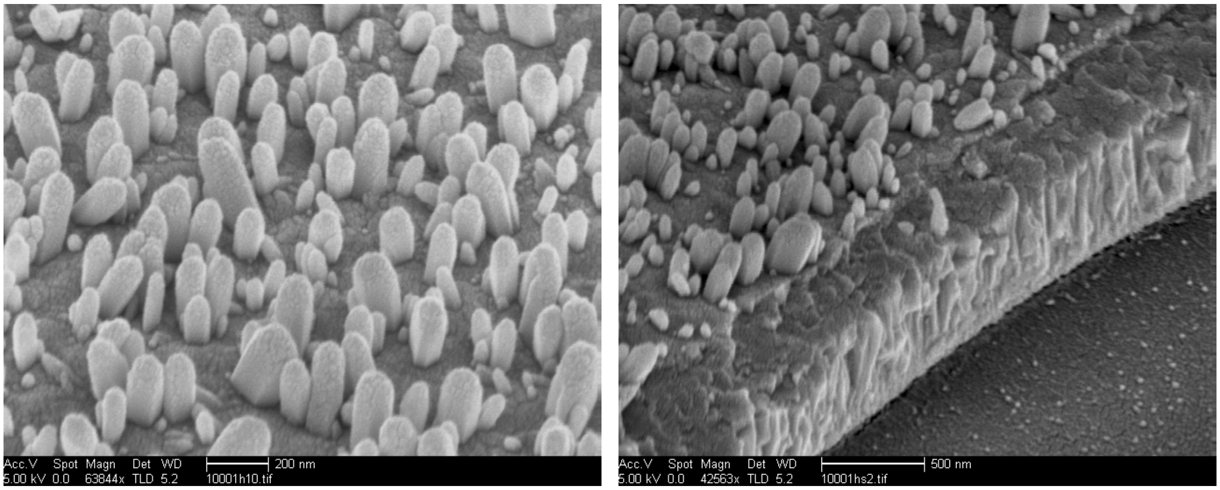

(a) Top view.

(b) Side view.

Fig. 25: SEM images shown the ZnO nanorods grown on PEN substrate precoated with a **1000 nm thick ZnO:0.5wt%Al seed layer**. The reactant concentration and growth time are 0.0005 M and 1 h, respectively.

A 1000 nm thick seed layer leads to relative thick nanorods (figure 25). The top of the rods is more round shaped than conic. The density of the rods on the surface is further decreased. Based on the above findings a simple summary given here is that the density and the diameter of ZnO nanorods are dependent on the thickness of seed layer.

3.6 Precursor solution concentration

The influence of the precursor solution is studied with a reactant concentration of 0.00025 M (0.00025 mol ZnAc mixed with equal 0.00025 mol HMT in 1 L de-ionized water), 0.0005 M, 0.001 M and 0.005 M, respectively. The morphology obtained related to certain concentration is characterized with SEM. These three samples contain a seed layer thickness of 500 nm and the rods are grown for one hour.

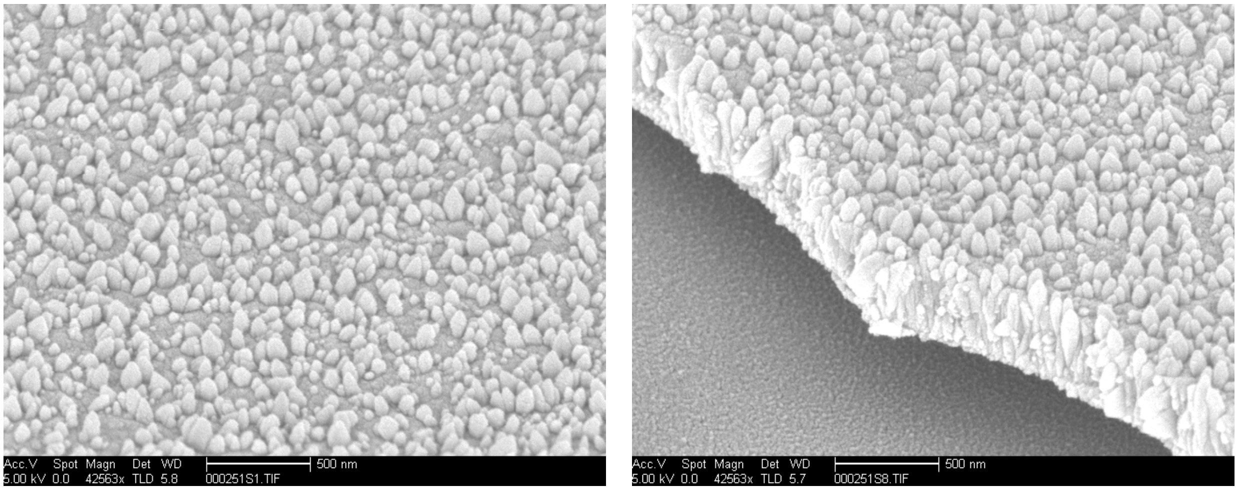

(a) Top view.

(b) Side view.

Fig. 26: SEM images shown the ZnO nanorods grown on PEN substrate precoated with a 500 nm thick ZnO:0.5wt%Al seed layer. The reactant concentration and growth time are **0.00025 M and 1 h**, respectively.

The sample with the lowest precursor concentration, 0.00025 M, shows a low density and disperse rods (figure 26). The rods are short and have a conic shape. Also, there is a small range of different lengths of the rods.

The SEM images of the 0.0005 M concentration again show conic rods (figure 24). The rod density is slightly higher, compared to the former sample. Also, it shows that a few rods are grown in a different direction. The SEM image of the side view, shows how the rods are grown. They grow from the bottom of the seed layer, and form a rod once it grows out of this layer.

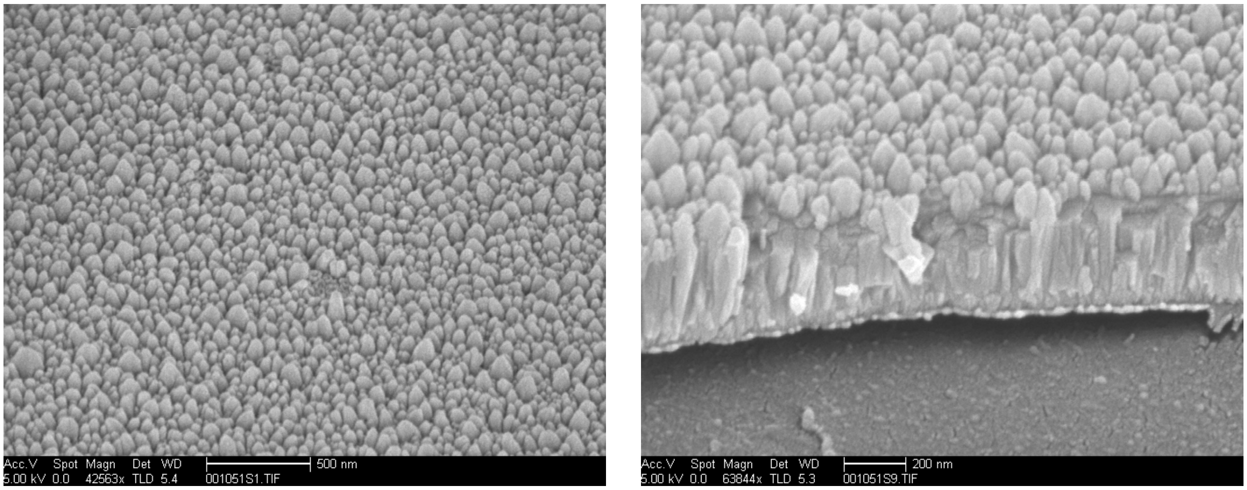

(a) Top view. (b) Side view.

Fig. 27: SEM images shown the ZnO nanorods grown on PEN substrate precoated with a 500 nm thick ZnO:0.5wt%Al seed layer. The reactant concentration and growth time are **0.0010 M and 1 h**, respectively.

For the sample using 0.001 M concentration, it can be seen in figure 27 that the rod shape of this sample is similar to the rod shape of both previously shown samples (figure 27). The density of the rods is significantly increased, and the rods show a good alignment.

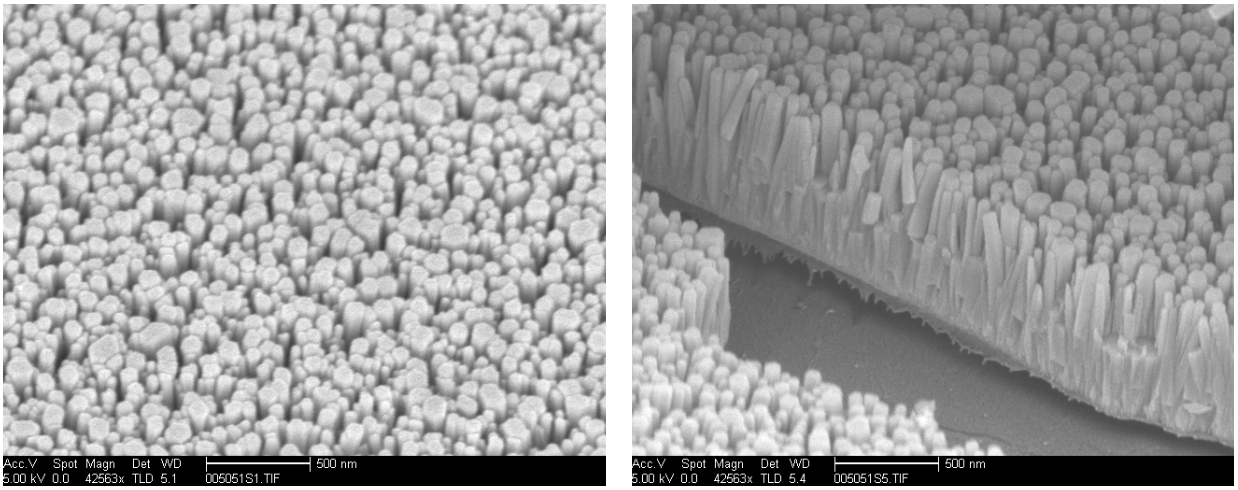

(a) Top view. (b) Side view.

Fig. 28: SEM images shown the ZnO nanorods grown on PEN substrate precoated with a 500 nm thick ZnO:0.5wt%Al seed layer. The reactant concentration and growth time are **0.0050 M and 1 h**, respectively.

When the precursor concentration is further increased to 0.005 M, the rod density is also increased (figure 28). Now, the shape of the rods is changed into wire with a flattened top. All rods are grown into roughly the same direction.

3.7 Growth time

In order to investigate the effect of growth time on the morphology of nanorods, growth time of one hour and three hours are used. All SEM images of the nanorods grown for three hours are shown (figure 29, 30, 31, 32 and 33). When these images are compared to the former shown images, which are grown for one hour, it shows that these samples contain longer nanorods. The sample with a 0.00025 M concentration of three hours forms the exception to this. The rods of this sample are not that much longer than those of the sample of one hour (figure 32), probably due to the depletion of Zn^{2+} for further growth after one hour because of the extremely low reactant concentration.

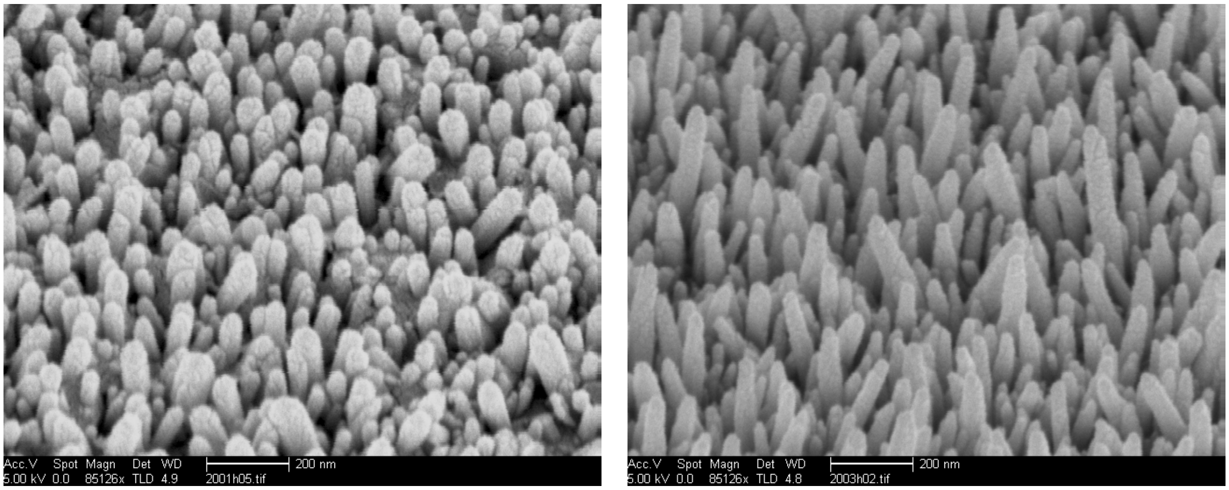

(a) 1 hour growth time.

(b) 3 hours growth time.

Fig. 29: SEM image of sample with **200 nm thick ZnO:0.5wt%Al seed layer**, a reactant concentration of **0.0005 M** and varying growth time.

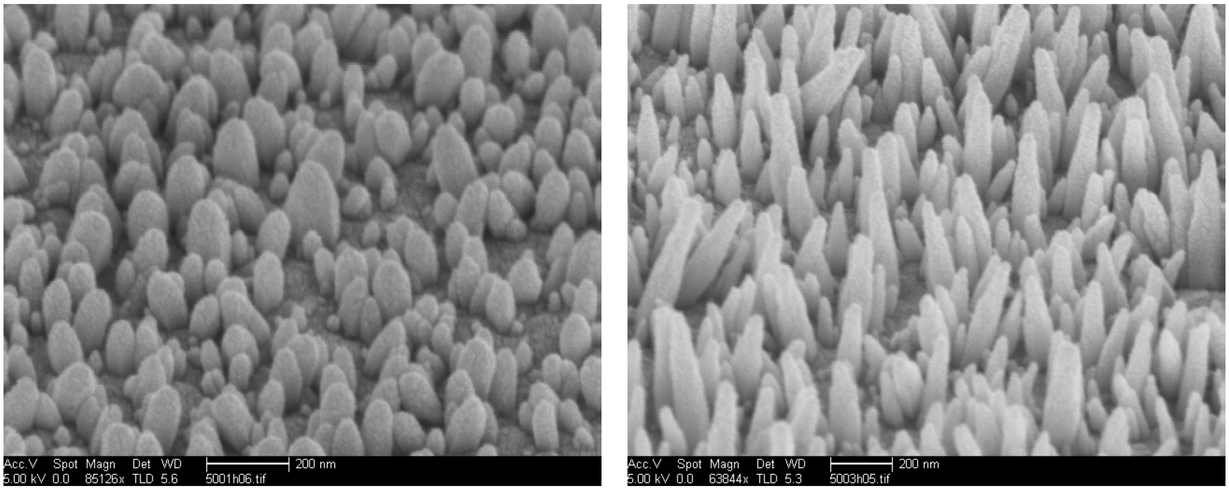

(a) 1 hour growth time.

(b) 3 hours growth time.

Fig. 30: SEM image of sample with **500 nm thick ZnO:0.5wt%Al seed layer**, a reactant concentration of **0.0005 M** and a varying growth time.

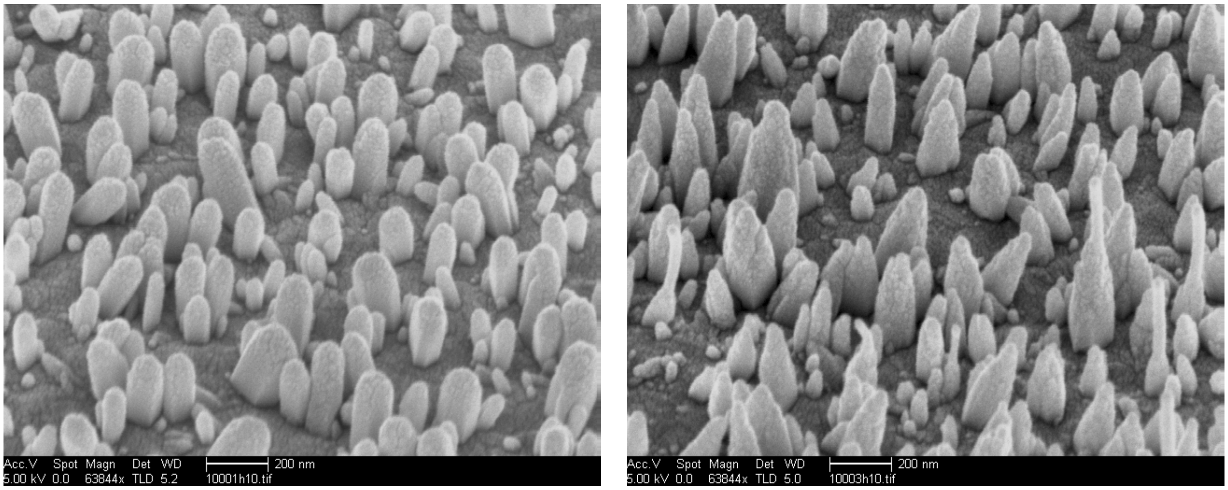

(a) (b)

Fig. 31: SEM images of sample with **1000 nm thick ZnO:0.5wt%Al seed layer**, a reactant concentration of **0.0005 M** and varying growth time.

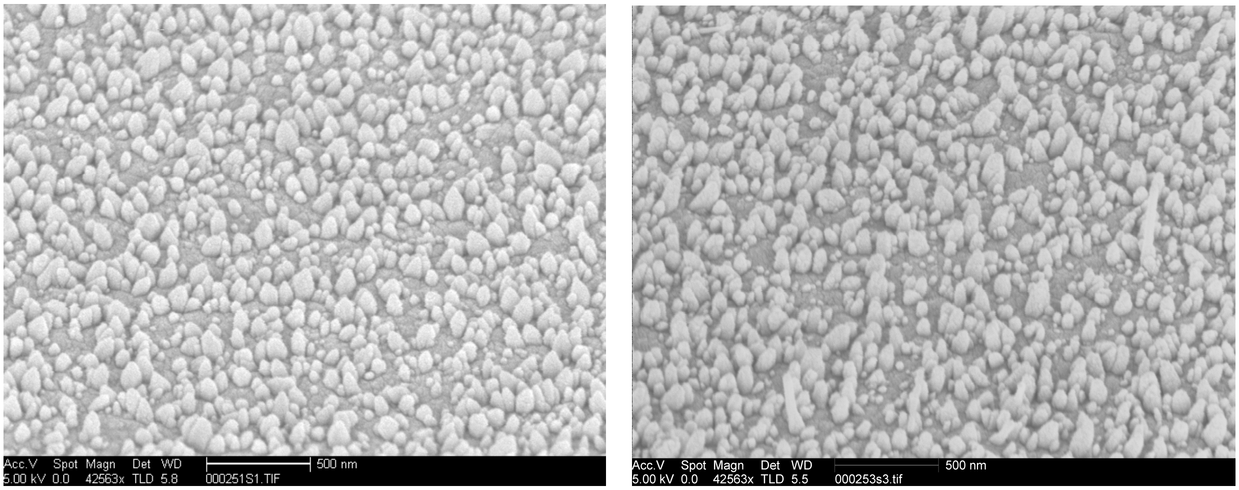

(a) 1 hour growth time. (b) 3 hours growth time.

Fig. 32: SEM image of sample with **500 nm thick ZnO:0.5wt%Al seed layer** a reactant concentration of **0.00025 M** and varying growth time.

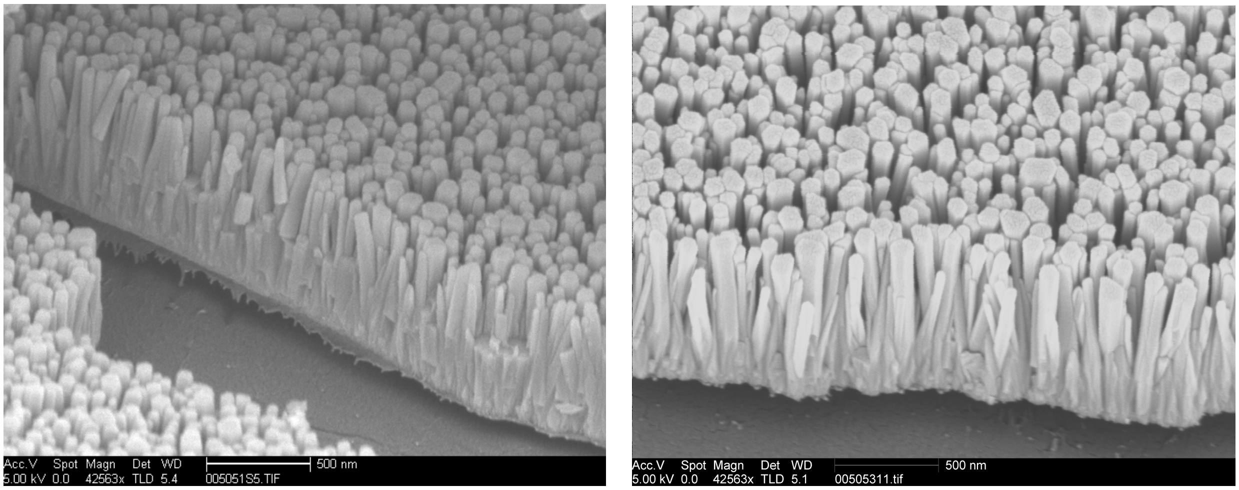

(a) 1 hour growth time.

(b) 3 hours growth time.

Fig. 33: SEM image of sample with **500 nm thick ZnO:0.5wt%Al seed layer**, a reactant concentration of **0.0050 M** and varying growth time.

3.8 The optimized growth parameters

For the morphology optimization of the nanorods as back scatters for realistic solar cells, a balance between optical and electrical properties should always be achieved. For maximum light scattering rough features are required, however for homogeneous coating of the active layers with good material quality, smooth surface is preferred. Additionally, losses related to localized surface plasmon modes can be induced due to the nanostructured metal. Based on these considerations, a suitable rod morphology is selected with an appropriate site density and aspect ratio.

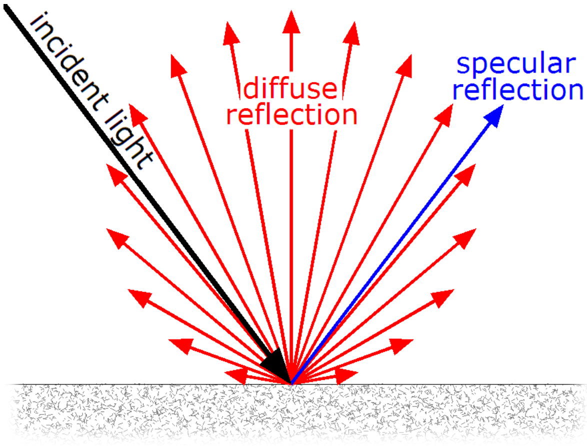

Fig. 34: Total reflection consists of two parts: diffuse reflection (red) and specular reflection (blue) [72].

The optimal light scattering of Ag coated nanorods is measured indirectly in terms of total and diffuse reflection using a Perkin Elmer spectrometer with a spherical detector, as shown in figure 34. The total reflection consists of two parts: specular and diffuse reflection. This latter is related to the light scattering. An indication of light scattering ability of a texture is the haze: the ratio of scattered transmission to the total transmission ($Haze(\lambda) = \frac{D.T.}{T.T}$). In a reflection case it is reasonable to extend this definition to the ratio of diffuse reflection to the total reflection at a certain reflective surface.

For a flat reflector on one hand it provides a high total reflection, while on the other hand its diffuse reflection is extremely low, since there is almost only specular reflection. In contrast, the nanorod-based reflector exhibits a significantly higher diffuse reflection but a lower total reflection that that for a flat surface. The reason is that the volume of Ag is significantly increased in a rod system due to the 3D geometry and hence the parasitic absorption in Ag caused by localized surface plasmon is remarkably increased.

In solar cells, ZnO nanorods coated with Ag and ZnO:2wt%Al serve as the back reflectors to scatter light into large angles hence increase optical travel path in the absorber layer. In this way the absorption is significantly enhanced. By using a Perkin Elmer spectrometer, the diffusion and total reflection are measured. Through this way, the optimal optical properties can be found. However, this optimal morphology for optical properties does not guarantee good electrical properties, since conformal coating of subsequent layers on rough features is rather difficult and very likely more defects will be introduced.

Due to the relative high deposition temperature of the metal, PEN substrates of the samples of 0.00025 M and 0.001 M deformed. Because of this deformation, reflections of these two samples could not be determined.

The total reflection of the flat reference is as expected the highest of all samples, shown in figure 35a. The curves of all nanorod samples are similar, around $\lambda = 350$ nm there is a reflection peak, and around $\lambda = 430$ nm the reflection is low and from then onwards the reflection increases gradually. Among all the nanorod samples, the sample made with a concentration of 0.0025 M and 1 hour growth on a 500 nm thick seed layer has the highest total reflection. This is consistent with the theory that the flatter surface provides highest total reflection. The sample of 0.005 M and 1 hour growth on a 500 nm thick seed layer has the lowest total reflection. The diffuse reflection of the flat sample is the lowest among all samples, which is again as expected. For all the nanorod samples, the sample with 0.0025 M concentration and 1 hour growth on a 500 nm thick seed layer is the lowest. The highest diffuse reflection is obtained for the sample of 0.0005 M and 1 hour growth on a 1000 nm thick seed layer. For both diffuse and total reflections the wavelength region 600-800 nm is the most interesting. Photons in this region can not be easily captured in a single path and a large fraction of these photons reaches the back reflector. Therefore the reflection of this part radiation is more crucial to increase light absorption in solar cells. The photons with shorter wavelength probably will be absorbed before they reach the back reflector.

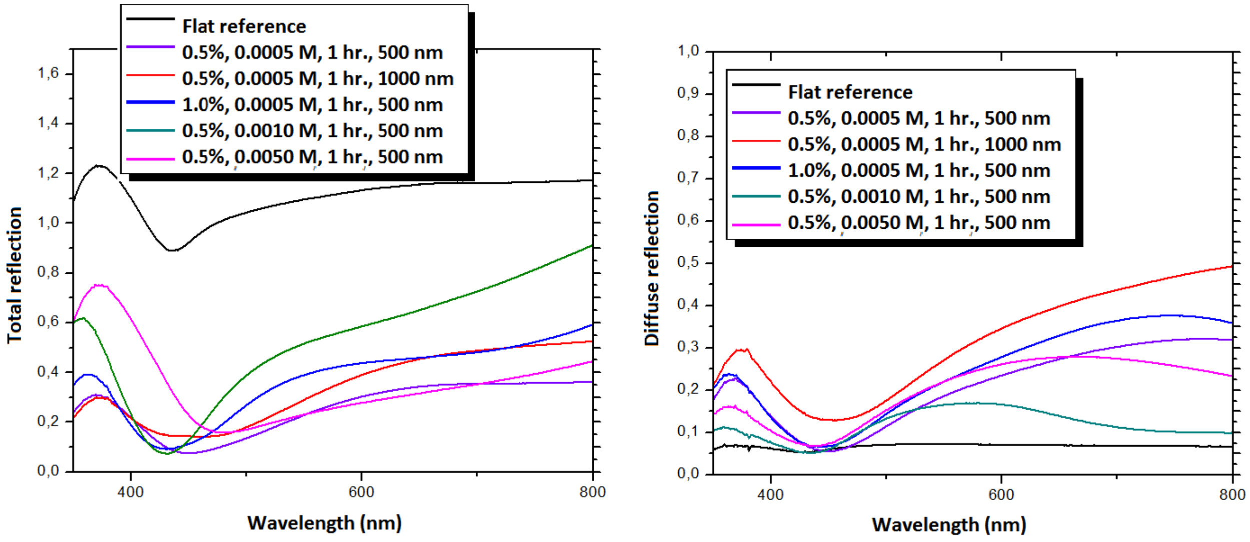

(a) Total reflection.

(b) Diffuse reflection.

Fig. 35: The reflection results of the nanorod samples coated with 200 nm thick Ag layer.

However, it is important to note that these reflection measurements are performed in air. When depositing an a-Si:H layer on the nanorod back contact, the reflection might differ due to the dielectric constant of a-Si:H. Therefore, these measurements should be repeated when the back contact is integrated in an a-Si:H solar cell. Subsequently, it can be determined whether the optimized parameters of this these are applicable for a a-Si:H thin film solar cell.

3.9 Conclusions

The morphology of the nanorods can be determined by the growth time, the seed layer thickness, and the precursor concentration. The length of the nanorods is dependent on growth time. The site density of the nanorods can be determined by the thickness of seed layer and the concentration. Thereby a high concentration assures dense rods with well alignment, where a low concentration leads to random growth of low site density of rods. As for the seed layer, a more thin layer in combination with a high precursor concentration result in well aligned rods with high site density. A thicker seed layer with a low reactant concentration generates less aligned nanorods with relatively low site density. In a certain range of time, the length of the nanorods increased with the increase in growth time. Similar results are obtained in literature [60, 57, 70].

The optimal back reflector should have both a high total reflection and a high diffuse reflection in the wavelength region of 600-800 nm. Based on this consideration, it can be concluded that the sample of 0.0005 M and 1 hour growth on a 1000 nm thick seed layer has the best trade-off between the total and the diffuse reflection. This sample has the highest diffuse reflection and a relatively high total reflection. It is also interesting to note the sample of 0.0005 M and 1 hour growth on a 500 nm thick seed layer. Its diffuse reflection is slightly lower than the one on a thick 1000 nm seed layer and the total reflection is similar, but it should be pointed out that the seed layer in this sample is half the thickness compared to that of the 1000 nm in the other sample. Thus, the material consumption is significantly decreased while not at obvious expense of optical properties.

4 Modeling of nanorod solar cells

4.1 Abstract

In this chapter the FDTD simulations on the nanorod system will be discussed. An a-Si:H solar cell built on ZnO nanorods is used as the model for simulation. By varying cell parameters such as the absorber layer thickness, the morphology of ZnO nanorods, and the different metallic back reflectors, the absorption of the nanorod system is investigated and optimized. After a short introduction, the nanorod structure of the solar cell will be explained , following the FDTD settings and the results. Finally, an optimization of this system is performed by varying the length of the rods, the distance between the rods, and the i-layer thickness of the solar cell. This chapter is completed with a discussion and conclusion.

4.2 Introduction of the nanorod thin film solar cells

In a previous work of our group a nanorod-based three dimensional (nano-3D) solar cell concept is proposed [26, 27]. More recently the Nano-3D cell has been optimized for a significantly enhanced performance by Kuang and the results will be published elsewhere soon. Figure 36 shows a SEM image of the cross section of the optimized nano-3D cell with a 200 nm thick a-Si:H absorber layer.

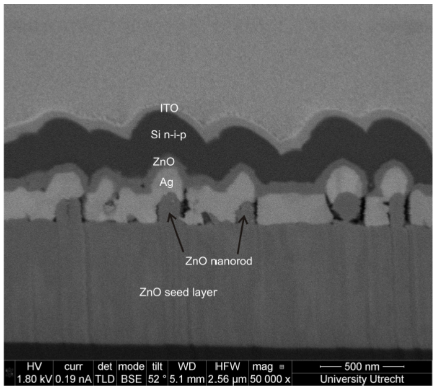

Fig. 36: SEM image of the cross section of a nanorod-based solar cell.

In order to get an insight on the absorption of this solar cell FDTD simulations are performed and parameters are optimized. These simulations can explain the absorption spectrum of the a-Si:H layer. In a flat solar cell photons can be described by Lambert-Beer Law by approximation and absorption due to reflected photons, as discussed in paragraph 2.4. When adding a nanostructure, additional absorption peaks appear, which can be caused by resonances.

4.3 The design of the nanorod solar cells

For the simulations the structure of the solar cell is simplified to a surface of periodically distributed rods with a spacing of 400 nm. The coating of the rods is assumed to be conformal. The length of ZnO nanorod is set to 300 nm and the diameter is set to 100 nm. They are coated with a 200 nm thick layer of silver. This is used as the back contact of the cell. Then an aluminum doped zinc oxide (ZnO:2wt%Al) layer is added. This layer is needed to prevent diffusion of silver into the a-Si:H layer and to avoid possible absorption in the Ag layer. The thickness of this layer is chosen to be 80 nm, because this seems to cause optimal back reflection. Next, the ZnO is covered by an a-Si:H n-i-p junction with thicknesses of 30 nm, 200 nm and 15 nm, respectively. The top layer is a 80 nm thick indium tin oxide (ITO), used as a transparent conducting oxide (TCO) layer. Figure 37 shows a schematic fraction of the cross section of the simulated nanorod solar cell.

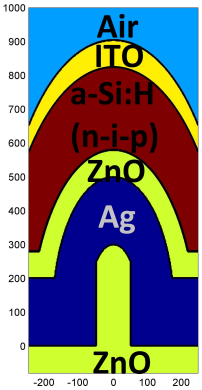

Fig. 37: The cross section of the simulated nanorod solar cell. The nanorod has a length of 300 nm and a diameter of 100 nm. The solar cell contains an a-Si:H n-i-p junction of 30 nm, 200 nm and 15 nm thick, respectively.

In order to investigate the effect of individual layer of Ag, ZnO and a-Si:H on the optical performance of solar cells, cells with different shape and thickness for Ag, ZnO and a-Si:H are simulated. These samples are divided into three different series of structures. The first series , as shown in figure 38, consists of four samples with similar a-Si:H i-layer thickness, labeled as the original Ag nanorod sample. In figure 39b and 38b a structure without ZnO layer and with a 20 nm thick ZnO layer are shown. A 20 nm ZnO thickness is chosen because it is thin enough to show a possible plasmonic effect. Additionally, two structures with or without a flat Ag layer are shown in figure 38c and 38d. From the results of these samples, the effect of the Ag back contact and the ZnO layer on the optical properties of the solar cell can be derived.

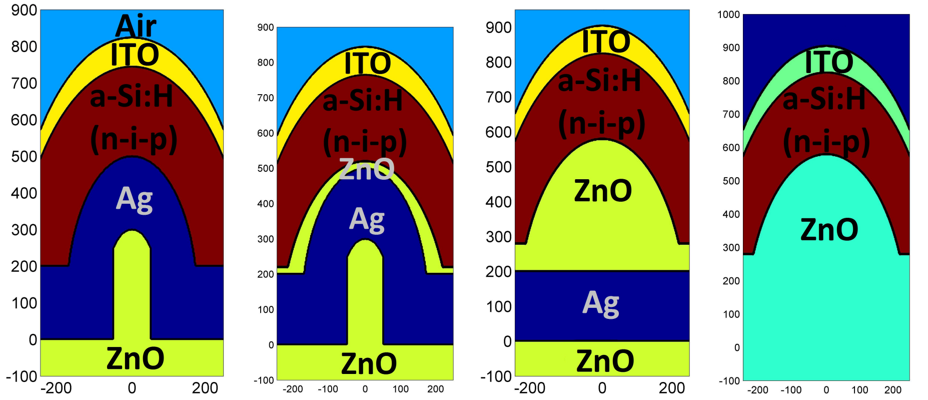

(a) Sample without ZnO. (b) Sample with 20 nm ZnO layer. (c) Sample with flat Ag. (d) Sample without Ag.

Fig. 38: A series of cross sections of structure 1, thin a-Si:H layer.

The flat substrate based structure series contain samples with the a-Si:H i-layer thick, as shown in figure 39, without a rod in the center with or without the flat Ag layer. The results of these samples are used to find out the influence of the rod and the contribution of the a-Si:H layer shape. Due to the thick a-Si:H layer, the absorption of this series increases significantly. However, this structure might be not favored in realistic cell due to the remarkably increased material volume which inevitably introduces more defects and increases the transport length of minority carrier. In addition, samples with different metals are simulated. In this case the original structure is maintained, only the Ag is replaced by aluminum (Al), gold (Au), and copper (Cu). The different metals contain different dielectric properties and different plasmon resonance modes. Based on these simulations, the effect of back reflector materials on the optical performance of the cells is investigated . The absorption spectra of all samples are compared to the original Ag nanorod solar cell. Additionally, the absorption cross sections are also investigated via simulations.

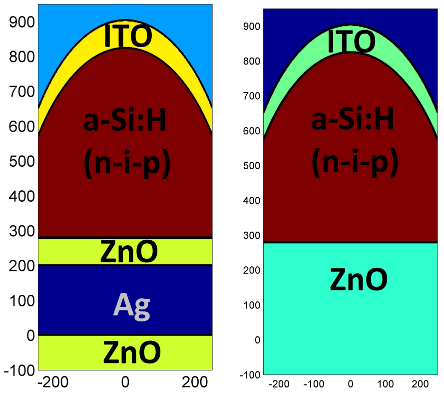

(a) Sample with flat ZnO and Ag.
(b) Sample without Ag and flat ZnO.

Fig. 39: Schematic cross sections series of structure 2, thick a-Si:H layer.

After discussing the origin of the absorption enhancement, the design of the solar cell will be optimized. Three parameters are varied to find the optimum, i.e., the length of the rods, the distance between the rods and the thickness of the a-Si:H i-layer. The optimal solar cell will be defined according to the calculated current density. However, it should be pointed out that the calculated current density is not equal to the real current density, because not all features are taken into account. In the simulations the assumption is made that all carriers generated by photons are collected by the electrodes. However, in a realistic case carrier recombination due to defects causes a non-negligible reduction on carrier collection efficiency. Nevertheless, the calculated current density can give an indication on which structure has the highest potential for enhancing absorption.

4.4 Simulated light absorption of nano-3D solar cells

4.4.1 FDTD settings

The simulations are run in FDTD, which solves the Maxwell equations, as discussed in Chapter 2. The settings are used to make the simulated results comparable with the experimental results. First of all it is important to keep in mind that all performed simulations in this thesis are two dimensional (2D). Therefore, the results can be deviate from the real results of the three dimensional system. An other important setting for the simulations is the material properties. These should be similar to the properties of the materials used for the experimental results. In order to see if the properties are correct, it is necessary to look at the fit plots of the materials. In these simulations standard silver of Palik (0-2 μm) is chosen, since these properties correspond to the silver used in the experiment. The properties of ZnO, ITO and a-Si:H are measured from samples and added to the material database. The material optical indices including a fit needed for FDTD, are shown in figure 40. For the trade-off between the duration of the simulation and the accuracy, a convergence test of the mesh size is needed. Derived from this convergence test, a mesh size of 2 nm is adopted. The frequency points are set at 100 points, to limit the simulation time [33].

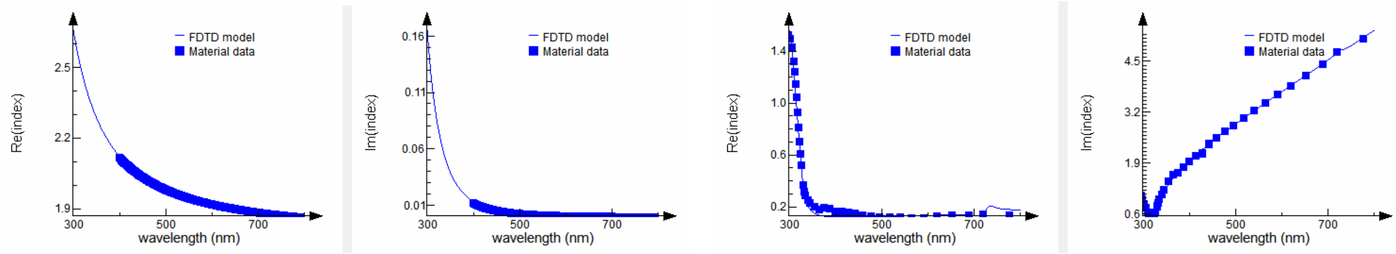

(a) Real and Imaginary values of ZnO.

(b) Real and Imaginary values of Ag.

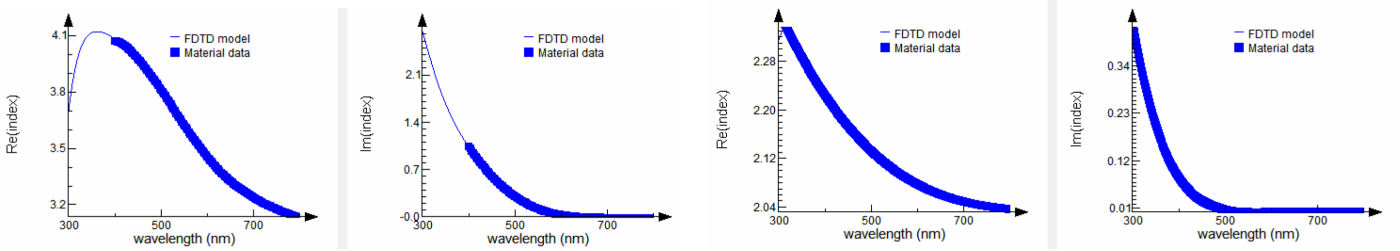

(c) Real and Imaginary values of a-Si:H.

(d) Real and Imaginary values of ITO.

Fig. 40: Optical properties of the materials in FDTD.

The quantum efficiency (QE) describes the calculated absorption of the simulated solar cell, when only taking the optical features into account. It is calculated by measuring the photon absorption in the a-Si:H i-layer, according to the formula [33]:

$$QE(\lambda) = \frac{P_{abs}(\lambda)}{P_{in}(\lambda)} \tag{24}$$

$P_{in}(\lambda)$ is the power of the incoming photons, $P_{abs}(\lambda)$ is the power of the absorbed photons at wavelength λ. In general the quantum efficiency is referred to as external quantum efficiency (EQE), though in this paper it will be referred to as QE. It is necessary to keep in mind that every absorbed photon contributes to the current in the simulation. Subsequently, in FDTD the current density is calculated as following [33]:

$$J_{sc} = e \int \frac{\lambda}{hc} QE(\lambda) I_{\mathrm{AM1.5}}(\lambda) \mathrm{d}\lambda \tag{25}$$

where e, h, c, $I_{\mathrm{AM1.5}}$are electron charge, Plank's constant, the speed of light and AM 1.5 solar spectrum at a wavelength λ, respectively.

In this thesis, the results of the simulations are exported to Matlab, where all further calculations are done by a developed script. The simulation yields the absorption per Yee cell [75]. The absorption cross sections are plotted directly from these FDTD results. To calculate the absorption in the solar cell, first the absorption of all Yee cells are summated. The result is integrated over the volume of each Yee cell, to obtain the absorption. The absorption can be calculated per material layer. Afterwards, the amount of photons in the light spectrum of interest is multiplied by the AM1.5 solar spectrum. The result of the a-Si:H i-layer is integrated to obtain the current density.

4.4.2 FDTD results

In order to get an insight on the absorption that takes place in the Ag nanorod solar cell, it is important to determine the origin of the absorption spectrum. The reflection and absorption of the photons can be analyzed according to the thin film interference theory. This theory states that an incoming photon can be either reflected, absorbed or transmitted by a layer in a solar cell. The reflected photons from top interface and from bottom interface together form an interference pattern which is dependent on the reflection, the transmission, the absorption coefficient of the layer and the angle of incidence, as shown in figure 41. Due to the nanorods, this interference pattern differs significantly from a flat case. The first effect of the nanostructure is that it changes the reflection and transmission of the top layer. Additionally, the optical path in the absorber layer is extended, and therefore the direct absorption of photons could be increased. In all cases, the non-absorbed photons can be reflected or transmitted by the ZnO/Ag back reflector [71]. Since these structures are presumably too big it is assumed that plasmonic effects will not occur in the Ag layer. However, if inexplicable results are obtained, this might still indicate a possible presence of a plasmonic effect.

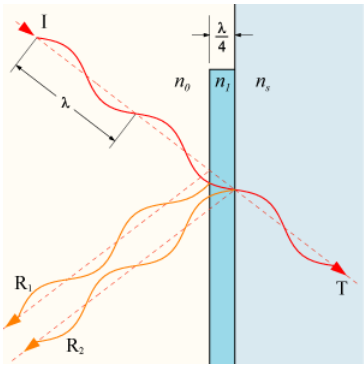

Fig. 41: Light incident transmission and reflection on different layers [71].

Absorption of the original Ag nanorod solar cell. In figure 42 the absorption spectra of both the flat and the nanostructured solar cells are shown. At short wavelength the absorption in the a-Si:H i-layer is expected to be high, due to its refractive index. On the contrary, low absorption is obtained in the a-Si:H i-layer because of the absorption in the ITO layer at short wavelength, derived from the optical properties of ITO shown in figure 40. At $\lambda = 550$ nm, another maximum is obtained. These two maxima are probably obtained due to the same interference effect akin the absorption maxima of the thin film solar cell studied in section 2.4. The nanostructured solar cell also shows the interference effects, but are shifted as a consequence of the rod shaped surface. Additionally, more peaks are presented in the absorption spectrum of the nanostructured cell. These peaks might originate from the rod-like geometry, but this assumption is not confirmed yet. The exact peak positions of the Ag nanorod sample are listed in table 6.

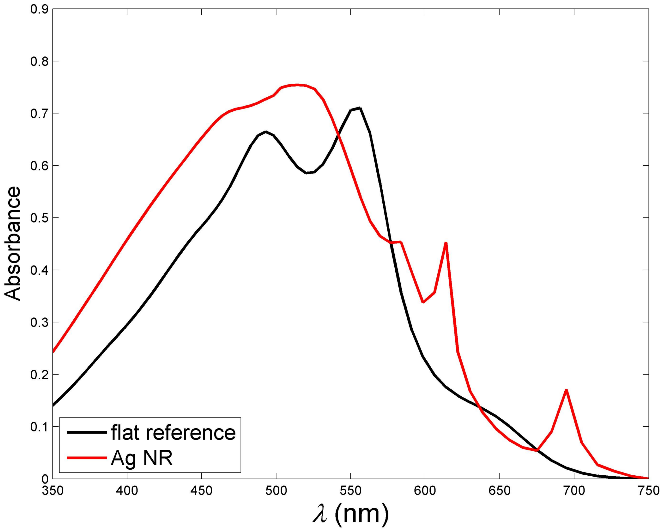

Fig. 42: The absorption spectra of the original Ag nanorod solar cell together with the flat reference.

Sample	λ_{peak} (nm)					
Ag NR	464	520	584	614	695	
No ZnO	451	503	598	647		
ZnO = 20 nm		503		630	685	
Flat Ag		532		614	685	705
No Ag		514	606	675	695	
Flat ZnO		538		614	656	705
Flat ZnO, no Ag	520	550	577	606	656	
Flat reference	493	556				

Tab. 6: Absorption peaks in a-Si:H i-layer of structure series 1 and 2 and the flat reference solar cell.

Comparison of light absorption between the original Ag nanorod solar cell and the other structures. The absorption spectra of series 1 and series 2 are shown in figure 43. In order to avoid the possible confusion on the large absorption of series 2 (which originates from the thick a-Si:H i-layer), the plots of the absorption for series 1 with a nanorod in the center and for series 2, where the a-Si:H nanorod is directly grown on a flat substrate, are divided into two graphs. The theoretical current densities obtained from the a-Si:H i-layer of the samples are listed in the table in figure 43. The absorption for all the structures (except for the flat reference) in the wavelength range of 350-450 nm are very similar. The reason is that a large fraction of this part of radiation is absorbed at ITO, p-layer and top region of i-layer before reaching the back nanostructures due to the high absorption coefficient of a-Si:H at short wavelength. Therefore, the different back reflectors do not influence the absorption at short wavelength. However, the flat reference demonstrates a significantly worse blue response. This can be explained by the naturally formed texture at the top surface due to the conformal growth of all applied layers on nanorods. The textured front surface reduces the reflection loss at top surface, demonstrating an anti-reflection effect. At longer wavelength, the Ag nanorod solar cell and the series of structure 1 and 2 show two correlating peaks, as shown in table 6. The flat Ag sample and the flat ZnO sample both contain the peak at $\lambda = 614$ nm. The sample without Ag shows the peak at $\lambda = 695$ nm. The absorption cross sections at these peak wavelengths will be studied later.

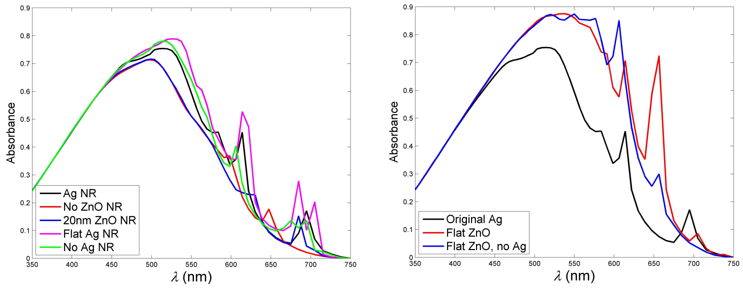

(a) Absorption structure series 1. (b) Absorption structure series 2.

	Ag sample	No ZnO	ZnO = 20 nm	Flat Ag	No Ag	Flat reference
I_{sc} (mA/cm^2)	11.23	10.23	10.28	12.20	11.51	9.23

Fig. 43: Absorption in a-Si:H i-layer and the obtained current density of the samples.

Samples with different metal back contact. The absorption of the Ag samples is also compared to samples with different metals, i.e.: Al, Au and Cu, as shown in figure 44. Again, the curves show increasing absorption at short wavelength due to the absorption in the ITO layer, this same effect is shown Chapter 2.4 in the thin film solar cell. Around $\lambda = 464$ nm and $\lambda = 520$ nm the absorption curves show two local optima. At these optima the absorption of the Al and Ag samples is significantly higher than that of the Au and Cu samples. At longer wavelength different peaks appear in the different absorption spectra. The exact wavelengths of the peaks are listed in table 7. All samples have the peak at $\lambda = 695$ nm. It is remarkable that the sample without Ag also contains this peak. If these peaks have the same origin, this could imply that this peak is caused by the ZnO back reflector. In order to confirm whether these peaks have the same origin, their absorption cross sections will be examined. The peak at $\lambda = 614$ nm is present in the Ag, Au and Cu samples. It is interesting to note that these peaks also appear in the samples with flat Ag and flat ZnO. Therefore, this might be caused by the morphology of the a-Si:h i-layer. The Au sample additionally contains a peak at $\lambda = 584$ nm.

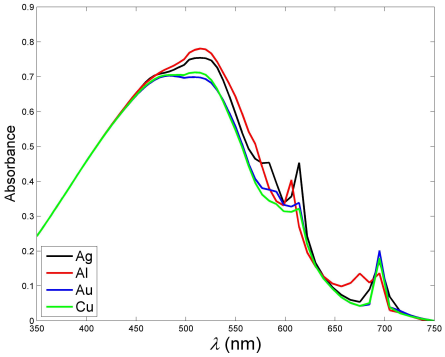

	Al sample	Au sample	Cu sample
I_{sc} (mA/cm^2)	11,37	10,58	10,48

Fig. 44: Absorption in a-Si:H i-layer of different nanorod metal samples and the obtained current densities of the samples.

Sample	λ_{peak}(nm)					
Al	464	526	606	675	695	716
Au	473	526	584	614	695	716
Cu	473	526		614	695	716

Tab. 7: Absorption peaks in a-Si:H i-layer of the samples with different metals.

Absorption cross section of the Ag nanorod solar cell. The absorption cross sections at the discussed absorption peaks of the Ag nanorod sample are shown in figure 45. Additionally the absorption cross sections of three local absorption minima at $\lambda = 606$ nm, $\lambda = 666$ nm and $\lambda = 705$ nm are shown, to study the absorption patterns off-resonance. The absorption cross section at $\lambda = 464$ nm differ from the flat reference, shown in figure 17b, probably caused by the shape of the top texture of the nanorod solar cell. Due to this naturally evolved structure, the blue response is improved. The absorption is localized at the top of the nanorod, and tapers towards the top of the metal rod. The absorption cross section at $\lambda = 520$ nm shows a similar shape. Though, a more complex absorption pattern is shown and the absorption in the metal layer is increased due to the larger penetration depth of photon in this wavelength. More photons interact with the back reflector and proportionately more of them are absorbed by structured metal back contact due to the localized surface plasmon mode. The vertical interference pattern is interrupted by absorption maxima and minima in horizontal direction. This pattern can be derived from internal reflection of the ZnO and the Ag layer. When looking at longer wavelengths, more complex absorption patterns dominate. At $\lambda = 614$ nm the absorption maximum starts to localize at the top and the two sides of the nanorod. This effect is even stronger in the absorption cross section at $\lambda = 685$ nm.

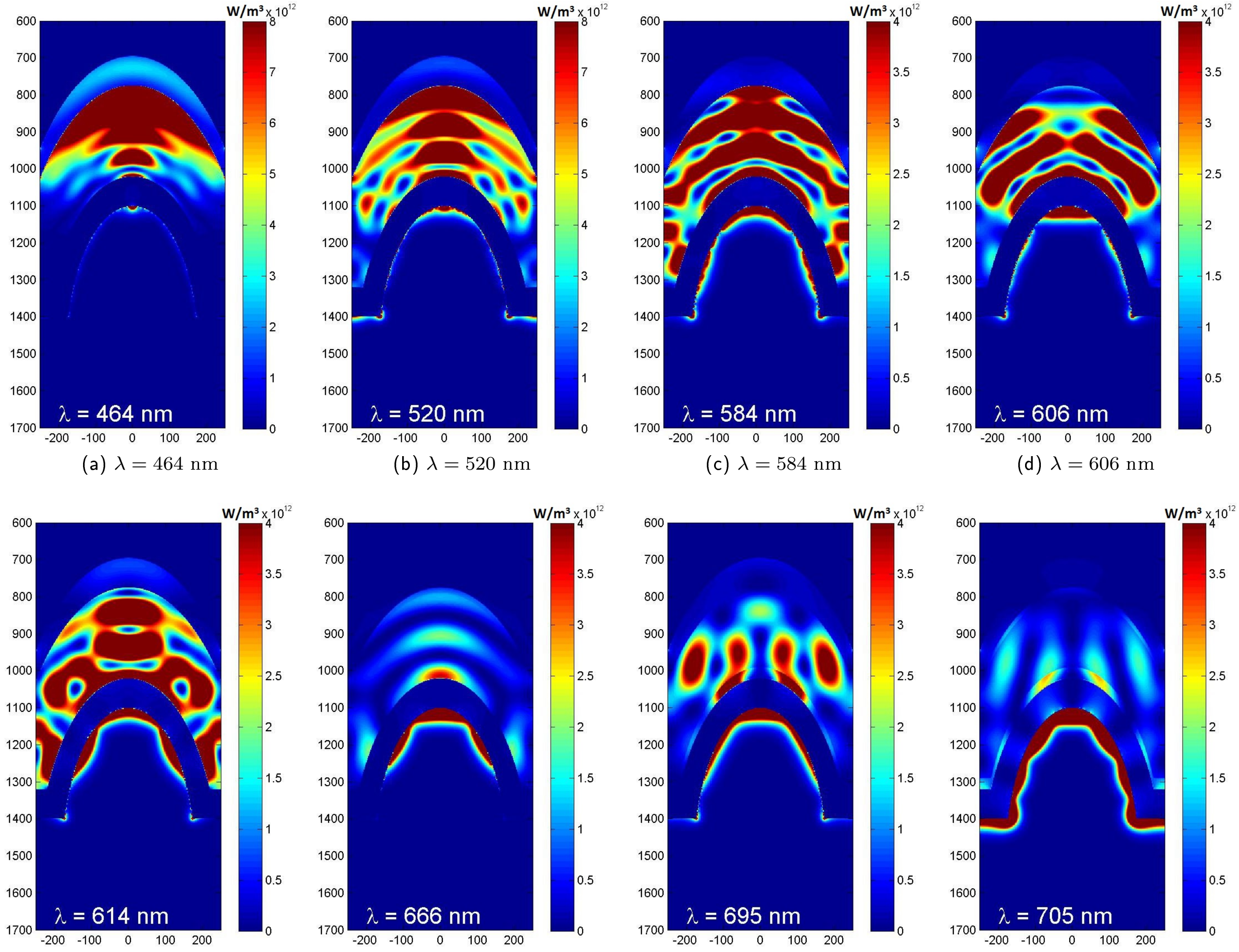

(a) $\lambda = 464$ nm (b) $\lambda = 520$ nm (c) $\lambda = 584$ nm (d) $\lambda = 606$ nm

(e) $\lambda = 614$ nm (f) $\lambda = 666$ nm (g) $\lambda = 685$ nm (h) $\lambda = 705$ nm

Fig. 45: The absorption cross sections of the original silver nanorod sample.

The absorption cross sections at the wavelengths of the local minima are at $\lambda = 606$ nm, $\lambda = 666$ nm and $\lambda = 705$ nm. Low absorption maxima are observed in the a-Si:H i-layer, due to weak constructive interference which occurs off-resonance.

Comparison of the absorption cross sections for different samples. In the above paragraph the peaks of the Ag nanorod solar cell are discussed that also appear at the absorption spectra of the other samples, as shown in figure 43 and figure 44. The absorption cross sections of these peaks are shown in figure 46a, 47 and 48, and are studied to determine the origin of the peaks. The peak at $\lambda = 584$ nm of the Au nanorod sample is shown in figure 46a. The absorption patterns in a-Si:H i-layer in Au nanorod sample are very similar to that in the Ag sample at this wavelength (figure 45c) with only small differences. The absorption in both metal layers differs. This small difference very likely is related to the absorption in metal layers which differs from each other. The absorption difference in metal layers can influence the absorption in the a-Si:H layer. Despite of the small deviation, it can concluded that the origin of the peak at $\lambda = 584$ nm both in Ag and Au samples is the same. Therefore, this peak of the Ag nanorod solar cell is hardly dependent of the metal and thus most likely is caused mainly by the morphology, e.g., an interference effect.

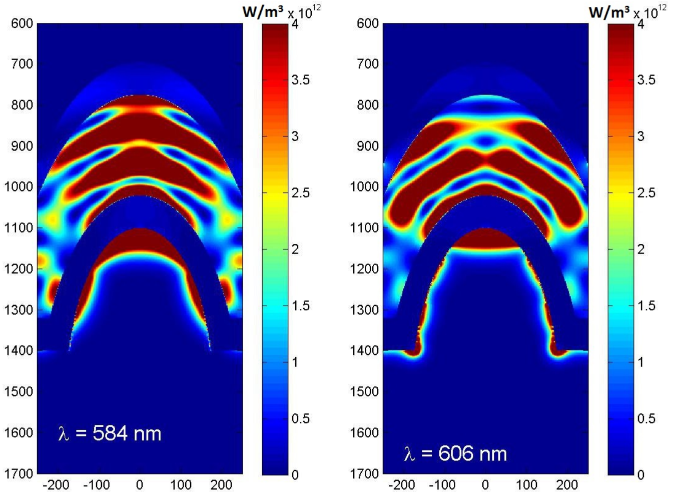

(a) $\lambda = 584$ nm.

(b) $\lambda = 606$ nm.

Fig. 46: Au nanorod sample.

As discussed above, the peak at $\lambda = 614$ nm appears in cells both with and without a metal rod, as shown in figures 43 and 44. The absorption cross section of the Au nanorod sample, shown in figure 47a, is strongly consistent with the cross section of the Ag nanorod sample (figure 45e). The same applies for the cross section of the Cu nanorod sample at $\lambda = 614$ nm, as shown in figure 47b. In contrast, the sample with flat Ag strongly deviates from the former two cross sections, as shown in figure 47d. The absorption patterns is caused by interference in the vertical direction, due to the flat Ag back reflector. The absorption of this solar cell is significantly enhanced as shown in figure 43. The cross section of the flat ZnO sample has a complex interference pattern, due to the increased a-Si:H layer thickness (figure 47d). The absorption pattern differs significantly from the Ag nanorod sample (figure 45e). On the other hand, it shows resemblance with the flat Ag sample. Due to the changed geometry of the a-Si:H layer, it is difficult to compare this cross section directly with the cross section of the Ag nanorod sample. Concluding, the peak at $\lambda = 614$ nm is attribute to the structure and almost independent on the metals.

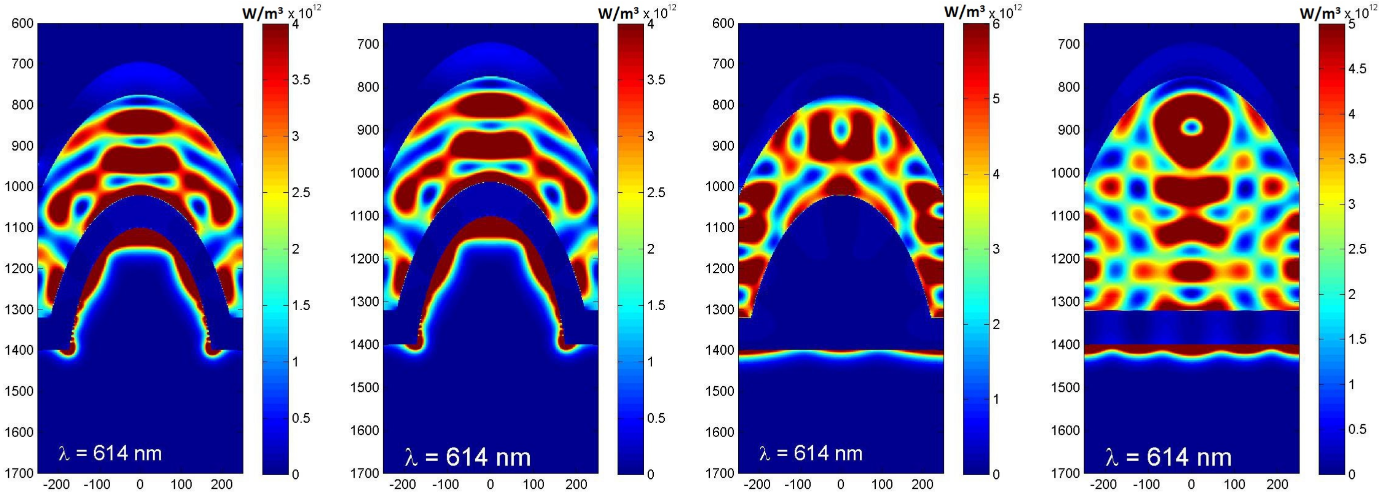

(a) Au sample.

(b) Cu sample.

(c) Flat Ag sample.

(d) Flat Zno sample.

Fig. 47: Absorption cross sections at $\lambda = 614$ nm of different nanorod samples.

The peak at $\lambda = 695$ nm, shown in figures 43 and 44, appears in different metal samples and in the sample without metal. Therefore, this peak originates very likely from something else rather than the metal. Though as shown before, it is possible that two peaks appear at the same wavelength, but are caused by a different effect. Therefore, it is important to take a look at their cross sections. The contribution of the ZnO layer can be determined by comparing the samples with and without metal. Also the contribution of the metals can be derived from this comparison. The interference patterns of all five samples are similar, shown in figure 47. Consequently, the origin of all peaks is the same. Also, the absorption pattern of the sample without metal shows that a large fraction of the photons is reflected by the ZnO layer (figure 48a). From the absorption spectrum it seems that more than half of the reflected photons is caused by this layer, derived from figure 43. It is remarkable that the absorption cross sections of the metal samples, shown in figure 45g, 48b and 48c, have the same interference pattern as the sample without the metal back reflector. Due to the metal back reflectors, the absorption maxima are enhanced. In addition, the Au nanorod back reflector appears to have the highest reflection.

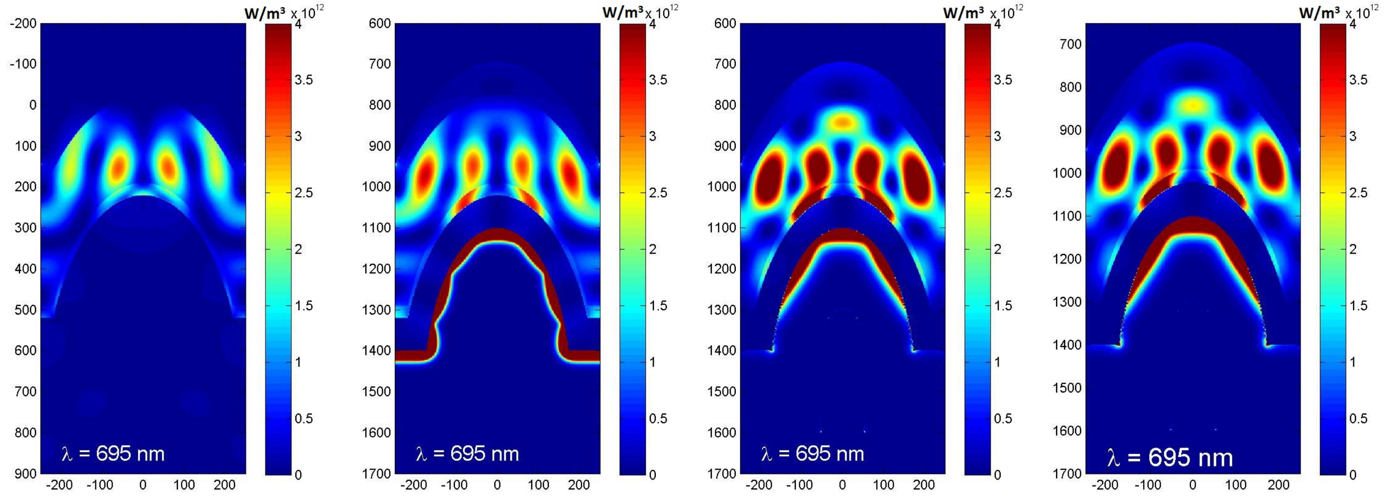

(a) No Ag sample. (b) Al sample. (c) Au sample. (d) Cu sample.

Fig. 48: The absorption cross sections of the absorption peak at $\lambda = 695$ nm of different nanorod samples.

4.5 Optimization of the cell design

In the FDTD simulations three parameters of the ZnO nanorod arrays are varied to find the optimal parameters for solar cell. These investigated parameters include the length of the rods (l), the distance between the rods (d), and the i-layer thickness (t). It is important to be aware that not all simulated are applicable to realistic device, because in practice the coating should be conformal. In addition one should keep in mind that the electrical properties are not taken into account in the simulations, while in real device it largely determines the cell performance, and that the simulations are performed in 2D.

4.5.1 The effect of the length of the nanorods

The length of the nanorods is varied from 100 nm up to 1000 nm with a step of 100 nm for 100-400 nm and onwards a step of 300 nm for 400-1000 nm. The distance between the rods for these samples is set on 400 nm, and the a-Si:H i-layer is set on 200 nm, because these two parameters correspond to an experimental solar cell previously made. Due to the different lengths of the nanorods, the interference of the reflected photons in the a-Si:H layer changes. Therefore, the wavelength of the absorption peaks can shift, shown in figure 49. Mainly, the absorption peaks of the 100 nm and the 200 nm samples appear to differ from the other samples. The absorption peaks of the 300 nm till the 1000 nm samples are similar, with only small differences in absorption intensity. The optimal short-circuit current density (I_{sc}) is at a nanorod height of 300 nm, as shown in figure 50.

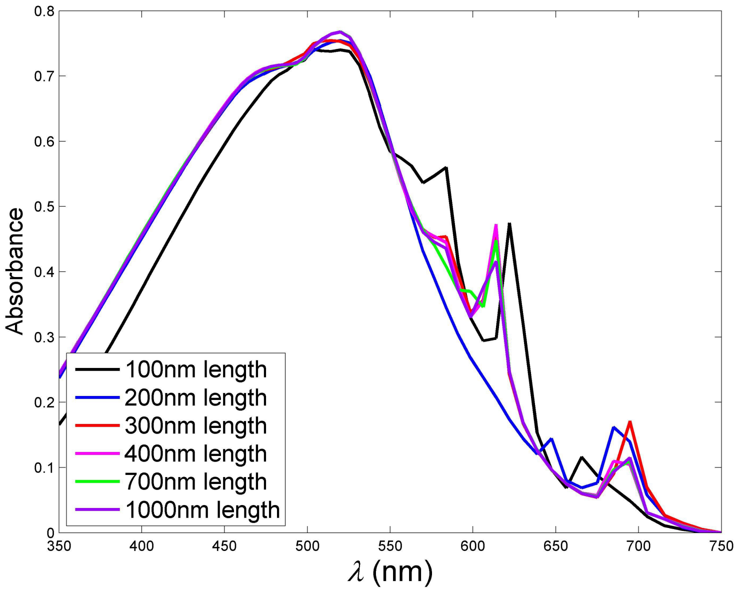

Fig. 49: Absorbance of different samples with a distance of 400 nm, a i-layer thickness of 200 nm and a varying length of the rods.

Figure 50 shows a heighest absorption in the nanorod samples with a rod length of 300 nm. The lowest current density is obtained at a rod length of 200 nm. As shown in figure 50, the current density as a function of rod length is neither parabolic nor linear. Therefore, it is difficult to find a direct relation between the current density and the rod length. Nevertheless, on one hand the rod length should be high enough to provide significant roughness of the surface, appropriate optical path length and optimal internal reflection back into the a-Si:H i-layer of the solar cell. On the other hand, too long nanorods will decrease the absorption. While the pitch of the nanorods is constant, the radius of the longer rods will increase. Consequently, the longer rods will overlap eventually, which results in an decreasing absorption layer and hence a lower current.

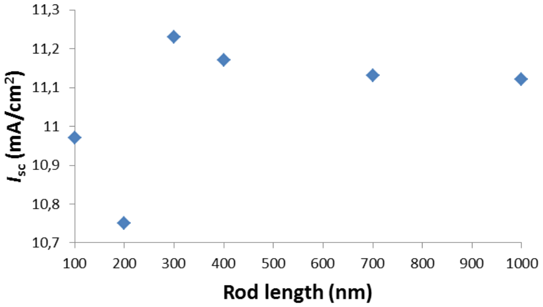

	$l = 100$ nm	$l = 200$ nm	$l = 300$ nm	$l = 400$ nm	$l = 700$ nm	$l = 1000$ nm
I_{sc} (mA/cm^2)	10.97	10.75	11.23	11.17	11.13	11.12

Fig. 50: The short-circuit current density as a function of rod length and the table with the exact values of the current densities.

4.5.2 The effect of the distance between each nanorods

The distance between the nanorods is varied between 100 nm and 600 nm, with a step of 100 nm. The length of the nanorods is 300 nm and the a-Si:H i-layer thickness is 200 nm, just like the original Ag nanorod sample. Because of the different distances, the interference patterns due to reflected photons and the path length differ significantly. The current density generated by the samples with different distances between the rods are shown in figure 52. It is difficult to find a trend in the wavelength shift of the absorption peaks, as shown in figure 51. In general it can be determined that a blue shift is observed and more peaks are shown when the distance between the rods is increased. According to the short-circuit current density of the samples, the sample with a distance of 600 nm between the rods generates the highest current density.

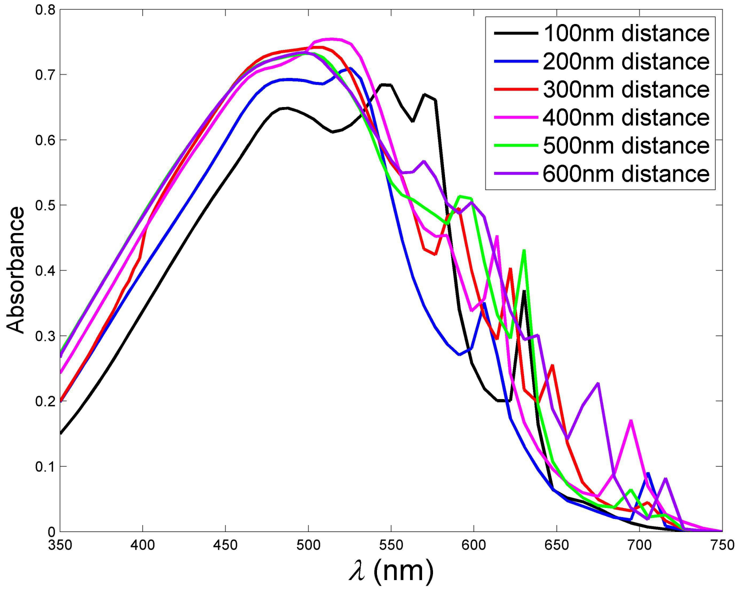

Fig. 51: Absorbance of different samples with a length of 300 nm, a i-layer thickness of 200 nm and a varying distances between the rods.

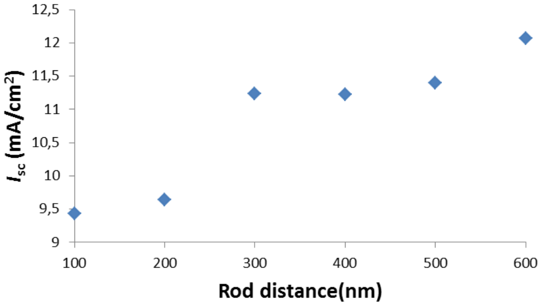

	$d = 100$ nm	$d = 200$ nm	$d = 300$ nm	$d = 400$ nm	$d = 500$ nm	$d = 600$ nm
$I_{sc}(\mathrm{mA/cm^2})$	9.43	9.64	11.24	11.23	11.40	12.07

Fig. 52: The short-circuit current density as a function of distance between the rods and the exact values of the current densities listed in a table

The results show an optimum of short-circuit current density at a distance of 600 nm. The lowest current density is obtained at a distance of 100 nm. Therefore, it can be concluded that a greater distance leads to a higher current density, which is probably caused by enhanced internal reflection in the a-Si:H i-layer of the solar cell. In addition, the closer the rods are to each other, the more the surface of the solar cell approaches that of a flat surface. Therefore, the effect of the nanostructures is nullified. Nevertheless, as shown in figure 52, the function of current density depending on rod distance is neither linear nor parabolic. Hence, it cannot be determined how this trend wil continue.

4.5.3 The effect of the thickness of the a-Si:H i-layer.

The thickness of the a-Si:H i-layer is varied between 50 nm and 300 nm with a step of 50 nm. In the former simulations, it is shown that the optimal distance between the nanorods is 600 nm. Therefore, the different a-Si:H i-layer thicknesses are simulated for both a 400 nm distance, the original Ag nanorod structure, and a 600 nm distance, the best nanorod structure within the simulated region. Additionally, the length of the rods is varied, to see the interaction between the thickness of the i-layer and the rod length.

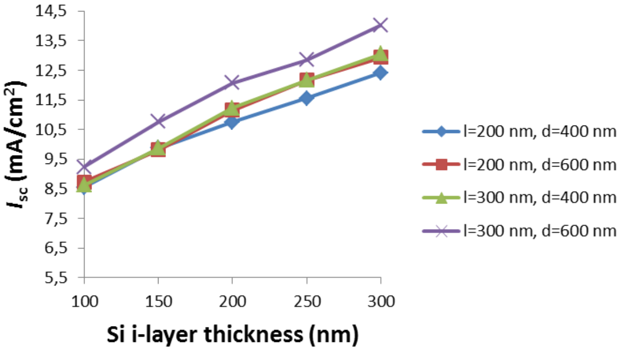

	$t = 50$ nm	$t = 100$ nm	$t = 150$ nm	$t = 200$ nm	$t = 250$ nm	$t = 300$ nm
I_{sc} (mA/cm^2)with $l = 200$ nm, $d = 400$ nm	6.03	8.55	9.88	10.75	11.55	12.42
I_{sc}(mA/cm^2) with $l = 200$ nm, $d = 600$ nm	6.50	8.73	9.81	11.16	12.16	12.94
I_{sc}(mA/cm^2) with $l = 300$ nm, $d = 400$ nm	6.37	8.63	9.88	11.23	12.16	13.06
I_{sc}(mA/cm^2) with $l = 300$ nm, $d = 600$ nm	6.94	9.24	10.76	12.07	12.85	14.02

Fig. 53: The short-circuit current density as a function of i-layer thickness and their values in the table.

The absorption spectra and current density for both 400 nm and 600 nm thick i-layer samples on rods with a length of 200 nm are similar, as shown in figure 54. The current density increases linearly with the increase in i-layer thickness, as shown in figure 53. A thicker i-layer results in higher current density in all samples, which is just as expected since in the simulations it is assumed that there is no carrier recombination. In addition, larger distance between rods also leads to a higher current density, as presented in figure 53.

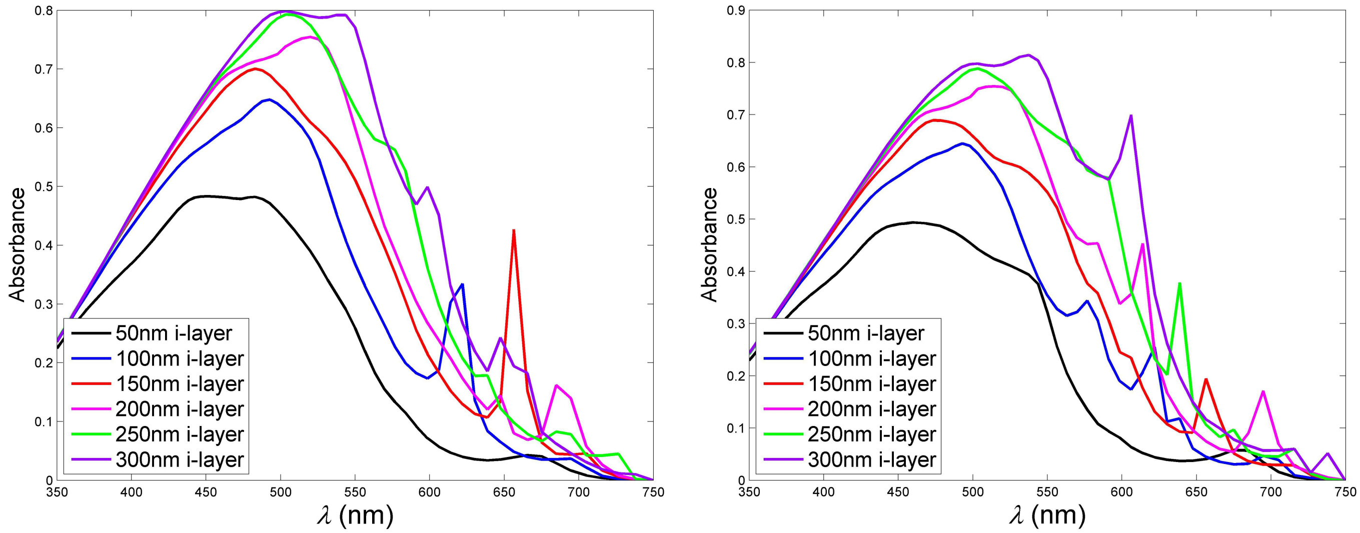

(a) Sample with $l = 200$ nm and $d = 400$ nm. (b) Sample with $l = 300$ nm and $d = 400$ nm.

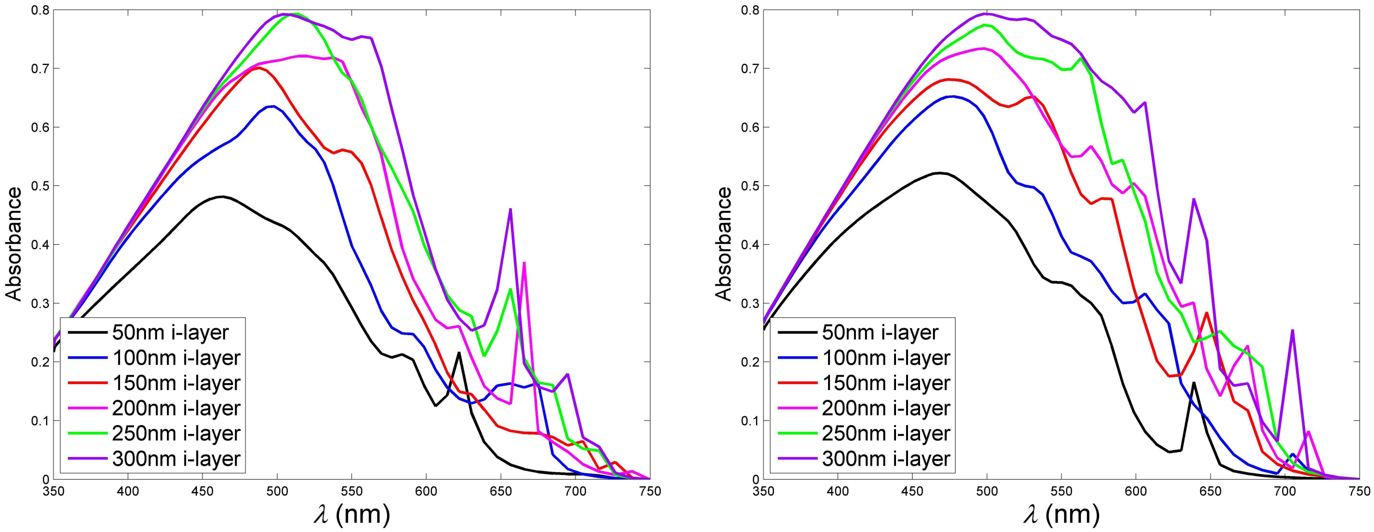

(c) Sample with $l = 200$ nm and $d = 600$ nm. (d) Sample with $l = 300$ nm and $d = 600$ nm.

Fig. 54: Absorbance of different samples with different lengths (l) and distances (d) between the rods with varying i-layer thickness.

4.6 Discussion

The results of the FDTD simulations of the nanorod structure are analyzed in this chapter. Due to the anti-reflection originating from the shape of the nanorods, the nanorod cell demonstrates improved blue and red response with respect to the flat reference solar cell. These results are in agreement with literature [3, 22, 61]. At longer wavelength several peaks appear due to the nanostructure. The absorption cross sections are studied to determine the origin of the absorption peaks. The origin of the absorption peaks for the Ag nanorod sample can be understood by comparison to samples with different structure and different metal back contact. High absorption is expected in the a-Si:H i-layer at small wavelength. Meanwhile, the results show a low absorption increasing towards an optimum at $\lambda = 520$ nm, because of the absorption in the ITO layer. The majority of the photons at small wavelength is absorbed in the ITO layer, due to its absorption coefficient shown in figure 40. The peak of the original Ag nanorod sample at $\lambda = 520$ nm, also observed in the absorption curve of the flat reference, can be assigned to interference of the reflected photons due to the presence of the Ag back reflector, which is also observed by Ferry et. al. [7, 12, 29]. The peaks are shifted to blue region with respect to the flat reference cell, caused by the anti-reflection of the nanorod shape. The peak at $\lambda = 584$ nm is obtained in both the Ag and the Au sample. Since the absorption cross sections of both samples are similar, it is assumed that they have the same origin. A slight difference in the patterns is caused by the different absorption properties of the metals. Based on these considerations, it can be concluded that this peak is caused mainly by the nanorod geometry and is independent on the metal.

The peak at $\lambda = 614$ nm appears in most of the samples. The absorption cross sections of samples with flat Ag and flat ZnO layers differ significantly from the original Ag nanorod sample. Hence, these samples do not appear to have the same origin. The peaks of samples with Ag, Au and Cu back contact very likely have the same origin. In contrast to these metal samples, the sample with flat metal has a deviated absorption cross section. Therefore, the origin of this peak is probably not the same as that for the peak in Ag nanorod sample at $\lambda = 614$ nm. Concluding, this peak originates in the structure of the nanorod solar cell with a metal nanorod in the center.

The last peak at $\lambda = 695$ nm is interesting to notice, since it appears in all metal samples and the sample without metal. Moreover, the cross sections of all of these samples correspond to each other. Only the absorption intensity of the different samples varies. From this point it can be concluded that this peak is caused by the reflection of the ZnO layer. When adding a metal layer under the ZnO layer, this reflection is amplified.

The structure of this solar cell is optimized for the following parameters; distance between the rods, rod lengths and a-Si:H i-layer thickness. When optimizing the layer thickness a correlation is found between the thickness and the current density, similar to results found by Ferry et. al [12]. The optimal structure for the highest absorption of the solar cell is the one with a distance of 600 nm between the rods, a rod length of 300 nm and and a-Si:H i-layer thickness of 300 nm, due to the optimal anti-reflection of the top layer, the internal reflection in the a-Si:H i-layer and the coating of the a-Si:H i-layer. However, since the absorption layer should be kept as thin as possible to reduce bulk recombination, it is probably better to reduce the thickness to 200 nm. By experimental research, the optimal thickness of the a-Si:H i-layer can be determined, since in the realistic case the recombination of carriers is taken into account.

4.7 Conclusion

The studies of this nanorod solar cell, indicate that the absorption enhancement originates from the reflection and the consecutive constructive interference of the Ag nanorod and the ZnO barrier layer. The absorption of photons with small wavelength in the solar cell can be described by Lambert-Beer Law by approximation. Due to absorption in the ITO layer at short wavelength, the absorption in the a-Si:H i-layer is decreased at this region. The peak at $\lambda = 520$ nm is assigned to constructive interference of reflected photons, which also occurs in a flat cell. The improved blue response is caused by the anti-reflective effect of the surface of the nanorod solar cell. Above $\lambda = 550$ nm the flat reference solar cell does not show any more absorption peaks. Therefore, the absorption peaks present for the Ag nanorod solar cell at longer wavelength are caused by the nanorod structure. The exact origin of these peaks is studied in this chapter. The two peaks at $\lambda = 584$ nm and $\lambda = 614$ nm originates from the presence of the metal nanorod in the center of the solar cell. By varying the metal, only the intensity of the absorption peak is influenced. The last peak at $\lambda = 695$ nm is originated from a combination at the reflection of the ZnO layer and of the metal layer. Again, different metals influence only the intensity of the absorption peaks. In order to make the simulations applicable to realistic case, 3D simulations are necessary. These simulations can differ considerably from 2D simulations. In order to make the simulations a more reliable approximation of the realistic solar cell, it is required to simulate a surface with random nanorods. Due to a periodic nanostructure, certain absorption effects might differ from a random distributed nanostructure, i.e., coupling between the nanorods and second order interference.

The optimal structure for the highest absorption of the solar cell is the solar cell with a distance of 600 nm between the rods, a rod length of 300 nm and and a-Si:H i-layer thickness of 200 nm. This can be explained by looking at the anti-reflective character of the top layer, internal reflection in the absorbing layer and the optimal coating of the a-Si:H i-layer. The sample without ZnO has the lowest absorption due to the increased parasitic absorption in the Ag layer caused by the absence of the protective ZnO layer [12, 37, 43]. The highest absorption is obtained by the sample with the flat Ag layer, which has the second highest calculated current density. In this sample, the benefits of the nanorod shape in the a-Si:H layer is remained. Due to this shape the optical path length is extended and the electron path is shortened. Thereby, the reflection of the top layer is reduced by the increased roughness of the surface. On the other hand, by applying a flat Ag layer, the reflection of this layer is maximized and the parasitic absorption of Ag is significantly reduced. These two features can obtain optimal reflection into the a-Si:H i-layer of the solar cell. It is worth noting that the obtained absorption approaches the absorption of the sample with a 250 nm thick i-layer.

5 FDTD simulations on the nanohole-based thin film solar cells

5.1 Abstract

In this chapter the FDTD simulations on the nanohole system will be discussed. This system is based on a structure former synthesized in our group. By simulating nanohole solar cells with different diameter sizes, the absorption of the system is investigated. Additionally, different nanohole structures are simulated to determine the origin of the absorption curves of the nanohole systems. After a short introduction, the nanohole structures of the solar cell will be explained in the third paragraph. In the next paragraph, the FDTD settings and the results will be discussed. By determining the current densities of the nanohole samples with different diameters, the diameter of the nanohole is optimized. This chapter will be completed with a discussion and conclusion.

5.2 Introduction on nanoholes

The second system simulated system is a solar cell with nanoholes at the back contact shown in figure 55. Idem, this solar cell is a previous work of our group by Dick van Dam [66]. Nanoholes in the metal back contact are interesting for solar cells due to their plasmonic properties. As mentioned in Chapter 2, plasmons can increase the absorption in the red region. Due to the holes, SPPs can propagate over the hole surface and couple to the a-Si:H layer, which causes absorption. Thereby, the holes can scatter light back into the absorber layer [69].

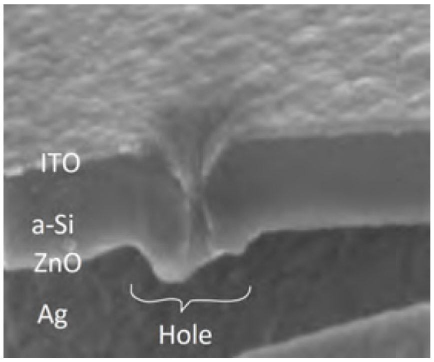

Fig. 55: A SEM image of cross section of the synthesized nanohole solar cell with 400 nm diameter hole [66].

In a former study five different nanohole systems were synthesized. All these structures are simulated in this thesis. The systems have different hole diameters of 50 nm, 100 nm, 200 nm, 300 nm and 400 nm. The flat reference solar cell is studied in paragraph 2.3. The absorption described by the Lambert-Beer law in first order and the absorption due to reflected photons are observed in this flat reference. The nanohole solar cells will be compared to this flat reference in this chapter.

5.3 The structure of nanoholes

The nanohole structures are studied because of the promising potency to generate SPP's and plasmonic scattering. Therefore, a Ag back reflector of 100 nm thick is deposited on a glass substrate. Holes of different diameters are placed in the back reflector. The synthesized solar cells are simulated as being a periodic surface of nanostructures. The coating is assumed to be conformal, and the ratio of the hole area versus the total surface will remain constant, i.e., the nanohole of 50 nm has a total surface of 250 nm and the nanohole of 100 nm has a total surface of 500 nm. It is assumed that there is no Ag in the middle of the hole. This structure is covered by 20 nm of ZnO, this layer is needed to avoid diffusion of Ag into the a-Si:H. The 20 nm thickness is the thinnest layer possible to produce in de lab and is thin enough that the plasmonic modes can couple to the a-Si:H. A 236 nm a-Si:H n-i-p junction (20 nm - 200 nm - 16 nm) of is stacked on the ZnO, the absorber layer. On top, 80 nm of ITO is placed as a transparent conductive layer. The cross sections of the simulated cells are shown in figure 56.

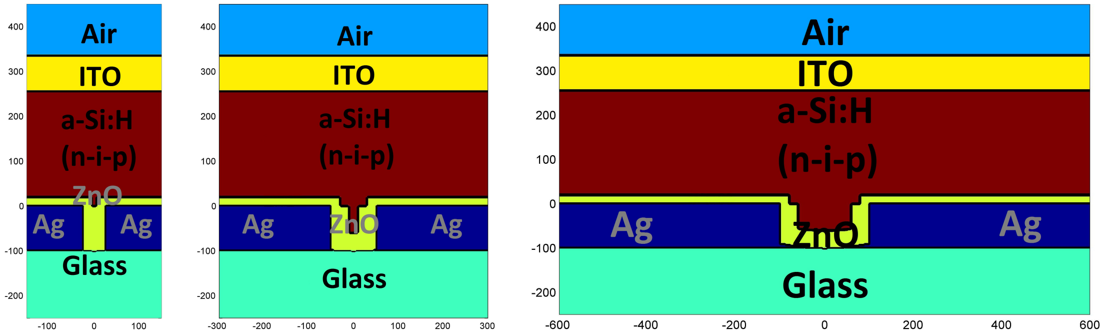

(a) 50 nm diameter (b) 100 nm diameter (c) 200 nm diameter

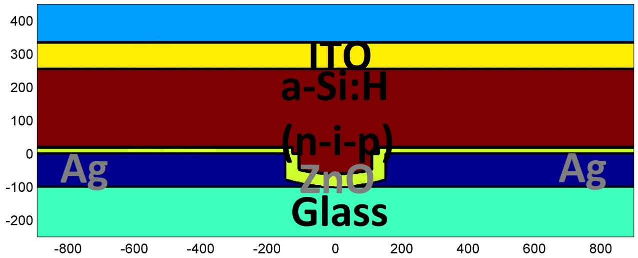

(d) 300 nm diameter

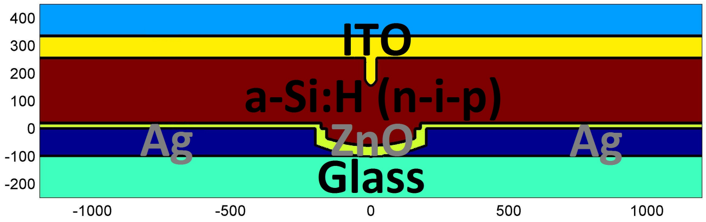

(e) 400 nm diameter

Fig. 56: Schematic FDTD cross section of Ag nanohole solar cells.

The samples without metal are simulated to determine the origin of the absorption curves of the nanohole Ag samples. For these samples, Ag is replaced by ZnO. Further, the structure is kept the same (figure 57). The absorption curves of both samples will be compared, to find out which peaks of the Ag nanohole samples are caused by the Ag layer, and which are caused by the ZnO layer or the morphology. Absorption peaks that appear in both the samples with and without Ag, are probably not caused by the Ag layer hence probably not plasmonic. If there are peaks which are only present in the Ag, it is important to do further investigation. Therefore, samples are simulated with other metals, i.e.: Al, Au and Cu, since different metals contain different plasmonic response [43]. From these results a peaks shift could denote a plasmonic effect.

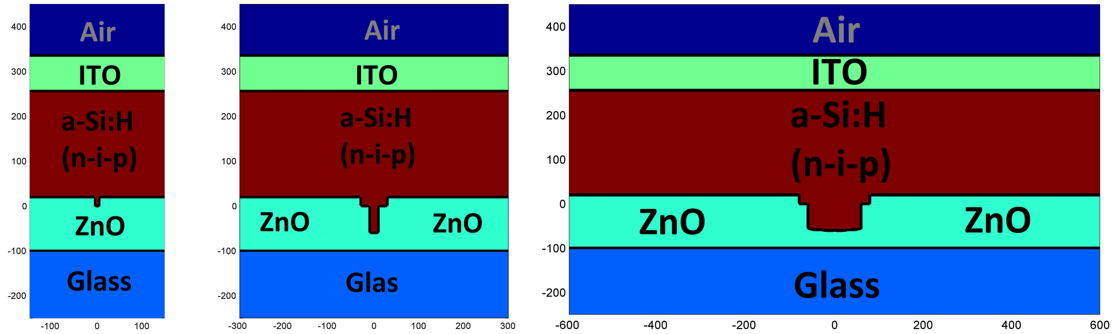

(a) 50 nm diameter.

(b) 100 nm diameter.

(c) 200 nm diameter.

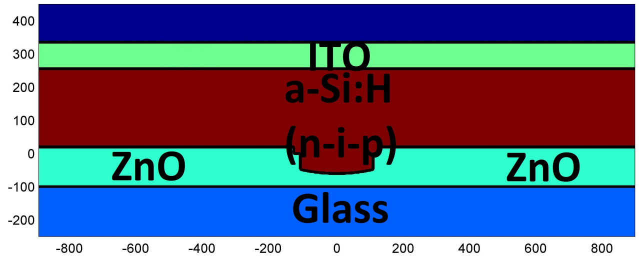

(d) 300 nm diameter.

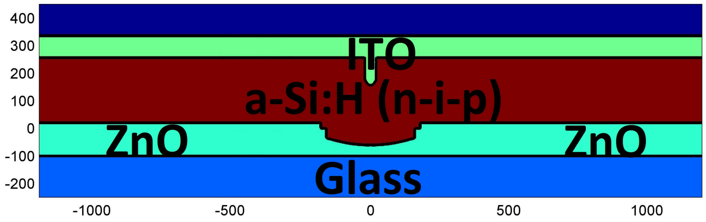

(e) 400 nm diameter.

Fig. 57: Schematic FDTD cross sections of the nanohole solar cells without Ag.

5.4 Simulated optical properties of the nanohole-based cells

5.4.1 FDTD settings nanoholes

For these FDTD simulations, the same settings are used as for the nanorod system discussed in paragraph 4.4.1. Both are 2D simulations, with a mesh size of 2 nm and 100 frequency points. The material database of the nanorod systems is also used for the nanohole solar cells (figure 40), since the materials in used the lab are the same. Also the calculations for the QE and the current are done are done similar as discussed in paragraph 4.4.1.

5.5 FDTD results nanoholes

The analysis of the results of the nanohole solar cells is done similar to the analysis of the nanorod solar cells. Since the nanoholes are small enough to cause coupling to plasmonic modes, it is expected that some peaks of these samples are left unexplained by using the same analysis. As discussed in Chapter 2, the plasmon modes depend on the size of the nanohole. Therefore, the samples with different nanohole size are compared to each other. Thereby, the plasmonic effect is a property of a metal, so different metals are compared to see if certain absorption peaks shift.

5.5.1 Analysis of the absorption curves

Comparing samples with different nanohole size. The absorption curves of the flat reference together with the Ag samples with different hole diameters are shown in table 8. The curves are similar at short wavelength till $\lambda = 550$ nm. The absorption curves of all samples contain two absorption maxima at $\lambda = 464$ nm and $\lambda = 526$ nm. At short wavelength the photons are absorbed by the ITO layer due to its refractive index, shown in figure 40. Therefore, the absorption in the a-Si:H i-layer is lower than expected. The second absorption peak is caused by constructive interference of either the reflected photons or the scattered photons or a combination of both. Since the surface of the nanohole solar cells shows a negligible change with respect to the flat solar cell, the absorption maximum at 464 nm remains the same in all samples. On the other hand, the maximum at 526 nm differs in absorption intensity. This absorption maximum is caused by the interference of reflected photons and is therefore influenced by the nanoholes at the Ag back reflector.

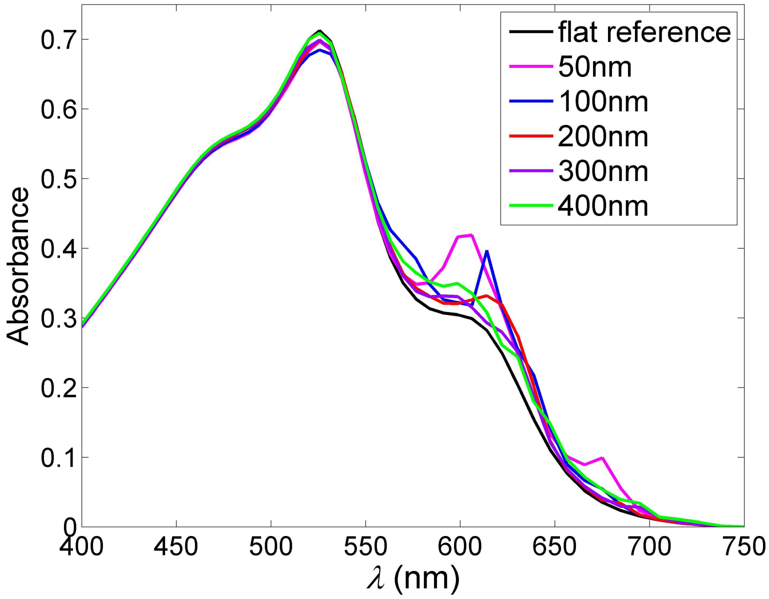

Fig. 58: Absorption in a-Si:H i-layer of nanohole solar cells with varying diameter.

Hole Diameter	λ_{peak} (nm) of sample with Ag				
50 nm	464	526	598	606	675
100 nm	464	526	577	614	675
200 nm	464	526		614	685
300 nm	464	526	591	622	695
400 nm	464	526	598	630	695

Tab. 8: Absorption peaks in a-Si:H i-layer of Ag nanohole samples .

The more interesting part of the absorption curves is between $\lambda = 550$ nm and $\lambda = 750$ nm. In this region, the nanohole samples show peaks, which do not appear at the absorption spectrum of the flat reference. The wavelengths of the peaks of the absorption curves are shown in table 8. The results for the nanohole structures shows a peak shift into red region. A spectral shift is observed due to an increased diameter. The three absorption peaks at longer wavelength are shifted to red region, when the hole diameter is increased from 50 nm to 400 nm. This trend can denote absorption enhancement due to plasmonic effects. One exception is the peak at $\lambda = 598$ nm of the Ag 50 nm nanohole sample.

Analysis of the absorption spectra of the nanohole samples with and without Ag. The absorption spectra of the nanohole samples are compared per hole diameter to the samples without Ag, shown in figure 58. Both samples of 50 nm nanohole with and without Ag back reflector obtain the first peak at $\lambda = 464$ nm as shown in figure 57a. Up to this wavelength the absorption can be described by the Lambert-Beer Law. This absorption depends on the absorption coefficient of the a-Si:H layer. Therefore, these results are in agreement with the expectations. The second absorption maximum, caused by the interference of reflected photons, is significantly lower for the sample without Ag back reflector, with respect to the Ag 50 nm nanohole sample. This can be explained by the removed Ag back reflector. Consequently, less photons are reflected back into the solar cell by the ZnO layer. After $\lambda = 509$ nm, no more peaks appear in the 50 nm nanohole sample without Ag back reflector. Therefore, the two peaks in the absorption spectrum of the 50 nm hole sample with Ag at longer wavelength are probably caused by the metal structure. Though the origin of the peaks is still unknown.

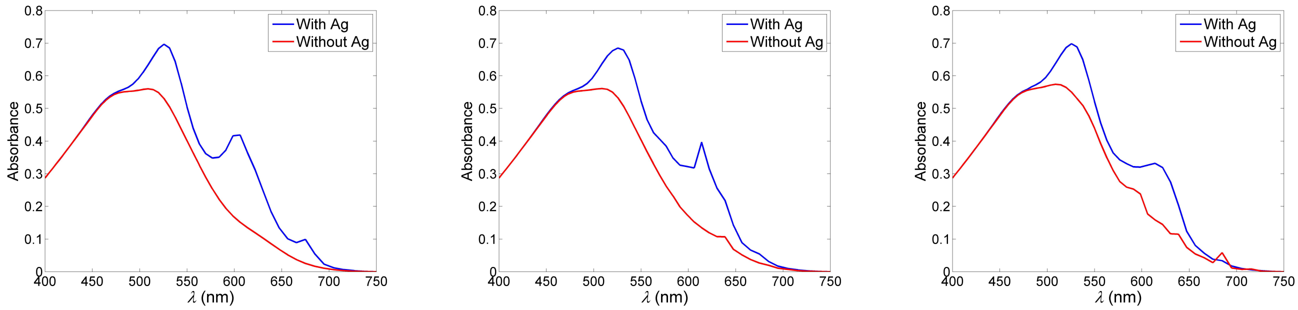

(a) 50 nm diameter. (b) 100 nm diameter. (c) 200 nm diameter.

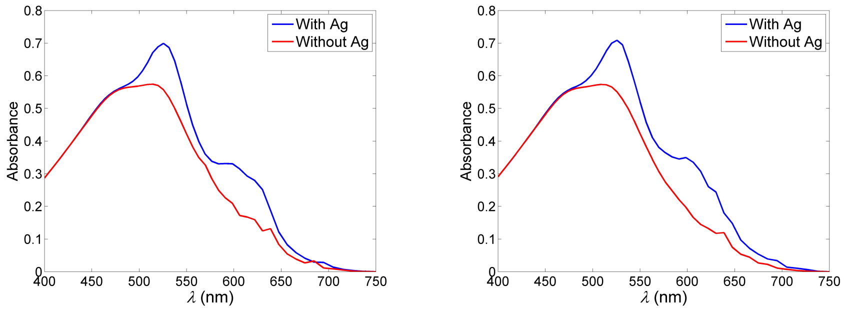

(d) 300 nm diameter. (e) 400 nm diameter.

Fig. 59: Absorption in a-Si:H i-layer of nanohole samples with and without Ag varying diameter.

Hole Diameter	λ_{peak} (nm) of sample without Ag					
50 nm	464	509				
100 nm	464	509			638	
200 nm	464	509	598		638	685
300 nm	464	509	577	622	638	685
400 nm	464	509	538		666	685

Tab. 9: Absorption peaks in a-Si:H i-layer of nanohole samples without Ag.

The 100 nm nanohole samples show similar photon absorption at short wavelength as the 50 nm nanohole samples, as shown in figure 57b. At longer wavelength a new peak appears in the 100 nm nanohole sample without Ag back reflector. This peak does not correlate to the peak of the 100 nm nanohole Ag sample, as shown in tables 8 and 9. Therefore, these peaks are caused by different effects. Consequently, the peaks of the Ag sample at $\lambda = 614$ nm and $\lambda = 675$ nm are caused by the Ag structure.

At short wavelength, the same counts for the 200 nm, 300 nm and 400 nm nanohole samples. The absorption curves of the nanohole samples without Ag back reflector show more absorption peaks when increasing the hole diameter. The 200 nm nanohole samples have one peak in common at $\lambda = 685$ nm. Therefore, this peak might not be caused by the Ag nanohole structure. Additionally, the 300 nm nanohole samples have one peak in common at $\lambda = 622$ nm. In order to find out the origin of these peaks, analysis of the absorption patterns of the absorption cross sections will take place.

Comparison different metals. The Ag nanohole solar cells are compared to samples with different metals. In this case the structure of the samples is maintained and the Ag back contact is replaced by Ag, Al, Au and Cu. The absorption of the samples with different metals per hole diameter are shown in figure 60 and the exact wavelengths of the peaks are enlisted in the tables 10, 11 and 12. The 50 nm nanohole samples, shown in figure 60a, all contain the two known peaks at short wavelength. At longer wavelength the absorption curves of varying metal back contact samples differ. The peak at $\lambda = 598$ nm appears in the Al 50 nm nanohole sample. The absorption at that wavelength of the Ag 50 nm nanohole sample is significantly higher than the absorption of the Al 50 nm nanohole solar cell. This might be originated from a higher reflection index of Ag or a lower absorption in the Ag layer. After analysing the origin of the absorption cross sections of these samples, it can be concluded whether these peaks are caused by the same effect or not. The Ag nanohole sample with a diameter size of 100 nm, shown in figure 60b, has no correlating peaks with the different metal samples. Therefore, the origin of these peaks remain undefined.

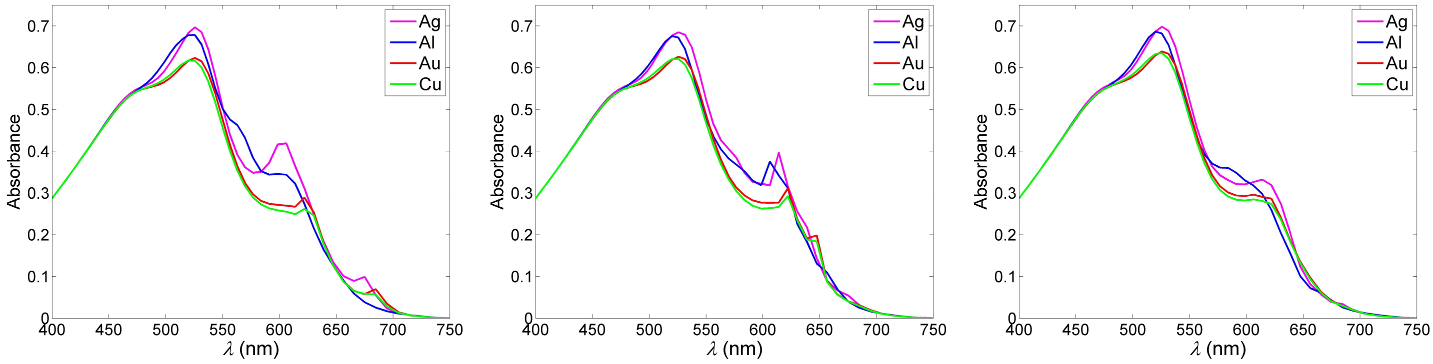

(a) 50 nm diameter. (b) 100 nm diameter. (c) 200 nm diameter.

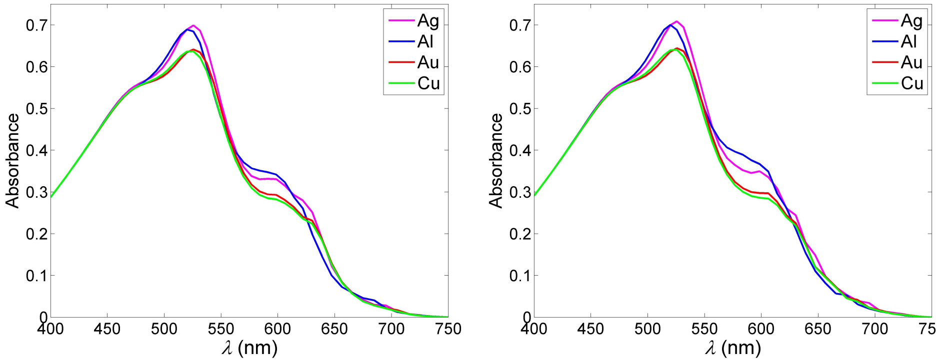

(d) 300 nm diameter. (e) 400 nm diameter.

Fig. 60: Absorption in a-Si:H i-layer of different nanohole metal samples with varying diameter.

The peak at $\lambda = 614$ nm of the Ag 200 nm nanohole sample also appears in the Al 200 nm nanohole sample, as shown in figure 60c. The absorption of the Ag nanohole is higher than the absorption of the Al nanohole. To determine whether these peaks have the same origin, their absorption cross sections will be analyzed further in this paragraph.

Hole Diameter	λ_{peak} (nm) of Al sample					
50 nm	464	526	563	598		
100 nm	464	520	584	606	622	656
200 nm	464	520	584		614	666
300 nm	464	520		598	622	685
400 nm	464	520		598		

Tab. 10: Absorption peaks in a-Si:H i-layer of Al nanohole samples.

The 622 nm peak of the Ag nanohole sample is also present in the Al 300 nm nanohole sample as shown in figure 60d. Additionally, a peak at this wavelength is observed in the 300 nm nanohole sample without Ag back reflector. Therefore, it seems likely that this peak is independent of the metal properties and its structure. This only counts when the peaks originate from the same effect.

Hole Diameter	λ_{peak} (nm) of Au sample				
50 nm	464	526		622	685
100 nm	464	526	584	622	647
200 nm	464	526		622	666
300 nm	464	526	598	630	705
400 nm	464	526	606	630	685

Tab. 11: Absorption peaks in a-Si:H i-layer of Au nanohole samples.

At $\lambda = 598$ nm there are two correlating peaks with the Ag 400 nm nanohole sample, as shown in figure 60e. This peak is also observed in the Au 400 nm nanohole sample and the Cu 400 nm nanohole sample. The peak at $\lambda = 630$ nm is shown in the Ag, Au and Cu 400 nm nanohole samples. The absorption cross section analysis will follow in the next paragraph, in order to find out the origin of all peaks.

Hole Diameter	λ_{peak} (nm) of Cu sample					
50 nm	464	526		622		685
100 nm	464	526		622	647	
200 nm	464	526		622		
300 nm	464	526	598	606	630	
400 nm	464	526		606	639	685

Tab. 12: Absorption peaks in a-Si:H i-layer of Cu nanohole samples.

5.5.2 Analysis of the absorption cross sections

The interference patterns of the absorption cross sections are analyzed in different ways. First the absorption cross sections are studied and then analyzed similar to the analysis of the thin film solar cells in section 2.4. After, the absorption cross sections are compared to the other samples which contain the same peak in the absorption spectrum.

The interference analysis is executed using the same method as explained in section 2.4 for the flat solar cells. The observed periodicity in the a-Si:H i-layer is determined by measuring the distances between the absorption maxima. The calculated wavelength in the a-Si:H i-layer is calculated by using equation 18.

At all samples, the two peaks at small wavelength of $\lambda = 464$ nm and $\lambda = 526$ nm are observed. These also appear in the absorption spectrum of the flat reference. Therefore, these are probably all caused by the same effect, explained in section 2.4. At small wavelength, light is absorbed by the ITO layer due to its absorption coefficient. As this absorption decreases, the absorption in the a-Si:H i-layer increases because of its absorption coefficient. The absorption peak at

$\lambda = 526$ nm is probably caused by optimal constructive interference in the solar cell. This can be confirmed by looking at the absorption cross sections of all samples, shown in figure 61b, 64b, 65b, 67b and 70b. The absorption in the nanohole solar cells is lower with respect to the flat reference cell. This is caused by the absence of the metal in the hole and ohmic losses in the metal.

50 nm nanohole absorption cross sections. The absorption spectrum of the Ag 50 nm nanohole contains five peaks of interest. The absorption cross sections at these wavelengths are shown in figure 61. The origin of the first two peaks at $\lambda = 464$ nm and $\lambda = 526$ nm are discussed above.

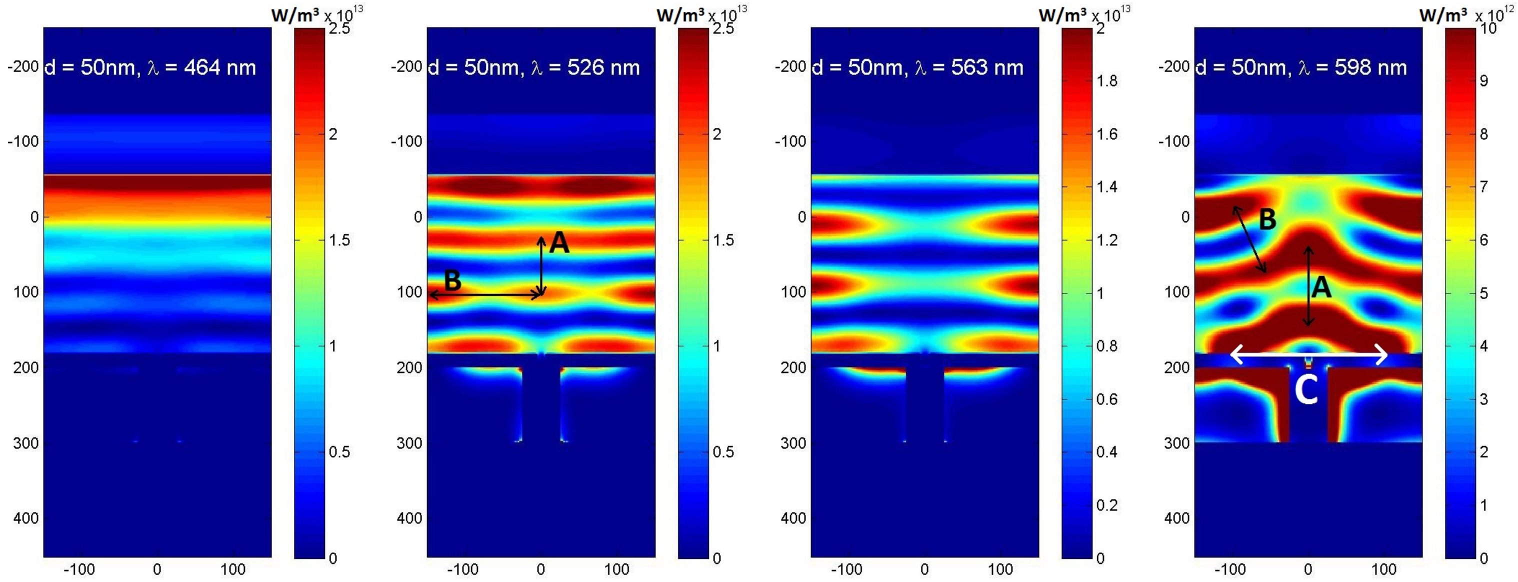

(a) $\lambda = 464$ nm (b) $\lambda = 526$ nm (c) $\lambda = 562$ nm (d) $\lambda = 598$ nm

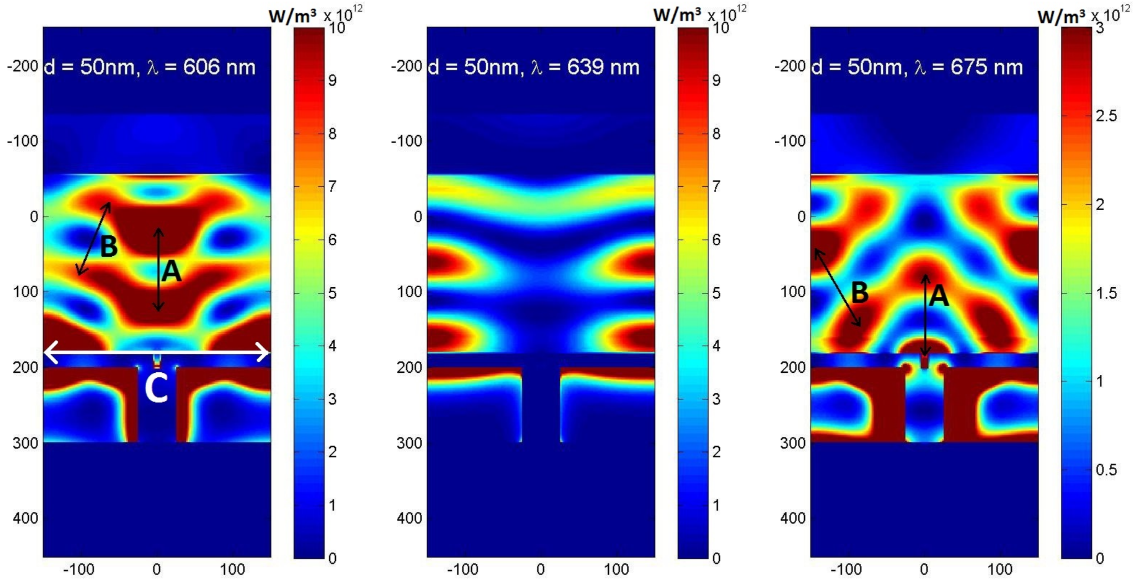

(e) $\lambda = 606$ nm (f) $\lambda = 639$ nm (g) $\lambda = 675$ nm

Fig. 61: Absorption cross sections of peaks of the 50 nm nanohole sample.

The absorption at $\lambda = 526$ nm is slightly lower than that of the flat reference. The absorption peak at $\lambda = 526$ nm is caused by optimal interference and is characterized by a broad peak. The absorption cross section shows the influence of the nanohole on the reflection of light at this wavelength, as shown in figure 61b. Due to the presence of the nanohole and the ohmic loss in the Ag layer, the absorption at this wavelength is reduced slightly with respect to the flat solar cell. The determined distances between the absorption maxima in the a-Si:H i-layer of the absorption cross section and the calculated wavelengths for this layer are listed in table 13. The distance between the absorption maxima above the nanohole (A) in a-Si:H is similar to the calculated wavelength from the spectrum for this layer. In contrast to the flat solar cell, a lateral periodicity (B) is observed of ∼ 280 nm, due to the presence of the nanohole. The distance between the absorption maxima of this periodicity resembles the periodicity of the nanoholes (∼ 300 nm).

λ_{air} (nm)	$n_{Si}(\lambda_{air})$	Calculated λ_{Si} (nm)		Observed λ_{Si} (nm)
526	3.712	141.7	A	137.9 ± 5.4
			B	281.1 ± 5.4
598	3.459	172.9	A	196.2 ± 5.4
			B	190.9 ± 5.4
			C	300.0 ± 5.4
606	3.441	176.1	A	206.8 ± 5.4
			B	196.2 ± 5.4
			C	600.0 ± 5.4
675	3.283	205.6	A	206.8 ± 5.4
			B	212.1 ± 5.4

Tab. 13: Analysis of absorption cross sections of peaks of 50 nm nanohole sample.

The peaks at $\lambda = 598$ nm, $\lambda = 606$ nm and $\lambda = 675$ nm are originated from resonance. Their cross sections show more complex interference patterns, shown in figure 61d, 61e and 61g, respectively. The interference patterns are strongly influenced by the presence of the nanohole, above the nanohole respectively two or three absorption maxima appear. In general, the absorption cross sections at resonance wavelength show roughly similar distances between the absorption maxima above the 50 nm nanohole and above the flat surface with a phase shift. In addition, the distances between the absorption maxima in the a-Si:H layer deviate from calculated wavelength (table 13). Another interesting feature is the relatively strong absorption in the metal, which is shown in the absorption cross sections of all three wavelengths. This probably denotes surface plasmons in the Ag layer. In addition, all samples have a relative high absorption located at the bottom of the a-Si:H layer, which might be induced by coupling to surface plasmon modes. Remarkable features of the absorption cross sections will be discussed per resonance peak from the spectrum.

The absorption cross section at $\lambda = 598$ nm (figure 61d) has an increasing phase between the absorption maxima above the nanohole and above the flat surface. In the lateral absorption maxima periodicity in the a-Si:H layer does not correlate to the lateral maxima periodicity in the Ag layer. The two absorption maxima in the Ag layer are at the corner of the nanohole and in between the nanohole. On the other hand, the lateral absorption maxima in the a-Si:H layer are localized at the absorption minima in the Ag layer.

The reflection at the metal layer to the a-Si:H at $\lambda = 606$ nm is relatively strong (figure 61e). The lateral absorption of in the a-Si:H layer in the absorption cross section correlates to the lateral absorption in the Ag layer and is similar to the nanohole periodicity ($^1/_2\lambda_{Si} = 300$ nm). This lateral absorption could presumably be caused by the surface plasmons or by the lateral components of the scattering on the nanohole. A shift of the absorption maxima above the nanohole (with respect to the periodicity above the flat surface) is again observed, probably caused by the back reflection of the nanohole.

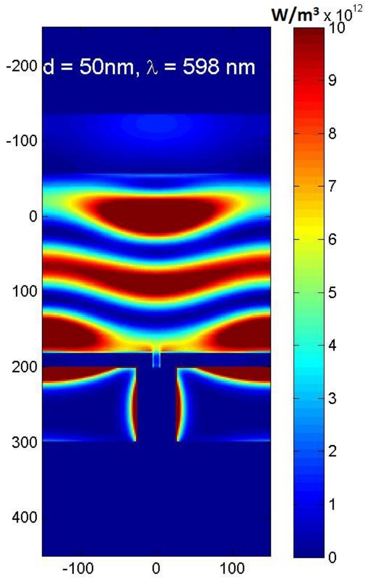

Fig. 62: The absorption cross sections of Al nanohole sample at $\lambda = 598$nm.

The absorption cross section of the resonance peak at λ = 675 nm is shown in figure 61g. A circular absorption pattern appears above the nanohole, probably caused by a back scattering nanohole. Strong absorption is observed in the nanohole in the a-Si:H i-layer and at the corners of the nanohole in the ZnO nanohole. This is possibly caused by surface plasmons in the Ag layer localized at the corners of the nanohole, and might result in scattering of the nanohole. At the top and the bottom of the Ag film symmetric absorption is observed, which can be obtained due to the use of thin film Ag, explained in section 2.2.2 [46].

The absorption cross sections at λ = 563 nm and λ = 639 nm are shown in figure 61c and 61f, respectively. No significant absorption is observed above the nanohole. A presumable explanation is that at these wavelengths light is not reflected and probably no resonance is obtained.

The absorption peak at λ = 598 nm also appears in the Al nanohole sample. To find the origin of the peak of both samples, the cross section of this sample is shown in figure 62. Comparing this interference pattern to the pattern of the Ag nanohole sample, the Al sample strongly deviates. The absorption maxima and minima in the a-Si:H i-layer of both absorption cross sections do not correlate. In the metal layer, both samples show relatively strong absorption, though the absorption patters differ significantly. Therefore, this peak appears to be metal dependent and could possibly find its origin in a different plasmonic behaviour.

100 nm nanohole sample. The absorption cross sections of the five absorption peaks of the 100 nm nanohole samples are shown in figure 64. Additionally, two absorption cross sections at local absorption minima are shown in this figure. The absorption cross sections at short wavelength (λ = 464 nm and λ = 526 nm) can be assigned to the same effects as determined for the Ag 50 nm nanohole solar cell.

The absorption at the optimal interference peak λ = 526 nm is decreased with respect to the flat reference due to the nanoholes in the Ag back reflector. The absorption cross section is shown in figure 64b. Above the nanohole (A) and above the flat surface (B) similar distances between the absorption maxima is observed as calculated in the a-Si:H i-layer at this wavelength (table 14). Above the nanohole no absorption is observed. This is probably caused by the absence of the Ag back reflector, hence no photons are reflected back into the a-Si:H i-layer. An interesting observation is the absorption inside the Ag walls of the nanohole, as shown in the enlarged absorption cross section in figure 63. In the enlarged absorption cross section confined resonances are observed. The distance between the absorption maxima in the metal (D) is in the orders of 20 nm, ten times smaller than the surface plasmons on the Ag surface.

λ_{air} (nm)	$n_{Si}(\lambda_{air})$	Calculated λ_{Si} (nm)		Observed λ_{Si} (nm)
526	3.712	141.7	A	139.3 ± 7.8
			B	143.1 ± 7.8
			D	224.4 ± 7.8
			E	19.3 ± 7.8
577	3.527	163.6	A	181.8 ± 7.8
			B	170.2 ± 7.8
			C	193.4 ± 7.8
614	3.415	179.8	A	185.7 ± 7.8
			B	193.4 ± 7.8
			C	193.4 ± 7.8
675	3.283	205.6	A	224.4 ± 7.8
			B	224.4 ± 7.8
			C	255.4 ± 7.8

Tab. 14: Analysis of absorption cross sections of peaks of 100 nm nanohole sample.

At the resonance peaks more complex absorption patterns are formed. At $\lambda = 577$ nm, the first resonance peak, a small absorption enhancement is shown in the absorption of the a-Si:H i-layer. The absorption cross section shows a strong interaction between the photons and the nanohole, as shown in figure 64c. A lateral periodicity with a distance between the absorption maxima of ~ 195 nm is observed in the absorption cross section due to the presence of the nanohole. This absorption is also present in the Ag layer and therefore probably caused by a surface plasmon. The distances between the absorption maxima observed in the a-Si:H i-layer (A and B in figure 64c) resembles the calculated wavelength, listed in table 14. A cone shape with phase shifted absorption maxima, appears in the absorption cross section. This is possibly originated from a scattering hole. Additionally, changes are seen in the absorption pattern of a short distance between the absorption maxima in the Ag nanohole.

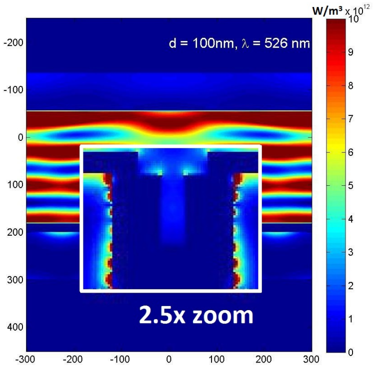

Fig. 63: Enlarged Ag 100 nm nanohole at $\lambda = 526$ nm.

The same applies for the absorption cross section at $\lambda = 614$ nm as shown in figure 64e. Moreover, a complex interference pattern is observed probably caused by different effects including surface plasmons. The lateral periodicity (C) resembles the absorption maxima in the Ag layer. This periodicity is interrupted above the nanohole. When moving up to the top layer of the a-Si:H i-layer, a strong absorption is shown with a similar distance between the absorption maxima as the lateral periodicity. The distance between the absorption maxima above the flat surface correlates to the calculated wavelength in the a-Si:H i-layer, as listed in table 14.

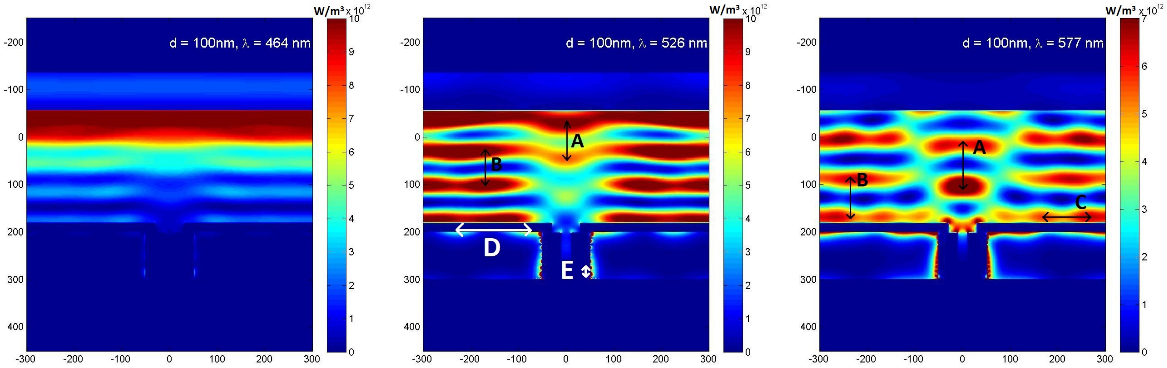

(a) $\lambda = 464$ nm (b) $\lambda = 526$ nm (c) $\lambda = 577$ nm

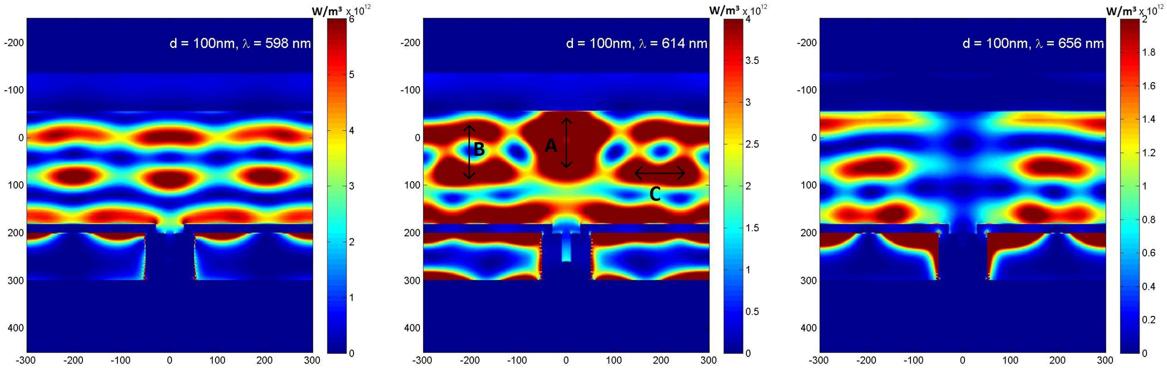

(d) $\lambda = 598$ nm (e) $\lambda = 614$ nm (f) $\lambda = 656$ nm

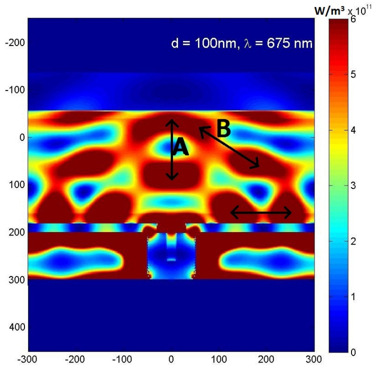

(g) $\lambda = 675$ nm

Fig. 64: Absorption cross section of 100 nm nanohole sample.

The last resonance peak is at $\lambda = 675$ nm is shown in figure 64g. At the absorption cross section a typical circular absorption pattern also observed in the 50 nm nanohole. This is probably caused by surface plasmons and a back scattering nanohole. Strong absorption in the ZnO layer at the corners of the metal nanohole appear, and an increased absorption in and right above the nanohole. This might be caused by surface plasmon modes localized on the corners of the Ag layer. In the Ag layer anti-symmetric absorption appears (explanation in section 2.2.2) [46]. The distance between the absorption maxima above the hole (A) and above the flat surface (B) are similar to the calculated absorption in the a-Si:H i-layer, listed in table 14.

At $\lambda = 598$ nm low absorption is obtained. The absorption cross section at this wavelength shows an interference pattern, as shown in figure 64d. The lateral absorption periodicity in the a-Si:H i-layer is equal to the lateral absorption periodicity in the Ag layer. Therefore, it seems likely that surface plasmons in the Ag layer couple to the a-Si:H i-layer.

Though, the obtained absorption is relatively low. Also at $\lambda = 656$ nm, shown in figure 64f, relatively low absorption is observed. In absorption cross section no significant absorption appears above the nanohole. This looks similar as the absorption cross section of the 50 nm nanohole at $\lambda = 639$ nm (see figure 61f) and presumably is a result of the same effect, i.e.: no reflected light and probably no resonance.

200 nm nanohole sample. In figure 65 the absorption cross sections of the four absorption peaks of the Ag 200 nm nanohole samples are shown, and two absorption cross sections of local absorption minima at $\lambda = 591$ nm and $\lambda = 639$ nm. At small wavelength the absorption patterns are comparable with the samples of 50 nm and 10 nm nanohole diameters. Therefore the absorption peaks at $\lambda = 464$ nm and $\lambda = 526$ nm can be assigned to the same effect as for the former samples, shown in figure 61a, 61b, 64a and 64b.

λ_{air} (nm)	$n_{Si}(\lambda_{air})$	Calculated λ_{Si} (nm)		Observed λ_{Si} (nm)
526	3.712	141.7	A	153.9 ± 5.1
			B	143.6 ± 5.1
			D	318.1 ± 5.1
614	3.415	179.8	A	205.2 ± 5.1
			B	174.4 ± 5.1
			D	410.4 ± 5.1
685	3.263	209.9	B	225.7 ± 5.1
			C	790.1 ± 5.1
			D	790.1 ± 5.1

Tab. 15: Analysis of absorption cross sections of peaks of 200 nm nanohole sample.

At higher wavelength two peaks appear at respectively $\lambda = 614$ nm and $\lambda = 685$ nm. Both cross sections have different interesting features. At $\lambda = 614$ nm a strong absorption is observed in and right above the nanohole. On the other hand, at $\lambda = 685$ nm no absorption is present in the nanohole. Instead, four maxima are distributed over the flat surface, which correspond to absorption maxima in the metal layer.

As in the former samples, the optimal interference of the 200 nm nanohole solar cell is at $\lambda = 526$ nm, shown in figure 65b. The absorption pattern is similar to the former samples at this wavelength (figure 61b and 64b), with similar observed distance between the absorption maxima in A and B as calculated according to equation 18. The exact wavelengths are listed in table 15. In the Ag layer, symmetric lateral absorption (D) is observed with a distance between the absorption maxima of $\sim$ 320 nm [46]. This lateral periodicity is not observed significantly in the a-Si:H i-layer. Therefore, this absorption in the Ag layer probably causes ohmic losses.

The peaks at $\lambda = 614$ nm and $\lambda = 685$ nm are originated from resonance. The absorption cross section at $\lambda = 614$ nm, shown in figure 65d, contains strong resonance due to the nanohole with a longer distance between the absorption maxima in the a-Si:H i-layer (A) than calculated as listed in table 15. On the contrary, the distance between the absorption maxima above the flat surface (B) in the a-Si:H i-layer is similar to the calculated wavelength. At the edges of the absorption cross section, lateral periodicity is observed in the a-Si:H i-layer, possibly due to strong coupling of the surface plasmons in the Ag layer with a distance between the absorption maxima of $\sim$ 410 nm, which correlates to the plasmon modes of Ag in vacuum determined by Novotny and Hecht ($\sim$ 340 nm) [43].

At $\lambda = 685$ nm anti-symmetric like absorption is observed in the Ag layer, as shown in figure 65f [46]. This is probably caused by a surface plasmon. Similar absorption is observed in the a-Si:H i-layer, which might denote coupling between the surface plasmon and the a-Si:H.

The lateral periodicity lengths C and D in both layers contain the same distances between the absorption maxima, as shown in table 15. Above the nanohole, the absorption is extinguished, due to the absence of the reflection. The distance between the absorption maxima B in the a-Si:H i-layer above the flat surface is similar to the calculated wavelength in this layer.

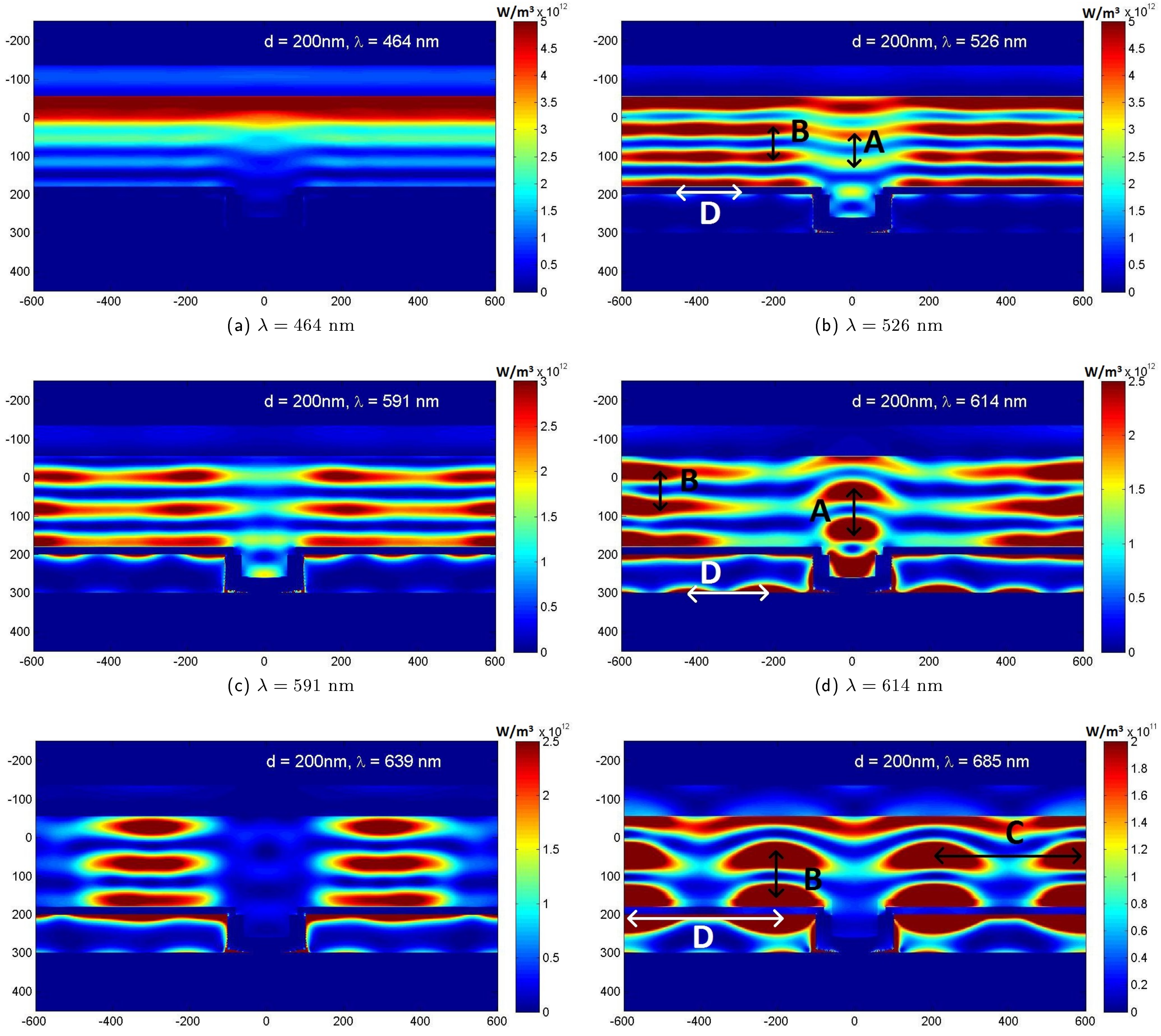

(a) $\lambda = 464$ nm

(b) $\lambda = 526$ nm

(c) $\lambda = 591$ nm

(d) $\lambda = 614$ nm

(e) $\lambda = 639$ nm

(f) $\lambda = 685$ nm

Fig. 65: Absorption cross section of 200 nm nanohole sample.

The absorption cross sections of the two absorption minima at $\lambda = 591$ nm and $\lambda = 639$ nm are shown in figure 65c and 65e, respectively. In the absorption cross section at $\lambda = 591$ nm low absorption is observed above the nanohole, which is significantly lower than the absorption at $\lambda = 614$ nm. Additionally, the absorption above the flat surface appears to be significantly lower. The absorption cross section at $\lambda = 639$ nm shows no absorption above the hole. The absorption above the flat surface is localized at sites and limited to six absorption maxima. Therefore, it seems plausible that there is no resonance at these wavelengths.

The resonance peaks at $\lambda = 614$ nm and $\lambda = 685$ nm also appear in the different 200 nm nanohole sample. First resonance peak appears in the Al 200 nm nanohole sample. The absorption cross section of the Al 200 nm nanohole sample is shown in figure 66a. In the Al nanohole significantly lower absorption is observed than in the Ag 200 nm nanohole sample. In addition, the absorption on the flat surface of the Al 200 nm nanohole sample is increased with respect to the Ag nanohole sample. Therefore, the absorption patterns are dependent on the metal properties and looking at the absorption patterns both peaks originate from a plasmonic effect. The absorption enhancement of the Ag nanohole sample seems to be originated from a scattering nanohole.

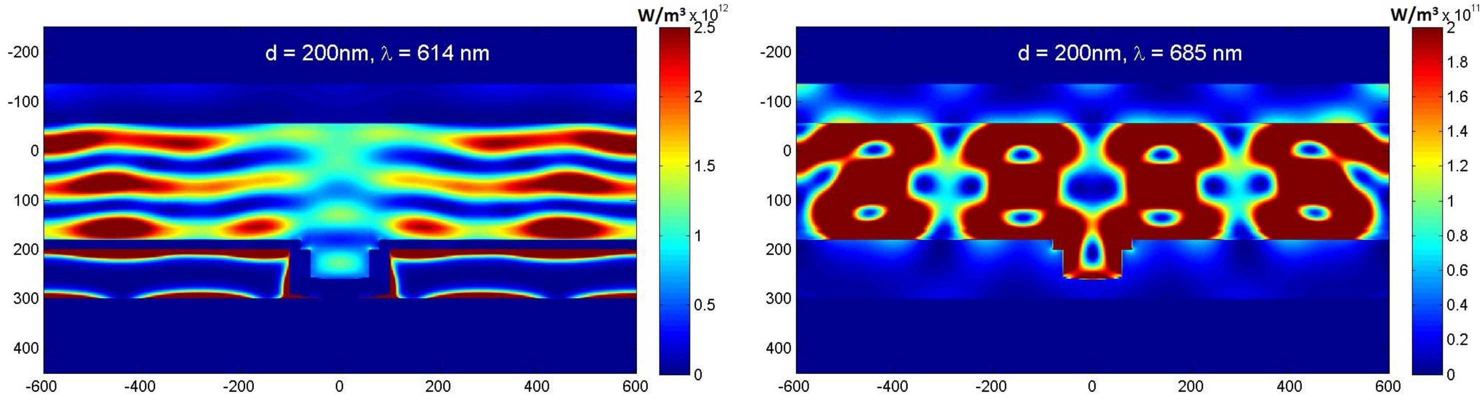

(a) Al nanohole sample at $\lambda = 614$nm.

(b) Nanohole sample without Ag at $\lambda = 685$nm

Fig. 66: The absorption cross sections of the absorption peaks of the other samples.

The absorption peak at $\lambda = 685$ nm is also obtained in the 200 nm nanohole sample without metal, as shown in figure 59c. The absorption pattern, shown in figure 66b, differs significantly from the Ag nanohole sample. Both show four absorption maxima in the a-Si:H layer. However, the patterns differ and strong absorption is observed in the metal layer of the Ag nanohole sample.

300 nm nanohole sample. The absorption cross section of the Ag 300 nm nanohole sample at $\lambda = 464$ nm, shown in figure 67a, is again assigned to the effect described above this section. The absorption cross section at $\lambda = 526$ nm, see figure 67b, shows an interference pattern similar to the interference pattern of the flat solar cell. Above the nanohole the absorption is extinguished and the phase of the absorption maxima is slightly shifted. This is probably caused by the absence of Ag at the nanohole, which causes different reflection of light. In the absorption cross section, the distance between the absorption maxima above the nanohole (A) and above the flat surface (B) is similar to the calculated wavelength in the a-Si:H i-layer, listed in table 16. Absorption in the Ag layer is observed in both absorption cross sections which do not couple to the a-Si:H i-layer. At the walls of the Ag nanohole show confined resonance, as shown in an enlarged absorption cross section in figure 68. This might denote plasmon resonances within the nanohole. The confined resonance seems similar to the resonance in the resonance in the Ag 100 nm nanohole sample at $\lambda = 526$ nm.

The two absorption cross sections of the resonance peaks at longer wavelength have more complicated absorption patterns. At $\lambda = 622$ nm four absorption maxima in and above the nanohole and increased absorption are observed in the Ag layer, as shown in figure 67d. A similar distance between the absorption maxima is observed above the nanohole (A) and above the flat surface (B). This distance between the absorption maxima resembles the calculated wavelength for the a-Si:H i-layer at this wavelength, as listed in table 16. Probably due to scattering of the nanohole, a phase shift of A is obtained with respect to B. Lateral periodicity is observed in the a-Si:H i-layer which might be caused by coupling of the surface plasmons in the Ag layer. In the Ag layer anti-symmetric absorption appear with super position of an absorption maximum at the top of the Ag layer, which can only occur at thin film metals [46].

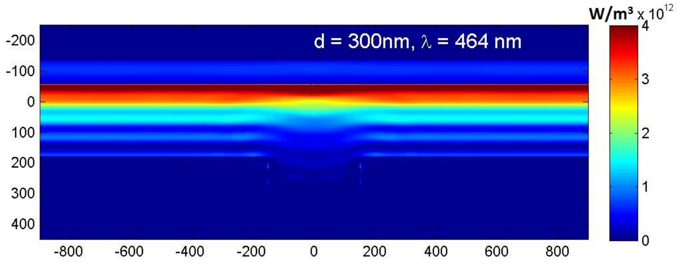

(a) $\lambda = 464$ nm (b) $\lambda = 526$ nm

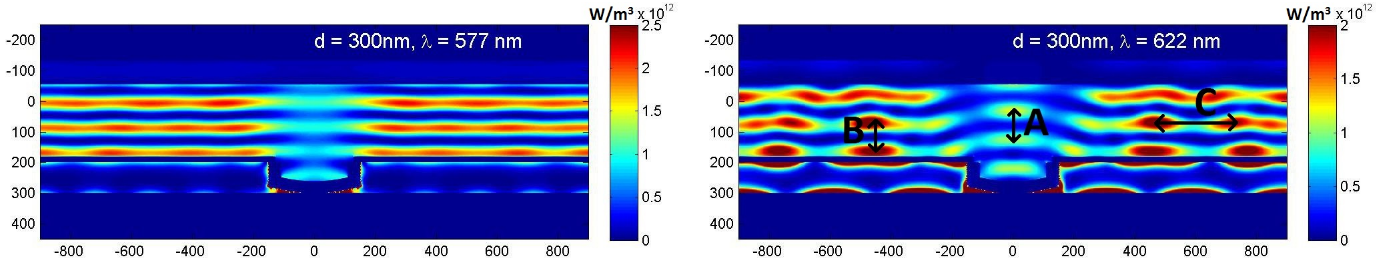

(c) $\lambda = 577$ nm (d) $\lambda = 622$ nm

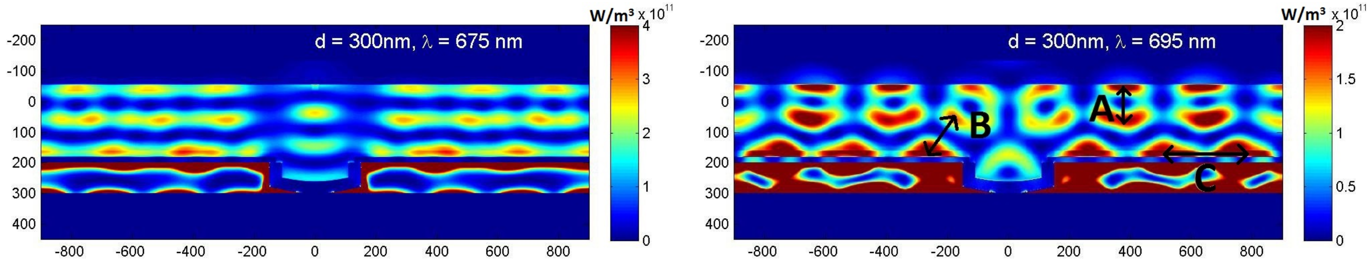

(e) $\lambda = 675$ nm (f) $\lambda = 695$ nm

Fig. 67: Absorption cross section of 300 nm nanohole sample.

λ_{air} (nm)	$n_{Si}(\lambda_{air})$	Calculated λ_{Si} (nm)		Observed λ_{Si} (nm)
526	3.712	141.7	A	152.3 ± 7.6
			B	$137.0 + 7.6$
			D	304.5 ± 7.6
			E	30.5 ± 7.6
622	3.391	183.4	A	197.9 ± 7.6
			B	190.3 ± 7.6
			C	639.5 ± 7.6
695	3.249	213.9	A	258.8 ± 7.6
			B	243.6 ± 7.6
			C	487.2 ± 7.6

Tab. 16: Analysis of absorption cross sections of peaks of 300 nm nanohole sample.

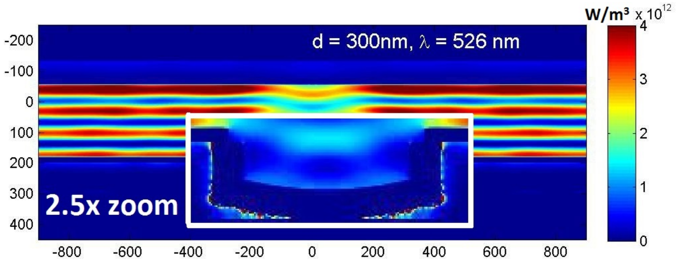

Fig. 68: Enlarged absorption cross section of the Ag 300 nm nanohole at $\lambda = 526$ nm.

This absorption on both sides of the metal is strongly increased at $\lambda = 695$ nm. At this wavelength, a complex interference pattern is shown in the absorption cross section, shown in figure 67f. This is probably caused by surface plasmon in the Ag layer which can couple to the a-Si:H i-layer and scattering of the nanohole. The absorption distances between the absorption maxima A and B are vertical and diagonal absorption above the flat surface, respectively. The lateral periodicity in the a-Si:H i-layer has the same distance between the absorption maxima as the anti-symmetric plasmon modes in the Ag layer.

The absorption patterns in the absorption cross sections at the minima $\lambda = 577$ nm and $\lambda = 675$ nm are similar to the patterns of the absorption maxima. Though, the net absorption at these wavelengths is significantly lower. This can probably be explained by the fact that no optimal interference is obtained at these wavelengths.

The absorption peak at $\lambda = 622$ nm also appears at the 300 nm nanohole sample without a Al back reflector (figure 59d). The absorption cross sections of the 300 nm nanohole sample without Ag is shown in figure 69a. On one hand, the intensity of the absorption is low with respect to the Ag 300 nm nanohole sample. On the other hand, the absorption pattern is similar to the pattern of the Ag 300 nm nanohole sample. Therefore, the 300 nm nanohole sample without Ag represents the scattering of the ZnO nanohole. Possibly due to this scattering of the nanohole, lateral periodicity is obtained. The absorption cross section of the Al 300 nm nanohole sample resembles the Ag nanohole sample, as shown in figure 69b. The metal layers enhance the absorption due to scattering of the ZnO hole. The absorption difference between the Al 300 nm nanohole sample and Ag 300 nm nanohole sample is due to the different optical properties of the metals.

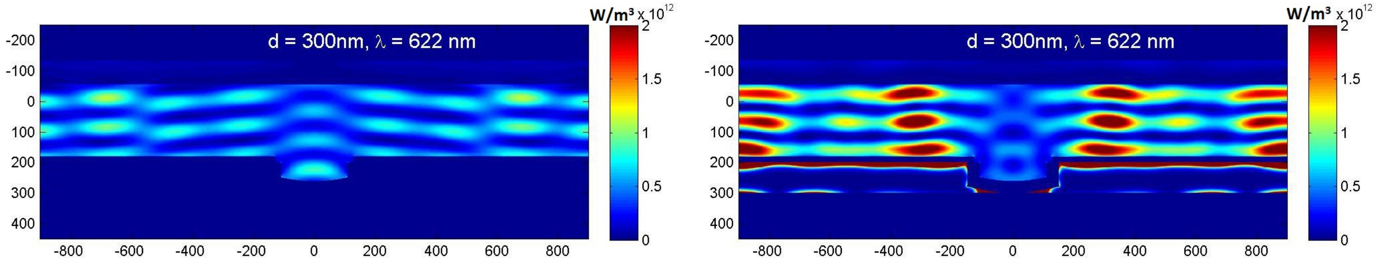

(a) Nanohole sample without Ag at $\lambda = 622$nm.

(b) Al nanohole sample at $\lambda = 622$nm

Fig. 69: The absorption cross sections of the absorption peaks of the other samples.

400 nm nanohole sample. The simulations of the 400 nm Ag sample resulted in the absorption cross sections are shown in figure 70. In the absorption cross section at $\lambda = 526$ nm, shown in figure 70b. The distance between the absorption maxima determined above the hole (A) is similar to the distance between the absorption maxima above the flat surface (B) with a phase shift. The distances between the absorption maxima resemble the calculated wavelength in the a-Si:H i-layer, as listed in table 17. A small absorption is observed in the Ag layer, as shown in the enlarged absorption cross section in figure 71. The distance between the absorption maxima is$\sim$ 280 nm and in the walls of the nanohole with a distance between the absorption maxima ten times smaller ($\sim$ 25 nm). This seems to be the same confined resonance as in the 100 nm and 300 nm nanohole samples.

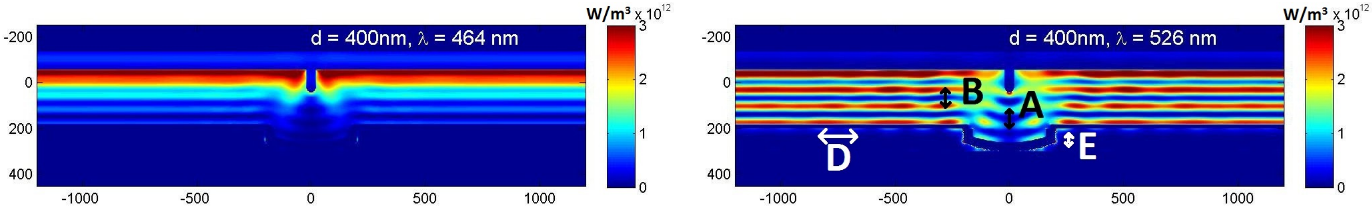

(a) $\lambda = 464$ nm (b) $\lambda = 526$ nm

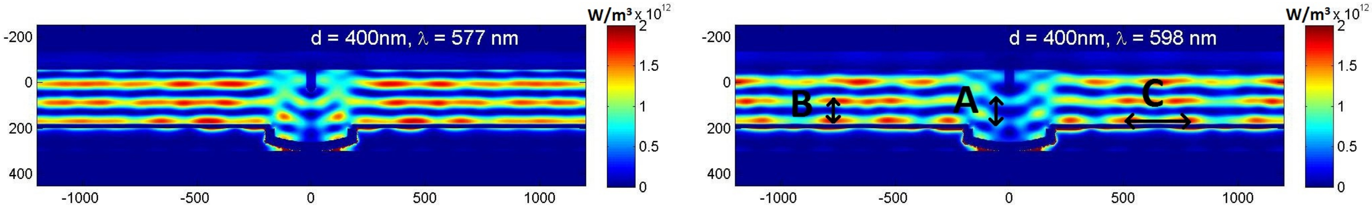

(c) $\lambda = 577$ nm (d) $\lambda = 598$ nm

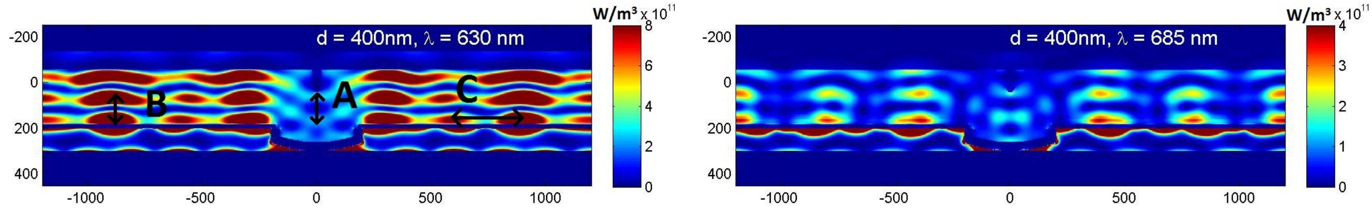

(e) $\lambda = 630$ nm (f) $\lambda = 685$ nm

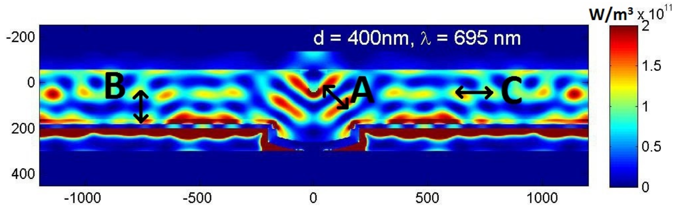

(g) $\lambda = 695$ nm

Fig. 70: Absorption cross section of 400 nm nanohole sample.

The small resonance peaks of the Ag 400 nm nanohole sample are at $\lambda = 598$ nm, $\lambda = 630$ and $\lambda = 695$ nm. The absorption cross section at $\lambda = 598$ nm shows an interference pattern with lateral absorption maxima probably due to the scattering hole and a surface plasmon in the Ag layer, as shown in figure 70d. Above the nanohole, a small absorption is observed with similar distance between the absorption maxima (A) as above the flat surface (B). These distance between the absorption maxima correlate to the calculated wavelength in the a-Si:H i-layer (table 17). The lateral periodicity (C) in the a-Si:H layer is equal to the periodicity in the Ag layer. At the Ag walls, similar absorption is shown as at $\lambda = 526$ nm.

Similar lateral absorption periodicity is observed in the Ag and the a-Si:H layer at $\lambda = 630$ nm , as shown in figure 70e, with a symmetric periodicity of $\sim$ 560 nm in both layers [46]. The absorption above the nanohole is extinguished, this might be caused by an inactive nanohole or destructive interference. Small absorption is shown with a distance between the absorption maxima (A) of $\sim$ 220 nm, alike the distance between the absorption maxima above the flat surface (B).

The absorption cross section at $\lambda = 695$ nm shows strong absorption at the corners of the nanohole in the a-Si:H i-layer with a diagonal periodicity of $\sim$ 220 nm (A). This might be caused by surface plasmons in the Ag layer localized at the corners. The periodicity of the absorption maxima above the flat surface (B) is similar to A. The lateral periodicity (C) is $\sim$ 560 nm and is possibly caused by coupling to the plasmon modes in the Ag layer.

λ_{air} (nm)	$n_{Si}(\lambda_{air})$	Calculated λ_{Si} (nm)	Observed λ_{Si} (nm)	
526	3.712	141.7	A	125.9 ± 15.7
			B	141.6 ± 15.7
			D	283.2 ± 15.7
			E	25.2 ± 15.7
598	3.459	172.9	A	157.3 ± 15.7
			B	157.3 ± 15.7
			C	472.0 ± 15.7
630	3.376	186.6	A	220.3 ± 15.7
			B	220.3 ± 15.7
			C	566.4 ± 15.7
695	3.249	213.9	A	220.3 ± 15.7
			B	220.3 ± 15.7
			C	566.4 ± 15.7

Tab. 17: Analysis of absorption cross sections of peaks of 400 nm nanohole sample.

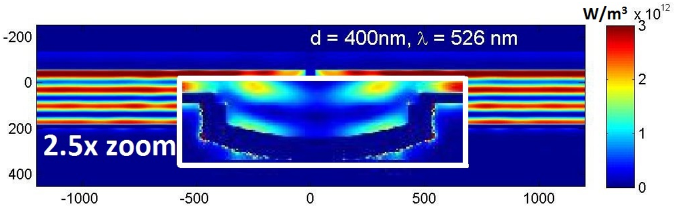

Fig. 71: Enlarged absorption cross section of the Ag 400 nm nanohole at $\lambda = 526$ nm.

The two absorption cross sections at the absorption minima $\lambda = 577$ nm and $\lambda = 685$ nmare shown in figure 70c and figure 70f, respectively. The first absorption cross sectionat $\lambda = 577$ nm is similar to the absorption cross section at absorption peak $\lambda = 598$ nm. On the contrary, the net absorption is significantly lower, which is probably caused by the the fact that the constructive interference at this wavelength is not optimal. The absorption in the a-Si:H i-layer of the absorption cross section at $\lambda = 685$ nmis significantly low. On the other hand, the absorption in the Ag layer is still relatively high. Hence, it seems likely that the absorption at this wavelength is low, since the Ag layer and the a-Si:H i-layer are not in resonance and high ohmic losses take place.

The absorption peak at $\lambda = 598$ nm appears in the Al nanohole sample. The absorption cross section of this sample at the specific wavelength is shown in figure 72a. The cross sections of both samples are similar, with the exception of the absorption pattern above the nanohole. This small difference is negligible. Therefore, this absorption peak is probably caused by the metal structure of the solar cell, however it is not metal dependent and thus is probably not induced by a plasmonic effect. The same presumably applies for the absorption peak at $\lambda = 630$ nm, which also appears in the absorption spectrum of the Au nanohole. The absorption cross section of this sample is shown in figure 72b, in which a similar absorption as the absorption pattern of the Ag nanohole sample is observed.

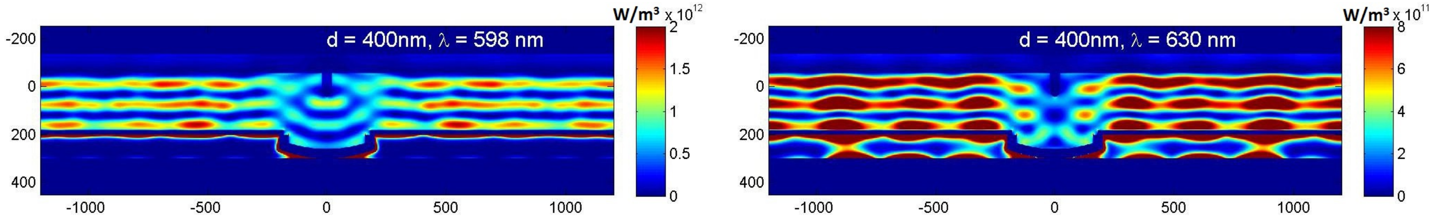

(a) Al nanohole sample at $\lambda = 598$nm.

(b) Au nanohole sample at $\lambda = 630$nm.

Fig. 72: The absorption cross sections of the absorption peaks of the other samples.

5.5.3 Optimization nanohole solar cell

The caclulated open circuit current densities of all samples are plotted in figure 73 and the values are enlisted in table 18. The current densities of the samples without metal are significantly lower with respect to the samples with a metal back contact. Additionally, performance differences are observed between the nanohole solar cells with different metal back contacts.

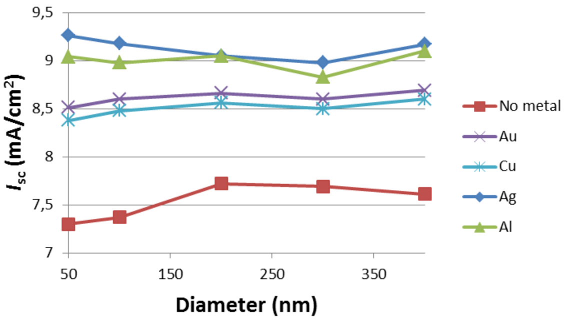

Fig. 73: Current densities of nanohole solar cell.

	d=50 nm	d=100 nm	d=200 nm	d=300 nm	d=400 nm
I_{sc}(mA/cm^2) Ag	9.26	9.18	9.05	8.98	9.17
I_{sc}(mA/cm^2) Non metal	7.30	7.37	7.72	7.69	7.61
I_{sc}(mA/cm^2) Al	9.04	8.98	8.84	8.85	9.10
I_{sc}(mA/cm^2) Au	8.51	8.60	8.66	8.60	8.69
I_{sc}(mA/cm^2) Cu	8.38	8.48	8.56	8.50	8.60
I_{sc}(mA/cm^2) flat reference	8.77	8.77	8.77	8.77	8.77

Tab. 18: Open circuit current densities of nanohole solar cells.

5.6 Discussion

At short wavelength the flat and nanohole sample appear to have the same absorption. This similar absorption can be assigned to the similar texture of the surface of both solar cells, due to the small size of the nanoholes at the back contact. Following from the absorption coefficient of a-Si:H, the absorption at small wavelength is expected to be higher. However, due to the absorption in the ITO layer, this absorption is significantly lower. At longer wavelength the absorption curves differ significantly. Peaks appear in the nanohole solar cell, which are not present in the flat reference.

Five varying hole sizes are studied, i.e.: a hole diameter size varying from 50 nm, 100 nm, 200 nm, 300 nm and 400 nm. All samples absorption at short wavelength with about the same absorption intensity. At longer wavelength different peaks appear in the absorption spectra of the different nanohole solar cells. From theory, it is derived that plasmon modes of nanoparticles are shifted into red region, when the particle radius is increased [25, 37]. This same effect is observed in the results of this study. The increasing absorption till $\lambda = 464$ nm is assigned to the decreasing absorption in the ITO layer. The peak at $\lambda = 526$ nm can be ascribed, when studying the absorption cross sections, to constructive interference of the reflected photons. The deviating peaks are interpreted separately per nanohole diameter. The absorption in the nanohole samples is slightly lower than in the flat sample, due to the lack of reflection above the nanohole, concluded from the absorption cross sections. This typical absorption pattern is also found among others [7, 12, 29].

In most samples, a phase shift is shown between the absorption maxima above the nanohole and the absorption maxima above the flat surface. This observation is also made by Sha et al. and Dewan et al., and is probably caused by the lower laying back reflector in the nanohole [7, 54].

Additionally, it is important to point at a remarkable observation in the 100 nm, 300 nm and 400 nm nanohole samples at $\lambda = 526$ nm. These samples show confined resonances within the nanohole, which probably denote plasmon resonances in the nanohole. The resonances are in the characteristic order of plasmon resonances [43].

50 nm nanohole Ag solar cell. The Ag 50 nm nanohole sample has three interesting absorption peaks at $\lambda = 598$ nm, $\lambda = 606$ nm and $\lambda = 675$ nm. These peaks are absent in the samples without metal, therefore it can be concluded that the metal structure causes these peaks. When comparing to the different metal samples, i.e.: Al, Au and Cu, only the peak at $\lambda = 598$ nm appears in the Al 50 nm nanohole sample. The absorption patterns in the a-Si:H i-layer of the absorption cross sections of both samples differ significantly. The absorption cross section of the Ag 50 mn nanohole sample is clearly influenced by the nanohole. The exact origin from this pattern cannot be derived from this absorption cross section. The lateral periodicity in the absorption cross section at $\lambda = 606$ nm probably denotes surface plasmons in the Ag layer [12, 25, 37]. Due to the similar lateral periodicity in the a-Si:H i-layer, the surface plasmons probably couple to the a-Si:H i-layer. At $\lambda = 675$ nm the absorption cross section probably also shows surface plasmons. At this wavelength the lateral periodicity is observed at the front and the back of the metal. According to Park et al, this indicates a symmetric surface plasmon configuration of a thin film [46]. The observed circular absorption pattern is found among others for a likewise nanohole in a metal film [12, 46]. According to literature this pattern is caused by surface plasmons in combination with back scattering from the nanohole. The circular absorption pattern also shows absorption maxima and minima, which are, by our knowledge, not found in literature. An interesting feature at this wavelength is the strong absorption in the ZnO layer at the corners of the Ag nanohole and the absorption within the nanohole in the a-Si:H layer. This is probably caused by the surface plasmons localized on the corners of the Ag layer. The absorption cross sections at the absorption minima $\lambda = 563$ nm and $\lambda = 639$ nm show no absorption above the hole which probably comes from the fact that at these wavelengths there is no resonance.

100 nm nanohole Ag solar cell. The three interesting absorption peaks are at $\lambda = 577$ nm, $\lambda = 614$ nm and $\lambda = 675$ nm. Since none of these peaks is observed in the samples without Ag or with a different metal, they are caused by the Ag back contact. At $\lambda = 577$ nm strong absorption takes place at the corners of the nanohole in the a-Si:H layer. In addition, a cone shape of absorption maxima is observed above the nanohole. Though it can not be said with certainty what the origin of this absorption pattern is. More detailed analysis of the absorption cross section at this wavelength is required in order to find out the origin of this peak. Both peaks at $\lambda = 614$ nm and $\lambda = 675$ nm similar lateral absorption periodicity is observed in the Ag and the a-Si:H i-layer. This lateral periodicity probably indicates surface plasmons, which can couple to the a-Si:H i-layer and enhance the absorption [12, 25, 37]. In addition, at $\lambda = 675$ nm the circular absorption pattern is shown, which denotes surface plasmons in combination with a back scattering nanohole [12, 46]. Another effect is observed: strong absorption is shown in the ZnO layer at the Ag corners of the nanohole. This effect is also observed by Sha et al. [54], and is presumably caused by the surface plasmons localized at the corners of the Ag layer. This results in absorption maxima and minima in the circular absorption. The absorption cross section at $\lambda = 596$ nm, and absorption minimum, contains an absorption pattern in the metal characteristic for a surface plasmon [12, 25, 37]. The relatively low absorption at this wavelength can probably be explained by the surface plasmons that do not seem to couple efficiently to the a-Si:H i-layer.

200 nm nanohole Ag solar cell. The two absorption cross sections of the 200 nm nanohole Ag sample at the two peaks with longer wavelength seem to be very interesting. Both show similar lateral periodicity in the metal layer and coupling to the a-Si:H layer. This presumably denotes surface plasmon in the Ag layer. Apart from the possible surface plasmons coupling, the absorption cross section at $\lambda = 614$ nm shows strong absorption above the nanohole, probably caused by a scattering hole. This peak is also observed in the Al nanohole sample. Both absorption patterns differ significantly, hence the origin of this peak for both samples differs and dependents on the metal. Concluding, the difference in the absorption patterns at this wavelength is caused by the different optical properties of the metals. At $\lambda = 685$ nm the lateral absorption appears to be very clear, which indicates surface plasmons [12, 25, 37]. This peak is also observed in the absorption spectrum of the nanohole sample without metal. However, since this absorption cross section differs significantly from the absorption cross section of the Ag nanohole sample, the origin of both peaks is not the same. Therefore, it still seems plausible that the absorption of the Ag nanohole at this wavelength can be assigned to coupling of the surface plasmon modes. The absorption cross section of the absorption minimum at $\lambda = 591$ nm shows typical surface plasmon absorption patterns in the metal [12, 25, 37]. No significant absorption enhancement is observed at this wavelength, probably since the coupling to the a-Si:H i-layer does not predominate the parasitic absorption in the metal.

300 nm nanohole Ag solar cell. The absorption curve of the 300 nm nanohole Ag sample contains two interesting peaks. Since the absorption cross section at $\lambda = 622$ nm of both samples with and without metal layer contain a similar absorption pattern, the origin of both peaks at this wavelength is probably the same. The lateral absorption periodicity can be caused by the scattering ZnO hole. The addition of the metal layer increases the absorption significantly. In the absorption cross section at $\lambda = 695$ nm a surface plasmon is presumably observed, in reference to literature [12, 25, 37]. In addition, possible scattering of the nanohole might result in a complex interference pattern in the a-Si:H i-layer.

400 nm nanohole Ag solar cell. The last simulated samples is the 400 nm nanohole Ag solar cell. The three discussed absorption peaks are at $\lambda = 598$ nm, $\lambda = 630$ nm and $\lambda = 695$ nm. Both absorption peaks at $\lambda = 598$ nm and $\lambda = 630$ nm also appear at the Al nanohole and Au nanohole sample, respectively. The absorption cross sections at both wavelengths are similar to cross sections of the Ag nanohole sample. The absorption pattern at $\lambda = 598$ nm looks similar to the pattern of the Ag 300 nm nanohole sample at $\lambda = 622$ nm. Therefore, it seems likely that this peak is originated from the scattering hole in both the Al and the Ag sample. At $\lambda = 630$ nm similar lateral periodicity is observed in the metal and the a-Si:H layer. On one hand, this denotes surface plasmons, in reference to literature [12, 25, 37]. On the other hand, since the absorption patterns of the Au and the Ag sample strongly agree, it seems likely that the interference pattern is caused by the scattering hole independent of the metal properties. Therefore, the origin of this peak cannot be concluded in this thesis. At $\lambda = 695$ nm a complex absorption cross section is obtained. Relatively strong absorption in the metal layer is observed with an absorption pattern similar to the absorption pattern of surface plasmons [12, 25, 37]. The absorption patterns in the a-Si:H i-layer are very complex. Due to the absorption from the corners of the nanohole in the a-Si:H i-layer, it seems likely that this is caused by surface plasmons localized at the corners of the Ag nanohole. The lateral periodicity in the a-Si:H i-layer is similar to the lateral periodicity in the metal layer. However, the absorption of this lateral periodicity is significantly lower in the a-Si:H i-layer. This could possibly be caused by weak coupling of surface plasmons to a-Si:H i-layer.

5.7 Conclusion

The absorption of the photons which can be described by the Lambert-Beer Law, is not significantly influenced by the nanohole at the metal back contact. In the three samples with a 100 nm, 300 nm and 400 nm nanohole plasmon resonances are probably observed within the nanoholes at $\lambda = 526$ nm. At longer wavelength absorption peaks appear in the absorption curves of the nanoholes which can possibly be assigned to a plasmonic effect and scattering of the nanohole, suported by literature. For confirmation, a more detailed interference analysis will have to be performed. In addition, these simulations are done in 2D. Therefore, 3D simulations are needed to be sure that this plasmonic effect also takes place in the real system. Then the plasmonic nanostructures can couple to each other in two directions, which can enhance the plasmonic absorption peaks.

An other difference that should be studied is the difference between periodic and random grating. The nanoholes are ordered periodically in these simulations. At a certain distance between the particles, the plasmonic modes can couple to each other. The absorption in the a-Si:H layer can be effected by those coupling modes. Vynck et al. (2012) studied the absorption of random distributed nanoholes. Due to the different distances between the holes, coupling to different modes is enabled. Consequently, more peaks at different wavelengths appear in the absorption curves [69]. Therefore, when the nanoholes are placed periodically as in the simulations, the plasmonic peaks can differ from the actual solar cell with randomly distributed nanoholes.

In order to produce a solar cell with a high efficiency, it is important that strong coupling between the plasmon modes and the a-Si:H layer takes place. In addition, the absorption in the metal should not be too high. Concluding from the performances of all solar cells, the 50 nm nanohole Ag sample has the highest efficiency. On the other hand, it is important to restrain the production costs. Since the material costs contribute significantly to the production costs, it is required to use low cost materials. Therefore, it could be interesting to continue research on the 400 nm nanohole Al solar cell. The efficiency of this solar is relatively high, thereby aluminum is a low cost metal.

6 Summary

Solar energy is one of the main renewable energies that generated from the sun and can be converted to electricity by using solar cells. In the absorber layer photons with certain energy can be absorbed to excite an electron-hole pair. The electron-hole pair can be extracted by internal electric field and collected by electrodes thus electricity is generated. The solar cell still suffers from some severe energy losses, i.e.: recombination, thermal and spectral losses. This thesis has introduced two different structures which can contribute to a low cost solar cell with a potentially high efficiency. Both are based on thin film solar cells in which light is trapped due to (plasmonic) nanostructures at the back contact to increase the photon absorption.

The first solar cell has nanorod arrays at the back contact. These rods are synthesized by using a low-cost method. ZnO nanorods are grown by using a wet chemical method, which are covered by a silver coating. This nanostructured back reflector can increase the photon absorption in several ways. First of all, it provides an anti-reflection due to the roughened surface. Secondly, the nanorods at the back contacts increase diffuse reflection at rear side, reflecting unabsorbed photons back into the solar cell. Thirdly, the nanorods orthogonalize the electron path and optical path, hence the optical path is in the axial direction while the carrier transport path is in the radial direction. This solar cell structure was studied in two ways. Firstly, the low cost synthesis of the nanorods is studied. The effects of growth parameters including precursor concentration, growth time, and seed layer thickness on the morphology of nanorods were investigated. The length of the nanorods is dependent on growth time. The site density of the nanorods can be determined by the thickness of seed layer and the concentration. The alignment can be controlled by varying the concentration of the reactants in combination with different thicknesses of the seed layer. By using a Perkin Elmer UV/VIS spectrometer the total and diffuse reflection of the back contact were measured. It can be concluded that the sample fabricated using a precursor concentration of 0.0005 M (mid-range concentration), growth time of 1 hour (short reaction time), and a 1000 nm thick seed layer (thickest seed layer) of ZnO:0.5wt%Al has the optimal combination of total and diffuse reflection. However, when also taking the production costs into account, the sample of 0.0005 M, grown for 1 hour on a 500 nm thick seed layer of ZnO:1wt%Al is the most interesting.

Afterwards, the FDTD simulations on the nanorod based solar cell is performed to study the absorption in the a-Si:H i-layer and optimize the structure of the solar cell. The absorption at low wavelength is increasing towards the optimum at $\lambda = 520$ nm, where optimal constructive interference is obtained. This is caused by the decreasing absorption of light in the ITO layer. The extra absorption in high wavelength regime can be explained by the texture of the ZnO and the Ag metal back contact. The simulated nanorod solar cell with the highest obtained absorption contains nanorods with a length of 300 nm, 600 mn distance between the rods covered by a 300 nm thick a-Si:H i-layer. In this case the anti-reflective character of the top layer, the internal reflection in the absorber layer and the conformal coating of the a-Si:H i-layer are optimized. However, when looking at the realistic case, a 200 nm thick a-Si:H i-layer is probably better, due to the reduced bulk recombination of the charge carriers.

The second structure has nanoholes at the back contact of the solar cell. This nanostructure is studied, because nanoholes can induce both surface plasmons and scattering resonance plasmons. Therefore, this nanostructure can possible increase the absorption of photons with long wavelength. Thereby, the diameter of the nanoholes is varied to find the solar cell with the highest absorption. From the simulations it can be concluded that the nanoholes indeed induce both surface plasmons and scattering resonance plasmons. An increased current density was demonstrated with respect to a flat reference cell due to these absorption peaks originated from the plasmonic effects. The highest efficiency was obtained by a 50 nm nanohole solar cell. On the other hand, when comparing these results to samples in which the Ag back reflector was replaced by Al, it turns out that the efficiency is only slightly lower. Since Al is a low cost material compared to Ag, it is interesting to investigate the 400 nm nanohole cell with Al as back contact.

7 Recommendations

Looking back at the results of this thesis, a few recommendations can be made. Overall, it can be concluded that the absorption enhancement arising from a textured surface is significantly stronger than that originated from the plasmonic effect. This would mean a preference towards further developing a nanorod solar cell. When looking at the simulated results of the nanorod solar cell, it turns out that the absorption would be optimal when using a flat back reflector covered by ZnO nanorods. In this case, the parasitic absorption is minimized while the reflection is maximized. Moreover, the roughened surface provides an anti-reflection effect and due to the presence of ZnO nanorods the photon path and carrier extraction path are orthogonalized. As a cost reduction method, not at expense of significant efficiency reduction, it might be interesting to explore the possibilities to replace the Ag back reflector by Al. Additionally, a smaller radius of the rod might lead to an improved red response [8, 12].

Using the simulated results as a guideline, the preparation of a nanorod solar cell with a flat back reflector from Al could prove to be very interesting as a route towards low cost thin film solar cells.

At all times, it is important to find an optimum between a high efficient solar cell and a low cost solar cell. To reach this optimum a cooperation of both synthetic work and simulations is beneficial. Simulations can provide a guideline as which structures might lead to enhanced properties of thin film solar cells. After that synthetic work can be used to find ways to prepare these structures.

8 Acknoweledgements

I would like to thank the following persons for their contributions of this master thesis. Ruud Schropp, who introduced me to the Nanophotonics group and Yinghuan Kuang for my first steps in solar cell synthesis. Then, I would like to thank Marcel Di Vece and Lourens van Dijk for giving me the opportunity to continue my thesis under their supervision and introducing me into the world of plasmonics. All their advice helped me to create a better understanding about the fundamentals of the photon absorption in solar cells and the use of plasmonics. They also gave me the chance to learn about FDTD simulations and introduced me in a physics subject, despite my background as a chemist.

Furthermore, I would like to thank the complete Nanophotonics group for their help and coffee breaks, and my new colleagues at my new office. I also would like to thank Rutger van Oel for all his beloved support and advice, during the time of this research. Especially, when writing the report.

References

[1] G. Amin, M. H. Asif, A. Zainelabdin, S. Zaman, O. Nur, and M. Willander. Influence of pH, Precursor Goncentration, Growth Time, and Temperature on the Morphology of ZnO Nanostructures grown by the Hydrothermal Method. *J. Nanomaterials*, 2011:5:5–5:5, January 2011.

[2] W. L. Barnes, A. Dereux, and T. Ebbessen. Surface Plasmon Subwavelength Optics. *Nature*, 424:824–830, 2003.

[3] R. Biswas and D. Zhou. Simulation and Modelling of Photonic and Plasmonic Crystal Back Reflectors for Efficient Light Trapping. *physica status solidi (a)*, 207(3):667–670, 2010.

[4] R. M. Cole, J. J. Baumberg, F. J. Garcia de Abajo, S. Mahajan, M. Abdelsalam, and P. N. Bartlett. Understanding Plasmons in Nanoscale Voids. *Nano Letters*, 7(7):2094–2100, 2007.

[5] F. J. Garcia de Abajo. *Colloquium* : Light Scattering by Particle and Hole Arrays. *Reviews of Modern Physics*, 79(4):1267–1290, October 2007.

[6] C. del Canizo, G. del Coso, and W.C. Sinke. Crystalline Silicon Solar Module Technology: Towards the 1 Euro per Watt-Peak Goal. *Progress in Photovoltaics: Research and Applications*, 17(3):199–209, 2009.

[7] R. Dewan and D. Knipp. Light Trapping in Thin-Film Silicon Solar Cells with Integrated Diffraction Grating. *Journal of Applied Physics*, 106(7):074901, 2009.

[8] R. Dewan, I. Vasilev, V. Jovanov, and D. Knipp. Optical Enhancement and Losses of Pyramid Textured Thin-Film Silicon Solar Cells. *Journal of Applied Physics*, 110(1):013101, 2011.

[9] Nederlands Onderzoeksplatform Duurzame Energievoorziening. Thin Layer Solar Cells, jan 2013.

[10] Z. Fan and J.G. Lu. Zinc Oxide Nanostructures: Synthesis and Properties. *Journal of Nanoscience and Nanotechnology*, 5(10):1561–1573, October 2005.

[11] Su feng WEI, Qing JIANG, and Jian she LIAN. Synthesis and Characteristics of Large-Scale ZnO Rods by Wet Chemical Method. *Transactions of Nonferrous Metals Society of China*, 18(5):1089 – 1093, 2008.

[12] V.E. Ferry. *Light Trapping in Plasmonic Solar Cells.* PhD thesis, California Institute of Technology Pasadena, mai 2011.

[13] V.E. Ferry, M.A. Verschuuren, H.B.T. Li, R.E.I. Schropp, H.A. Atwater, and A. Polman. Improved Red-Response in Thin Film a-Si:H Solar Cells with Soft-Imprinted Plasmonic Back Reflectors. *Applied Physics Letters*, 95(18):183503, 2009.

[14] S.J. Fonash. *Solar Cell Device Physics.* Elsevier Inc, 2rd edition edition, 2012.

[15] M.A. Green. Crystalline and Thin-Film Silicon Solar Cells: State of the Art and Future Potential. *Solar Energy*, 74(3):181–192, 2003.

[16] R. Gross, M. Leach, and A. Bauen. Progress in Renewable Energy. *Environment International*, 29(1):105–122, 2003.

[17] S.Y. Han, B.K. Paul, and C. Chang. Nanostructured ZnO as Biomimetic Anti-Reflective Coatings on Textured Silicon Using a Continuous Solution Process. *J. Mater. Chem.*, 22:22906–22912, 2012.

[18] IEA. International Energy Agency, jan 2013.

[19] M.Z. Jacobson and M.A. Delucchi. A path to Sustainable Energy by 2030. *Scientific American*, 301(5):58–65, November 2009.

[20] M. Jefferson. Sustainable Energy Development: Performance and Prospects. *Renewable Energy*, 31(5):571–582, 2006.

[21] H.B. Jo, K.J. Byeon, H. Lee, M.H. Kwon, and K.W. Choi. Fabrication of ZnO Nano-Structures using UV Nanoimprint Lithography of a ZnO Nano-Particle Dispersion Resin. *J. Mater. Chem.*, 22:20742–20746, 2012.

[22] J.Y. Jung, Z. Guo, S.W. Jee, H.D. Um, K.T. Park, and J.H. Lee. A Strong Antireflective Solar Cell prepared by Tapering Silicon Nanowires. *Opt. Express*, 18(S3):A286–A292, Sep 2010.

[23] B.M. Kayes, H.A. Atwater, and N.S. Lewis. Comparison of the Device Physics Principles of Planar and Radial p-n Junction Nanorod Solar Cells. *Journal of Applied Physics*, 97(11):114302, 2005.

[24] T. A. Kelf, Y. Sugawara, R. M. Cole, J. J. Baumberg, M. E. Abdelsalam, S. Cintra, S. Mahajan, A. E. Russell, and P. N. Bartlett. Localized and Delocalized Plasmons in Metallic Nanovoids. *Physical Review B*, 74(24):245415+, December 2006.

[25] U. Kreibig and M. Vollmer. *Optical Properties of Metal Clusters*, volume 118. Springer, 1995.

[26] Y. Kuang, K.H.M. Van der Werf, Z. Silvester Houweling, M. Di Vece, and R.E.I. Schropp. Fabrication and Characterization of Nanorod Solar Cells with an Ultrathin a-Si:H Absorber Layer. *Journal of Non-Crystalline Solids*, 358(17):2209 – 2213, 2012.

[27] Y. Kuang, K.H.M. Van der Werf, Z. Silvester Houweling, and R.E.I. Schropp. Nanorod Solar Cell with an Ultrathin a-Si:H Absorber Layer. *Applied Physics Letters*, 98(11):113111, 2011.

[28] N. N. Lal, B. F. Soares, J. K. Sinha, F. Huang, S. Mahajan, P.N. Bartlett, N.C. Greenham, and J.J. Baumberg. Enhancing Solar Cells with Localized Plasmons in Nanovoids. *Opt. Express*, 19(12):11256–11263, Jun 2011.

[29] N.N. Lal, H. Zhou, M. Hawkeye, J.K. Sinha, P.N. Bartlett, G.A. J. Amaratunga, and J.J. Baumberg. Using Spacer Layers to Control Metal and Semiconductor Absorption in Ultrathin Solar Cells with Plasmonic Substrates. *Phys. Rev. B*, 85:245318, Jun 2012.

[30] Q. Li, V. Kumar, Y. Li, H. Zhang, T.J. Marks, and R.P.H. Chang. Fabrication of ZnO Nanorods and Nanotubes in Aqueous Solutions. *Chemistry of Materials*, 17(5):1001–1006, 2005.

[31] J. Liu, J. She, S. Deng, Jun Chen, and Ningsheng Xu. Ultrathin Seed-Layer for Tuning Density of ZnO Nanowire Arrays and Their Field Emission Characteristics. *The Journal of Physical Chemistry C*, 112(31):11685–11690, 2008.

[32] A.L. Love, J.B. Marquis, and C.L. Haynes. Recent Advances in Nanomaterial Plasmonics: Fundamental Studies and Applications. *Appl. Spectrosc.*, 62(12):346A–362A, Dec 2008.

[33] Lumerical. Finite-Difference Time Domain, jan 2013.

[34] H. Lund. Renewable Energy Strategies for Sustainable Development. *Energy*, 32(6):912–919, 2007.

[35] S. Mahajan, R.M. Cole, B.F. Soares, S.H. Pelfrey, A.E. Russell, J.J. Baumberg, and P.N. Bartlett. Relating SERS Intensity to Specific Plasmon Modes on Sphere Segment Void Surfaces. *The Journal of Physical Chemistry C*, 113(21):9284–9289, 2009.

[36] K. Mahmood and S. Bin. Growth and Conductivity Enhancement of N-doped ZnO Nanorod Arrays. *Journal of Crustal Growth*, (347):104–112, 2012.

[37] A.S. Maier. Plasmonics: Fundamentals and Applications. page 223, 2007.

[38] S.A. Maier. Effective Mode Volume of Nanoscale Plasmon Cavities. *Optical and Quantum Electronics*, 38(1-3):257–267, January 2006.

[39] J. Muller, B. Rech, J. Springer, and M. Vanecek. TCO and Light Trapping in Silicon Thin Film Solar Cells. *Solar Energy*, 77(6):917 – 930, 2004. <ce:title>Thin Film PV</ce:title>.

[40] R.S. Muller and T.I. Kamins. *Device Electronics for Integrated Circuits.* John Wiley & Sons, 3rd edition edition, January 2003.

[41] W. A. Murray and W. L. Barnes. Plasmonic Materials. *Advanced Materials*, 19(22):3771–3782, nov 2007.

[42] M. J. Naughton, K. Kempa, Z. F. Ren, Y. Gao, J. Rybczynski, N. Argenti, W. Gao, Y. Wang, Y. Peng, J. R. Naughton, G. McMahon, T. Paudel, Y. C. Lan, M. J. Burns, A. Shepard, M. Clary, C. Ballif, F. J. Haug, T. Soderstrom, O. Cubero, and C. Eminian. Efficient Nanocoax-based Solar Cells. *physica status solidi (RRL)*, 4(7):181–183, 2010.

[43] L. Novotny and B. Hecht. Principles of Nano-Optics, 2006.

[44] NREL. National Renewable Energy Laboratory, jan 2013.

[45] J.W. Park, J.K. Kim, and K.Y. Suh. Fabrication of Zinc Oxide Nanostructures using Solvent-Assisted Capillary Lithography. *Nanotechnology*, 17(10):2631, 2006.

[46] T.H. Park, N. Mirin, J.B. Lassiter, C.L. Nehl, N.J. Halas, and P. Nordlander. Optical Properties of a Nanosized Hole in a Thin Metallic Film. *ACS Nano*, 2(1):25–32, 2008.

[47] S. Pillai and M.A. Green. Plasmonics for Photovoltaic Applications. *Solar Energy Materials and Solar Cells*, 94(9):1481 – 1486, 2010. <ce:title>PVSEC 18</ce:title>.

[48] J. Podzemsky and W. Schade. Vapor-Liquid-Solid Growth of ZnO Nanostructure. In *Electronics Technology, 2009. ISSE 2009. 32nd International Spring Seminar on*, pages 1 –4, may 2009.

[49] PVCDROM. PVeducation, jan 2013.

[50] E. Rayon and C. Ferrer. Electrochemical Deposition of ZnO Nanostructures. Mechanism of Growth. *Journal of Nanoscience and Nanotechnology*, 10(2), 2010.

[51] T.M. Razykov, C.S. Ferekides, D. Morel, E. Stefanakos, H.S. Ullal, and H.M. Upadhyaya. Solar Photovoltaic Electricity: Current Status and Future Prospects. *Solar Energy*, 85(8):1580–1608, 2011.

[52] J.J. Richardson, D. Estrada, S.P. DenBaars, C.J. Hawker, and L.M. Campos. A facile Route to Patterned Epitaxial ZnO Nanostructures by Soft Lithography. *J. Mater. Chem.*, 21:14417–14419, 2011.

[53] R.E.I. Schropp. Large-Area Thin-Film Silicon: Synergy between Displays and Solar Cells. *Japanese Journal of Applied Physics*, 51:03CA07, 2012.

[54] W.E.I. Sha, W.C.H. Choy, and W.C. Chew. A Comprehensive Study for the Plasmonic Thin-Film Solar Cell with Periodic Structure. *Opt. Express*, 18(6):5993–6007, Mar 2010.

[55] A. Shah, P. Torres, R. Tscharner, N. Wyrsch, and H. Keppner. Photovoltaic Technology: The Case for Thin-Film Solar Cells. *Science*, 285(5428):692–698, 1999.

[56] A. V. Shah, H. Schade, M. Vanecek, J. Meier, E. Vallat-Sauvain, N. Wyrsch, U. Kroll, C. Droz, and J. Bailat. Thin-Film Silicon Solar Cell Technology. *Progress in Photovoltaics: Research and Applications*, 12(2-3):113–142, 2004.

[57] X. Sheng and W. Zhong Lin. One-Dimensional ZnO Nanostructures: Solution Growth and Functional Properties. *Nano Research*, 4(11):1013–1098, 2011.

[58] W. Shockley and H.J. Queisser. Detailed Balance Limit of Efficiency of p-n Junction Solar Cells. *Journal of Applied Physics*, 32(3):510–519, 1961.

[59] K. Soderstrom, F.J. Haug, J. Escarre, O. Cubero, and C. Ballif. Photocurrent Increase in n-i-p Thin Film Silicon Solar Cells by Guided Mode Excitation via Grating Coupler. *Applied Physics Letters*, 96(21):213508, 2010.

[60] A.K. Sood, Y.R. Puri, W. Mai, P. Gao, C. Lao, Z.L. Wang, D.L. Polla, and M.B. Soprano. ZnO Nanostructures for Optoelectronic Applications. *Proc. of SPIE*, 6959:69591A–69591A–8, 2008.

[61] P. Spinelli, V.E. Ferry, J. Van de Groep, M. Van Lare, M. A. Verschuuren, R.E.I. Schropp, H.A. Atwater, and A. Polman. Plasmonic Light Trapping in Thin-Film Si Solar Cells, year = 2012, journal = Journal of Optics, pages = 024002, volume = 14, number = 2,.

[62] B.A. Taleatu, A.Y. Fasasi, G. Di Santo, S. Bernstorff, A. Goldoni, M. Fanetti, L. Floreano, P. Borghetti, L. Casalis, B. Sanavio, and C. Castellarin-Cudia. Electro-Chemical Deposition of Zinc Oxide Nanostructures by using Two Electrodes. *AIP Advances*, 1(3):032147, 2011.

[63] M. Tsoskounoglou, G. Ayerides, and E. Tritopoulou. The End of Cheap Oil: Current Status and Prospects. *Energy Policy*, 36(10):3797 – 3806, 2008.

[64] A. Umar, Y.H. Im, and Y.B. Hahn. Evolution of ZnO Nanostructures on Silicon Substrate by Vapor-Solid Mechanism: Structural and Optical Properties. *Journal of Electronic Materials*, 35:758–765, 2006.

[65] A. Umar, S.H. Kim, Y.S. Lee, K.S. Nahm, and Y.B. Hahn. Catalyst-Free Large-Quantity Synthesis of ZnO Nanorods by a Vapor-Solid Growth Mechanism: Structural and Optical Properties. *Journal of Crystal Growth*, 282(1):131 – 136, 2005.

[66] D. Van Dam. Plasmonic Light Trapping in Thin Film Amorphous Silicon Solar Cells using Nanoholes and Nanoclusters, August.

[67] L. Vayssieres. Growth of Arrayed Nanorods and Nanowires of ZnO from Aqueous Solutions. *Advanced Materials*, 15(5):464–466, 2003.

[68] E. Verhagen. *Subwavelength Light Confinement with Surface Plasmon Polaritons*. PhD thesis, University Utrecht, dec 2009.

[69] K. Vynck, M. Burresi, F. Riboli, and D.S. Wiersma. Photon Management in Two-Dimensional Disordered Media. *Nature Materials*, 11(12):1017–1022, 2012.

[70] Z.L. Wang. Zinc Oxide Nanostructures: Growth, Properties and Applications. *Journal of Physics: Condensed Matter*, 16(25):R829, 2004.

[71] Wikipedia. Anti-Reflective Coating, jan 2013.

[72] Wikipedia. Diffuse Reflection, jan 2013.

[73] Wikipedia. Kyoto Protocol, jan 2013.

[74] R. Williams. Becquerel Photovoltaic Effect in Binary Compounds. *The Journal of Chemical Physics*, 32(5):1505–1514, 1960.

[75] Z. Yang, Q.H. Li, F.X. Ruan, Z.P. Li, B. Ren, H.X. Xu, and Z.Q. Tian. FDTD for Plasmonics: Applications in Enhanced Raman Spectroscopy. *Chinese Science Bulletin*, 55:2635–2642, 2010. 10.1007/s11434-010-4044-0.

[76] H. Zhang, J. Feng, J. Wang, and M. Zhang. Preparation of ZnO Nanorods through Wet Chemical Method. *Materials Letters*, 61(30):5202 – 5205, 2007.

[77] Q.X. Zhao, P. Klason, and M. Willander. Growth of ZnO Nanostructures by Vapor-Liquid-Solid Method. *Applied Physics A*, 88:27–30, 2007.

[78] D. Zhou and R. Biswas. Photonic Crystal Enhanced Light-Trapping in Thin Film Solar Cells. *Journal of Applied Physics*, 103(9):093102, 2008.

[79] J. Zhu, C.M. Hsu, Z. Yu, S. Fan, and Y. Cui. Nanodome Solar Cells with Efficient Light Management and Self-Cleaning. *Nano Letters*, 10(6):1979–1984, 2010.